Humberto Paulo Gomes Pereira

Coupled Modelling of the Minho and Lima Estuaries: Hydrological Response to Climate Changes

Modelação Acoplada dos Estuários do Minho e do Lima: Resposta Hidrológica às Alterações Climáticas

Humberto Paulo Gomes Pereira

Coupled Modelling of the Minho and Lima Estuaries: Hydrological Response to Climate Changes

Modelação Acoplada dos Estuários do Minho e do Lima: Resposta Hidrológica às Alterações Climáticas

Dissertação apresentada à Universidade de Aveiro para cumprimento dos requisitos necessários à obtenção do grau de Mestre em Ciências do Mar e Zonas Costeiras, realizada sob a orientação científica do Doutor João Miguel Sequeira Silva Dias, Professor Auxiliar com Agregação do Departamento de Física da Universidade de Aveiro e co-orientação do Doutor Fernando Manuel Raposo Morgado, Professor Associado com Agregação do Departamento de Biologia da Universidade de Aveiro.

o júri

presidente	**Doutora Filomena Maria Cardoso Pedrosa Ferreira Martins** Professora Associada do Departamento de Ambiente e Ordenamento da Universidade de Aveiro
arguente	**Doutora Magda Catarina Ferreira de Sousa** Estagiária de Pós-Douturamento do CESAM da Universidade de Aveiro
orientador	**Doutor João Miguel Sequeira Silva Dias** Professor Auxiliar com Agregação do Departamento de Física da Universidade de Aveiro

acknowledgements

I would like to thank to all the people that helped me in my MSc thesis.

To Professor João Miguel Dias for all the support since day one in this university. For all the comments, suggestions and friendship that he gave me, a big thank you.

To Professor Fernando Morgado for all the help and suggestions during this process.

To Magda Sousa, the person that guide me since the beginning and support me in all my work.

To NMEC (Estuarine and Coastal Modelling Division) for giving me the best conditions to do my thesis and a special appreciation to Américo Ribeiro, the person that helped me no matter what.

And the last but not the least, to my parents, girlfriend and friends. They were always there for me in everything and I can't thank them enough.

To all of them I dedicate this thesis.

palavras-chave

Estuário do Minho; Estuário do Lima; Delft3D; Padrões Hidrológicos; Alterações Climáticas; Pluma Estuarina; Intrusão Salina.

resumo

Em Portugal, o rio Minho e o rio Lima originam os estuários situados mais a Norte próximos de Espanha, e estando estes separados por aproximadamente 20 km, surge a necessidade de investigar se interagem entre si e de efetuar a sua caracterização hidrológica simultaneamente. Atualmente a modelação numérica é a ferramenta mais utilizada em estudos sobre a hidrodinâmica estuarina, permitindo aumentar o conhecimento das propriedades e padrões físicos nestes sistemas. Neste trabalho foi implementado o modelo numérico tridimensional Delft3D-Flow, para estudar quais as variações físicas e dinâmicas dos estuários e qual a resposta hidrológica destes sistemas sob a influência das alterações climáticas. Este modelo foi calibrado e validado com a altura de maré, salinidade e temperatura da água, sendo depois aplicado em dois cenários de alterações climáticas (RCP 4.5 e RCP 8.5) onde se variaram parâmetros como o nível do mar e descargas fluviais. As simulações foram realizadas para os meses de verão e inverno do ano 2100/2101. As previsões numéricas revelaram padrões hidrológicos tipicamente estuarinos e que, no verão, o estuário do Minho é mais quente mas o estuário do Lima é mais salino. No inverno, o Lima é o estuário mais quente e salino. Da análise de resultados verificou-se que a zona interior dos estuários será a mais afetada com as alterações climáticas. A intrusão salina no rio Minho atinge os 13 km no Presente e no cenário RCP 4.5, e no cenário 8.5 atinge os 14 km. No rio Lima a intrusão é maior, chegando aos 15 km no Presente e no cenário RCP 4.5, e atinge o máximo de 17.5 km no cenário RCP 8.5. Por fim, foi ainda realizado o estudo das plumas estuarinas onde se observou que estas são maiores e mais largas durante o inverno nos cenários RCP 4.5 e 8.5. Concisamente, a modelação desenvolvida neste estudo contribuiu para um aumento do conhecimento dos padrões físicos destes dois estuários bem como da interação destes na região costeira adjacente. Para trabalhos futuros, este modelo poderá constituir a base para a aplicação de um modelo biogeoquímico, o que permitirá aumentar o conhecimento sobre estes processos nestes estuários.

keywords

Minho Estuary; Lima Estuary; Delft3D; Hydrological Patterns; Climate Change; Estuarine Plume; Salt Intrusion.

abstract

In Portugal, the Minho river and the Lima river originate the northern estuaries near Spain, and being these separated by approximately 20 km, there is a need to investigate if they interact with each other and to carry out its hydrological characterization simultaneously. Numerical modelling is the most used tool in studies about estuarine hydrodynamics, allowing to increase the knowledge of physical properties and patterns in these systems. In this work, the three-dimensional numerical model Delft3D-Flow was implemented to investigate the physical and dynamic variations of these two systems and their hydrological response under the influence of climate change. The model was calibrated and validated with tidal height, salinity and water temperature, and then applied to two scenarios of climate change (RCP 4.5 e RCP 8.5) where variables such sea level and river discharge were varied. The simulations were realized for the summer and winter months of the year 2100/2101. The numerical predictions revealed hydrological patterns typically estuarine and that, in summer, the Minho estuary is warmer but the Lima estuary is more saline. In winter, Lima is the hottest and saline estuary. Of the results analysis it was verified that the interior zone of the estuaries will be most affected by climate change. The saline intrusion in Minho river reaches 13 km in Present and in RCP 4.5 scenario, and in RCP 8.5 it reaches 14 km. In the Lima river the intrusion is higher, reaching 15 km in Present and in RCP 4.5 scenario, and reaches the maximum of 17.5 km in RCP 8.5. Finally, a study of the estuarine plumes was carried out, where it was observed that these are larger and wider during winter in the scenario RCP 4.5 and 8.5. Concisely, the modelling developed in this study contributed to an increased knowledge of the physical patterns in these two estuaries as well as their interaction in the adjacent coastal region. For future work, this model may be the basis for the application of a biogeochemical model, which will increase the knowledge about these processes in these estuaries.

Contents

List of Figures

List of Tables

Chapter 1

Introduction

1.1 Motivation

Climate change is a modification in the distribution of climate patterns when that change lasts for a long period of time (from decades to million years). Human activities has been identified as significant causes of recent global warming. The factors causing climate change are natural, external and anthropogenic, and the impacts are felted in land, water and atmosphere.

Coastal zones are important for humans because they have special characteristics like warm weather, productive soils and more job opportunities that provide a better life quality. Here we can see transition zones from land to sea as lagoons, estuaries and fjords. From the physics point of view, the most used definition of an estuary was given by Pritchard (1967) defining it as a *"semi-enclosed coastal body of water, which has a free connection with the open sea, and within which sea water is measurably diluted with fresh water derived from land drainage"*.

According to Arndt et al. (2011) estuaries are complex systems, where there are several processes forced by waves, tides, freshwater inflow, wind stress and exchanges with the atmosphere. All these mechanisms influence and affect the hydrodynamics of the estuary. Each estuary has unique characteristics which makes it crucial to the ecosystem where it is inserted, making them the most productive and valuable aquatic systems on earth (Costanza et al., 1997). These areas are related with high primary production, fish's shelters and nurseries, and with human constructions. These features leads to a development of human populations near estuarine borders that can increase the anthropogenic stress, turning these regions into vulnerable systems requiring frequent surveillance (Rodrigues, 2015).

The study of the characteristics of coastal zones and its dependence on physical, chemical and biological factors is becoming very important. The demand for this kind of information arises from a range of fields and applications, such as scientific research on marine ecosystems, monitoring of seawater quality and decision-making support for marine and coastal management (Picado, 2016). The request for numerical models able to reproduce physical and biogeochemical interactions in estuarine systems arise to overcome the lack of continuous and long term observations and to provide forecasts of estuarine evolution (Marta-Almeida et al., 2012).

Dias (2001) said that an accurate and reliable numerical model must be able to reproduce transport and mixing processes as response of different forcing conditions in boundaries as well as of anthropogenic interventions.

The results produced by numerical models are very useful but their reliability depends on the adequacy of the model to reproduce the domains characteristics as well as to solve both space and time scales, correctly parameterized (Ribeiro, 2015). Thus, a good knowledge of the estuarine physical processes is essential to use correctly the numerical models.

Neves (2007) stated that numerical modelling results can give a valuable support to major decisions, like the design of ports, sewage systems and ecological reserves but to be classified as a Decision Support Tool, the model must have a good performance in producing results that describe a reference situation and hypothetical scenarios.

Since the estuaries of Minho and Lima are separated by only 20 km, it is likely that there may be a connection between the water masses coming from the two estuaries. Thus, as currently there are no studies about coupled modelling of Minho and Lima estuaries, this work tries to fulfil this gap. This thesis attempts to implement a numerical model of circulation and transport in order to investigate the variation of water temperature and salinity inside the estuaries and near the coastal zone.

1.2 Aims

The Minho and Lima estuaries have different characteristics and dynamics, for instance the size, shape and volume of freshwater input. There are some studies about this two estuaries, but none of them discusses their dynamics in three dimensions, the distribution of salinity and water temperature within the estuary and in the water column as well as their possible interaction, and the climatic change impact on their dynamics.

Therefore, the main goal of this dissertation is to implement a three-dimensional baroclinic model (Delft3D) in order to study the dynamics, the distribution of salinity and water temperature and the modification induced by climate change in both estuaries, considering in a unique modelling application. To achieve this purpose, some particular objectives are settled down:

- Characterize the estuaries of Minho and Lima;
- Develop a numerical model application to reproduce and represent the hydrodynamics of both estuaries and adjacent coastal area;
- Calibrate the model application;
- Study the vertical and longitudinal distributions of water temperature and salinity;
- Analyse the hydrological response to climate changes.

1.3 Literature Review

1.3.1 Minho Estuary

The Minho river it is located in the north of Portugal bordering with Spain, originating the Minho estuary, that has been the subject of some scientific studies.

Santos et al. (2006) investigated the hydrography and dynamics dependence on tidal variability during low run-off, concluding that the estuary revealed a vertical homogeneity during spring and a highly stratified structure during neap tide. Zacarias (2007) analysed the effect of bathymetry and river flow in tidal propagation verifying that the existence of bathymetric constraints influences the tidal wave progression inside the estuary and that the river flow do not.

Delgado et al. (2011) made a simulation of the estuary's hydrodynamic and morphodynamic concluding that the numerical simulation, when associated with proper characterization of the water lines, bottom material and solid cargo transported by drag and in suspension allows to observe that the deposition of sediments is high and currents velocities are low, creating sand banks and islands.

The Minho plume and his interaction with Rias Baixas and with Douro plume was studied by Sousa et al. (2014a), Sousa et al. (2014b,c) and Mendes et al. (2016). These authors made a complete characterization of the hydrodynamics in the region supplementing it with a description of estuarine plumes and their interactions along the Northwest coast of the Iberian Peninsula concluding that the Minho and Douro plumes can interact with Rias Baixas through the Western Iberian Buoyant Plume under certain conditions.

The textural composition of sediments and its relation with hydrodynamics was analysed by Balsinha et al. (2009), which concluded that it is only possible to divide the estuary in lower and upper parts with no detectable middle one, due to sediment homogeneity (sandy river, with predominance of medium to very fine sands) and Mil-Homens et al. (2013) studied the heavy metal and metalloid concentrations in sediments of the estuary concluding that there is a low total concentration of heavy metals and metalloids, with the exception of mercury that presented concentrations slightly higher than the expected natural levels.

Finally, Pinto and Martins (2013) utilized the Portuguese National Strategy for Integrated Coastal Zone Management as a spatial planning instrument to climate change adaptation and Roebeling et al. (2014) examined the gains in the area due to water quality management concluding that national welfare maximization leads to increased rates of water pollution (+5%), while trans-national welfare maximization leads to significant reductions in rates of water pollution (-14%).

1.3.2 Lima Estuary

The Lima river is located south of Minho, originating the Lima estuary. Vieira and Pinho (2010) studied the salt distribution in Lima estuary for different hydrodynamic regimes concluding that for river flow values below 100 $m^3 s^{-1}$ the transition between salt and fresh occurs mainly inside the estuary, and that the estuarine plume moves to north when exists winds from South.

Pinho and Vieira (2005) applied a 2DH hydrodynamic and mass transport model to analyse the salt water intrusion in the estuary concluding that the saline intrusion reaches 12 km upstream the river mouth, for the most unfavourable conditions (spring tide and low river discharge) and for more frequent river flows, the salinity gradients occur mainly downstream (5 km from river mouth).

Vale and Dias (2011) investigated the effect of tidal regime and river flow on the hydrodynamics and salinity structure, concluding that the estuary classification varies between well mixed and slight stratified water column due to river flow and tidal cycle, and the river discharge is highly variable depending mainly on the Touvedo and Alto Lindoso power generating dams. Falcão et al. (2013) saw the influence of elevation modelling on hydrodynamic simulations concluding that the larger differences between using different elevation models occur at low tide during spring tide, slightly influencing the flood modelling.

Rebordão and Trigo-Teixeira (2009) studied the tidal propagation showing that this plays an important role in the circulation and mixing processes in the estuary, Trigo-Teixeira and Rebordão (2009) made an assessment of tidal energy potential for the installations of tidal turbines, and Araújo et al. (2011) and Marujo et al. (2014) studied the ADCIRC model's capacity to model storm-surge events in the region concluding that the meteorology and astronomical effects interact non-linearly, being more pronounced when considering the river flow due to the tidal wave–current interaction.

Lastly, Cardoso et al. (2006, 2008) characterized geochemically the sediments of salt marshes and marginal environments concluding that the highest concentrations of metals tend to occur in the high marshes, playing an important role in heavy metals retention.

1.3.3 Climate Change

Climate change has been the subject of scientific studies all over the world. Snyder et al. (2003) studied the effect of climate change in the upwelling of the California coast concluding that there is an intensification of the upwelling season, with some changes in seasonality, leading to enhanced productivity along the coast of California. Najjar et al. (2010) characterized the potential climate change impacts on the Chesapeake Bay, concluding that these changes will increase the coastal flooding, the salinity variability, the harmful algae and the hypoxia.

Macías et al. (2014) studied the consequences of a future climatic scenario for the anchovy fishery in the Alboran Sea, concluding that there will be a substantial increase in horizontal water velocity and a negligible change in the associated biological production, which likely indicates reductions in anchovy stock, catches and revenues. Lazzari et al. (2014) analysed the impacts of climate change and environmental management policies on the trophic regimes in the Mediterranean Sea, concluding that the increase in temperature fuels will raise the metabolic rates, leading to a gross primary production increment.

Finally, Brown et al. (2016) made a study about the effect of climate change on water temperature in the Yaquina Estuary (USA), concluding that the largest water temperature increases are expected in the upper portion of the estuary, while sea level rise may mitigate some of the warming in the lower part being the smallest changes in water temperature predicted for summer, and maximum for winter and spring.

1.3.4 Delft3D

The numerical model applied in this thesis was Delft3D. This model is a world leading 3D modelling component used to study hydrodynamics, sediment transport and morphology, and water quality for fluvial, estuarine and coastal environments.

The FLOW module is the heart of Delft3D, integrating a 2D or 3D hydrodynamic model which calculates non-steady flow and transport phenomena resulting from tidal and meteorological forcing on a curvilinear, boundary fitted grid or spherical coordinates (Deltares, 2014a). In 3D simulations, the vertical grid is defined following the σ or Z-model approach.

This model is applied in all world and has proven his good capabilities to study different processes in a large number of coastal systems, as for example the hydrodynamic and sediment transport in Yangtze estuary, China (Hu et al., 2009), the coastal processes and alongshore sediment transport in Kundapura coast, India (Shanas and Kumar, 2014), the long-term hydrodynamic in Persian gulf, Arabia (Elhakeem et al., 2015) and in San Quintin Bay, Mexico (Garcia et al., 2015), the influence of tides, winds and waves on the redistribution of nourished sediment in Terschelling, Netherlands (Grunnet et al., 2005), the suspended sediment concentration in Dithmarschen Bight, Germany (Rahbani, 2015) and the coupled modelling of Tagus and Sado estuaries in Portugal (Ribeiro et al., 2016).

With more than 400 scientific articles reporting studies with different purposes in a lot of coastal spaces, the Delft3D model proves to have a good capacity to simulate the hydrodynamic and physical patterns distribution in Minho and Lima estuaries.

1.4 Structure of this Work

This dissertation is divided in six chapters. Chapter 1 presents the motivation, the description of principal aims, the literature review about researches in Minho and Lima estuaries and about studies using Delft3D hydrodynamic model, and the structure of the thesis.

A detailed description of the study area with special attention to Minho and Lima estuaries is presented in Chapter 2, and in Chapter 3 is presented the numerical model equations. The field data, the bathymetry, the boundary conditions, the wind direction and velocity and the river discharge used for the numerical simulations, and the model's establishment and calibration are presented in Chapter 4. In Chapter 5, the climate change scenarios and their features, as well as the model predictions and their discussion are present. Finally, in Chapter 6 is given a global overview of the results, presenting final conclusions and providing some further research suggestions.

Chapter 2

Description of the Study Area and Estuaries Characterization

2.1 Introduction

The study area, comprising the Minho and Lima estuaries, is located in the North Western part of Portugal (Figure 2.1) between 41º 36' and 42º 2' N and between 8º 24' and 8º 54' W.

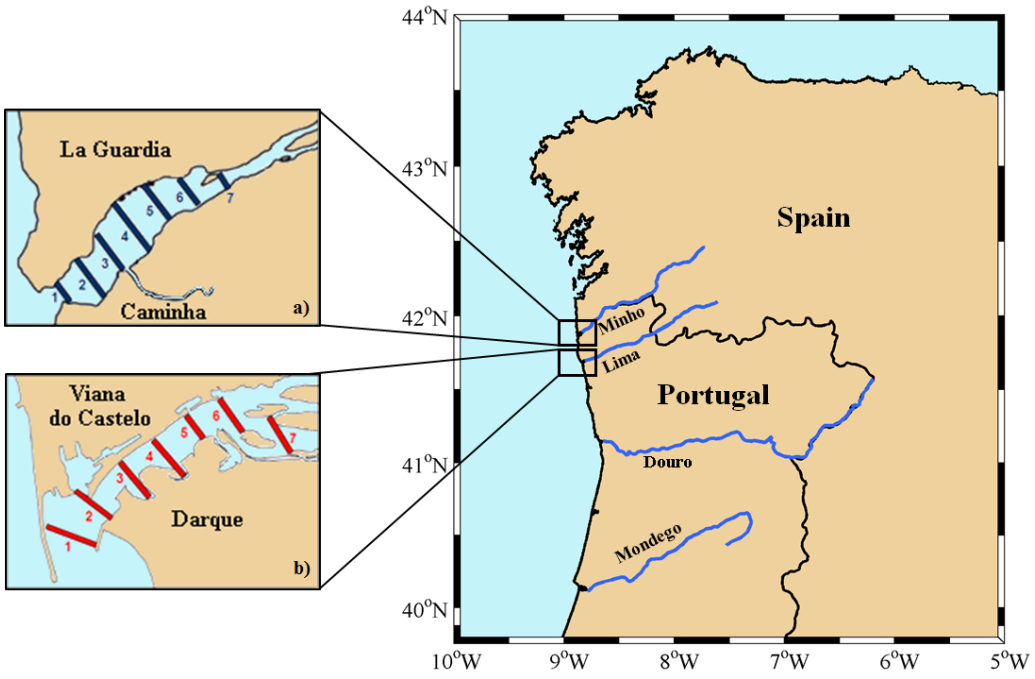

Figure 2.1: Map of North Western part of Iberian Peninsula. a) Minho estuary and b) Lima estuary with sampling transects (T1-T7) in both estuaries.

2.2 Minho Estuary

Minho river is an international river located in the north of Portugal with a special characteristic: it forms a natural border between Portugal and Spain. It rises in Sierra de Meira (Spain) at 750 m altitude and flows in front of Caminha, Portugal and La Guardia, Spain. With a total length of 300 km, the upper part, around 230 km, stays in Spain and the lower part, around 70 km, in Portugal. With a basin area of 17080 km^2, 95% is located in Spain and only 5% in Portugal. The annual average river discharge is about 305 m^3s^{-1}, and the monthly average discharge varies between 121 m^3s^{-1} in the summer and 692 m^3s^{-1} in the winter (Sousa, 2013).

With 35 km long and a total area of 23 km^2, Minho estuary is located at 41º 55.1' N and 8º 26.4' W (Figure 2.2). The estuary has a maximum width of 2 km near the mouth and decrease to 100 m at the head. In the lower part of the estuary, there is a region with sand banks and small islands due to sediment accumulation. The mean depth of the estuary is 2.6 m and the maximum depth is 6 m near the mouth (Freitas et al., 2009). With a semi-diurnal and mesotidal regime, the astronomical tide range varies between 2 m (in neap tides) and 4 m (in spring tides) (Ferreira et al., 2003). Sousa et al. (2005) consider the Minho estuary as a partially mixed system, although during the period of high floods it tends to evolves into a salt wedge estuary.

The climate in this area is the result of the geographic position, the proximity to Atlantic Ocean and the shape and arrangement of the principal mountainous sets in the region (Zacarias, 2007).

Figure 2.2: Satellite image of Minho estuary.

2.3 Lima Estuary

Lima river is located south of the Minho river. It is an international river which rises at 950 m altitude in Sierra S. Mamede located in Orense, Spain, and flows in front of Viana do Castelo, Portugal. This river has a total length of 108 km and a basin area of 2460 km^2. In Spain the river has about 41 km length and in Portugal around 67 km. The annual discharge is very variable, because it depends on two dams (Touvedo and Alto Lindoso) located upstream (Vale and Dias, 2011). The average discharge ranges between 30 m^3s^{-1} in the summer and 130 m^3s^{-1} in the winter (SNIRH, www.snirh.pt).

With 22 km long and a total area of 5.5 km^2, Lima estuary is located at 41º 40.1' N and 8º 35.7' W (Figure 2.3). In Portugal, the estuary has a maximum width of 1 km near the mouth and decrease to 50 m at the head. In the mouth exists a 2 km long jetty directing the river flow to the south. The mean depth of the estuary is 3 m and the maximum depth is 10 m in the center channel due to the constant dredging activity. This estuary has a semi-diurnal and mesotidal regime (the high tidal range is 3.4 m and the low tidal range is 1 m) reaching 1 ms^{-1} of downstream current velocity during ebb tide (Vale, 2008). Lima estuary is considered partially mixed and the salt intrusion extends up to 12 km upstream (Pinho and Vieira, 2005).

Due to the presence of Peneda and Amarela Sierras as well as the proximity to the Atlantic Ocean, the climate in this region is highly wet and mesothermal, being described as maritime (Ramos, 2007). The annual mean rainfall at the Portuguese part of the estuary is 2164 mm. In average, 73% of the precipitation occurs during winter season and 27% during summer season.

Lima river basin has a high ecological importance, with relevant ecosystems and important biodiversity, and it is mostly used for water supply, agricultural irrigation and hydro power generation (Ramos, 2007).

Figure 2.3: Satellite image of Lima estuary.

Chapter 3

Numerical Model DELFT3D

This Chapter presents the model's equations used in the modelling process. It is presented the governing equations, the flow and transport equations for the boundary conditions, and the turbulence and heat flux equations. The informations here presented were taken from Deltares (2014a).

3.1 Principles of the Flow Module

Delft3D is the integrated flow and transport modelling system of Deltares for the aquatic environment and can be applied in shallow seas, coastal areas, estuaries, lagoons, rivers and lakes. Delft3D-FLOW is the flow module of the Delft3D system and it provides the hydrodynamic basis for other modules like water quality, ecology, waves and morphology.

This hydrodynamic module simulates two-dimensional (2DH, depth-averaged) or three-dimensional (3D) unsteady flow and transport phenomena resulting from tidal and meteorological forcing, including the effect of density differences due to a non-uniform water temperature and salinity distribution. In transport issues, where the horizontal flow field shows significant variation in the vertical direction, the three dimensional modelling acquires a special interest. Some examples are the upwelling and downwelling of nutrients, the salt intrusion in estuaries, the fresh water river discharges in the coastal systems and thermal stratification in seas.

Delft3D-FLOW provides two different vertical grid systems: σ coordinate system (σ-model) and the Cartesian Z coordinate system (Z-model). The σ-model has a constant number of layers, usually with non-uniform thickness, over the entire horizontal area independently of the local water depth which allows more resolution in the interest zones. The Z-model has horizontal coordinate lines that are parallel with density interfaces (isopycnics) in region with steep bottom slopes which is important to reduce artificial mixing of scalar properties.

3.2 Governing Equations

The Delft3D-FLOW model solves the shallow water equations in 2D (depth-averaged) or in 3D. The equation's system consists in the horizontal equations of motion, the continuity equation and the transport equations for conservative constituents. The equations are formulated in orthogonal curvilinear or in spherical coordinates. In curvilinear coordinates, the reference of the free surface level and bathymetry are related to a flat horizontal plane, whereas in spherical coordinates the reference plane follows the Earth's curvature.

The depth-average continuity equation is given by:

$$\frac{\partial \zeta}{\partial t}+\frac{1}{\sqrt{G_{\xi\xi}}\sqrt{G_{\eta\eta}}}\frac{\partial[(h+\zeta)U\sqrt{G_{\eta\eta}}]}{\partial \xi}+\frac{1}{\sqrt{G_{\xi\xi}}\sqrt{G_{\eta\eta}}}\frac{\partial[(h+\zeta)V\sqrt{G_{\xi\xi}}]}{\partial \eta}=(h+\zeta)Q \tag{3.1}$$

With h representing the water depth, ζ the free surface elevation, $\sqrt{G_{\xi\xi}}$ and $\sqrt{G_{\eta\eta}}$ the coefficients used to transform curvilinear coordinates into rectangular coordinates, Q the contribution, per unit area, of water discharge, precipitation and evaporation, and U and V the depth average velocities, given by:

$$U=\frac{1}{h+\zeta}\int_h^{\zeta} u\,dz=\int_{-1}^{0} u\,d\sigma \tag{3.2}$$

and

$$V=\frac{1}{h+\zeta}\int_h^{\zeta} v\,dz=\int_{-1}^{0} v\,d\sigma \tag{3.3}$$

The momentum equation in ξ-direction is:

$$\begin{aligned}&\frac{\partial u}{\partial t}+\frac{u}{\sqrt{G_{\xi\xi}}}\frac{\partial u}{\partial \xi}+\frac{v}{\sqrt{G_{\eta\eta}}}\frac{\partial u}{\partial \eta}+\frac{w}{h+\zeta}\frac{\partial u}{\partial \sigma}-\frac{v^2}{\sqrt{G_{\xi\xi}}\sqrt{G_{\eta\eta}}}\frac{\partial \sqrt{G_{\eta\eta}}}{\partial \xi}+\\&+\frac{uv}{\sqrt{G_{\xi\xi}}\sqrt{G_{\eta\eta}}}\frac{\partial \sqrt{G_{\xi\xi}}}{\partial \eta}-fv=-\frac{1}{\rho_0\sqrt{G_{\xi\xi}}}P_\xi+F_\xi+\frac{1}{(h+\zeta)^2}\frac{\partial}{\partial \sigma}\left(\nu_V\frac{\partial u}{\partial \sigma}\right)+M_\xi\end{aligned} \tag{3.4}$$

and in η-direction is:

$$\begin{aligned}&\frac{\partial v}{\partial t}+\frac{u}{\sqrt{G_{\xi\xi}}}\frac{\partial v}{\partial \xi}+\frac{v}{\sqrt{G_{\eta\eta}}}\frac{\partial v}{\partial \eta}+\frac{w}{h+\zeta}\frac{\partial v}{\partial \sigma}-\frac{u^2}{\sqrt{G_{\xi\xi}}\sqrt{G_{\eta\eta}}}\frac{\partial \sqrt{G_{\xi\xi}}}{\partial \eta}+\\&+\frac{uv}{\sqrt{G_{\xi\xi}}\sqrt{G_{\eta\eta}}}\frac{\partial \sqrt{G_{\eta\eta}}}{\partial \xi}+fu=-\frac{1}{\rho_0\sqrt{G_{\eta\eta}}}P_\eta+F_\eta+\frac{1}{(h+\zeta)^2}\frac{\partial}{\partial \sigma}\left(\nu_V\frac{\partial u}{\partial \sigma}\right)+M_\eta\end{aligned} \tag{3.5}$$

Where P_ξ and P_η are the pressure gradients, F_ξ and F_η the forces for the unbalance of horizontal Reynold's stresses, M_ξ and M_η the contributions due to external sources or outcomes of momentum, f the Coriolis parameter ($f = 2\Omega \sin\phi$) and ν is the coefficient for the vertical eddy viscosity.

The vertical velocity, also interpreted as the velocity associated with upwelling or downwelling motions, is obtained from the continuity equation (Equation 3.1) adapted to σ coordinate system, resulting:

$$\begin{aligned} &\frac{\partial \zeta}{\partial t} + \frac{1}{\sqrt{G_{\xi\xi}}\sqrt{G_{\eta\eta}}} \frac{\partial[(h+\zeta)u\sqrt{G_{\eta\eta}}]}{\partial \xi} + \frac{1}{\sqrt{G_{\xi\xi}}\sqrt{G_{\eta\eta}}} \frac{\partial[(h+\zeta)v\sqrt{G_{\xi\xi}}]}{\partial \eta} + \frac{\partial w}{\partial \sigma} = \\ &= (h+\zeta)(q_{in} - q_{out}) \end{aligned} \tag{3.6}$$

The hydrostatic pressure equation resulted from the vertical momentum equation is:

$$\frac{\partial P}{\partial \sigma} = -g\rho H \tag{3.7}$$

After integration of Equation 3.7, the new hydrostatic equation is:

$$P = P_{atm} + gH \int_\sigma^0 \rho(\xi, \eta, \sigma', t)\, d\sigma' \tag{3.8}$$

The transport equation (Equation 3.9) is formulated, in the horizontal direction, as a conservative form in orthogonal curvilinear coordinates and in the vertical direction as a σ coordinate.

$$\begin{aligned} &\frac{\partial (h+\xi)c}{\partial t} + \frac{1}{\sqrt{G_{\xi\xi}}\sqrt{G_{\eta\eta}}} \left[\frac{\partial[\sqrt{G_{\eta\eta}}(h+\zeta)uc]}{\partial \xi} + \frac{\partial[\sqrt{G_{\xi\xi}}(h+\zeta)vc]}{\partial \eta} \right] + \frac{\partial \omega c}{\partial \sigma} = \\ &= \frac{h+\zeta}{\sqrt{G_{\xi\xi}}\sqrt{G_{\eta\eta}}} \left[\frac{\partial}{\partial \xi} \left(D_H \frac{\sqrt{G_{\eta\eta}}}{\sqrt{G_{\xi\xi}}} \frac{\partial c}{\partial \xi} \right) + \frac{\partial}{\partial \eta} \left(D_H \frac{\sqrt{G_{\xi\xi}}}{\sqrt{G_{\eta\eta}}} \frac{\partial c}{\partial \eta} \right) \right] + \\ &+ \frac{1}{h+\zeta} \frac{\partial}{\partial \sigma} \left(D_V \frac{\partial c}{\partial \sigma} \right) - \lambda_h (h+\zeta) c + S \end{aligned} \tag{3.9}$$

With D_H and D_V the horizontal and vertical diffusion coefficient respectively, λ_h representing the first order decay process and S the source and outcome terms, per unit area, due to discharge of water and exchange of heat through the free surface.

3.3 Boundary Conditions

3.3.1 Flow Boundary Conditions

A set of initial and boundary conditions for water levels and horizontal velocities must be specified in order to achieve a good modelling work. There are two types of boundaries: the open and the closed boundaries. The open boundaries are also called as "water-water" boundaries. In a numerical model, open boundaries are introduced to restrict the computational area and the computational effort. The closed boundaries are the "natural" boundaries of the study area, for example coast lines and river banks. The solution of the shallow water equations can be split in a steady state solution and a transient solution. The steady state solution is completely dependent on the boundary conditions.

Delft3D-FLOW assumes the flow at the open boundaries as sub-critical, which means that the magnitude of the flow is smaller than the velocity of wave propagation. Sub-critical flow means that the Froude number (Equation 3.10) is smaller than 1.

$$Fr = \frac{|U|}{\sqrt{gH}} \tag{3.10}$$

In the σ coordinate system, the free surface ($\sigma = 0$ or $z = \xi$) and the bottom ($\sigma = -1$ or $z = -d$) are σ coordinate, and ω is the vertical velocity relative to the σ plan. The impermeability of the surface ($\sigma = -1$) and the bottom ($\sigma = 0$) is zero.

At the seabed, the boundary conditions are:

$$\frac{\nu_V}{H}\frac{\partial u}{\partial \sigma}\bigg|_{\sigma=-1} = \frac{1}{\rho_0}\tau_{b\xi} \tag{3.11}$$

and

$$\frac{\nu_V}{H}\frac{\partial v}{\partial \sigma}\bigg|_{\sigma=-1} = \frac{1}{\rho_0}\tau_{b\eta} \tag{3.12}$$

With $\tau_{b\xi}$ and $\tau_{b\eta}$ as the components of the bed stress in ξ- and η- direction, respectively. For 3D models, the bed shear stress is related to the current just over the bottom:

$$\vec{\tau}_{b_{3D}} = \frac{g\rho_0 \vec{u}_b |\vec{u}_b|}{C_{3D}^2} \tag{3.13}$$

Where $|\vec{u}_b|$ is the magnitude of the horizontal velocity in the first layer and C_{3D} the 3D Chezy coefficient. The boundary conditions of the momentum equations at the free surface are:

$$\frac{\nu_V}{H}\frac{\partial u}{\partial \sigma}\bigg|_{\sigma=0} = \frac{1}{\rho_0}|\vec{\tau}_s|\cos(\theta) \tag{3.14}$$

and

$$\frac{\nu_V}{H}\frac{\partial v}{\partial \sigma}\bigg|_{\sigma=0} = \frac{1}{\rho_0}|\vec{\tau}_s|\sin(\theta) \tag{3.15}$$

Whit $|\overrightarrow{\tau}_s|$ as the magnitude of the wind shear-stress and θ the angle between the wind stress vector and the local direction. Without wind, the stress at the free surface is zero.

To reduce the reflections at the open boundary, it was derived a first order weakly reflecting boundary condition. Assuming zero flow along the boundary, the zero order boundary condition can be obtained using the Riemann invariants. The Riemann invariants are two waves, moving in opposite direction where propagation speed is $R = U \pm 2\sqrt{gH}$. At the open boundary, the incoming wave should be specified. The linearised Riemann invariant is given by:

$$U + 2\sqrt{gH} = U + 2\sqrt{g(h+\zeta)} \approx U + 2\sqrt{gh} + \zeta\sqrt{\frac{g}{h}}, \qquad \frac{|\zeta|}{h} \ll 1 \tag{3.16}$$

In the computational part, the type of boundary conditions are:

- Water level:

$$\zeta = F_\zeta(t) + \delta_{atm} \tag{3.17}$$

- Velocity:

$$U = F_U(t) \tag{3.18}$$

- Discharge:

$$Q = F_Q(t) \tag{3.19}$$

- Neumann:

$$\frac{\partial \zeta}{\partial \overrightarrow{n}} = f(t) \tag{3.20}$$

- Riemann invariant:

$$U \pm \zeta\sqrt{\frac{g}{h}} = F_R(t) \tag{3.21}$$

Stelling (1983) added the time-derivative of the Riemann invariant, in water level and velocity boundary conditions, to make the boundaries less reflective and to reduce the spin-up time of a model, resulting:

- Water level boundary (Equation 3.17):

$$F_\zeta(t) = \zeta + \alpha\frac{\partial}{\partial t}\left[U \pm 2\sqrt{gH}\right], \qquad \alpha = T_d\sqrt{\frac{H}{h}} \tag{3.22}$$

- Velocity boundary (Equation 3.18):

$$F_U(t) = U + \alpha\frac{\partial}{\partial t}\left[U \pm 2\sqrt{gH}\right], \qquad \alpha = T_d \tag{3.23}$$

With T_d the time that a free surface wave takes to travel from the left boundary to the right boundary of the model domain. In ocean, T_d and the period of the tidal forcing are of the same order.

At the closed boundaries, two boundary conditions are recommended: the normal flow to the boundary and the shear-stress along the boundary. If the normal flow specifies no flow through the boundary, this means that the boundary is impermeable. Partial slip is the condition for the shear-stress along the boundary however for large-scale simulations, the influence of the shear-stress along the closed boundary can be ignored.

3.3.2 Transport Boundary Conditions

The advection is the principal vehicle of horizontal transport of dissolved substances in rivers, estuaries and coastal seas, being the horizontal diffusion in flow direction the second most important. At the open boundary, during inflow, it is necessary a boundary condition to describe the advection transport but, during outflow, no boundary condition is needed. The concentration established at inflow can be determined by the concentration at outflow of the former ebb period.

Usually only the background concentration is known from measurements or from a larger model area, so is used the Thatcher-Harleman boundary condition (Thatcher and Harleman, 1972) based on the combination of the concentration in the interior area with the return time, which does not completely fix the concentration at the background value. The return time depends on the renovation of water at the open boundary.

The transport of heat and salt is described by the advection-diffusion equation. The concentration is determined by:

$$\frac{\partial C}{\partial t} + \frac{U}{\sqrt{G_{\xi\xi}}}\frac{\partial C}{\partial \xi} = 0 \tag{3.24}$$

At outflow, if the concentration differs from the boundary condition at inflow, there is a discontinuity in the concentration at the turn of the flow. Leading to a more time consuming transition of the concentration at the boundary from the outflow value to the inflow value, depending on the refreshment of water in the boundary region. This transition time is called the return time or the memory-effect for open boundary, and is formulated as:

$$C(t) = C_{out} + \frac{1}{2}(C_{bnd} - C_{out})\left(cos\left(\pi\frac{T_{ret} - t_{out}}{T_{ret}}\right) + 1\right), \qquad 0 \leq t_{out} \leq T_{ret} \tag{3.25}$$

Where C_{out} is the computed concentration at the open boundary at the last time of outward flow, C_{bnd} is the background concentration, t_{out} is the elapsed time since the last outflow and T_{ret} is the constituent return period. When the flow turns inward ($t_{out} = 0$), the concentration is set equal to C_{out}. During the interval $0 \leq t_{out} \leq T_{ret}$, the concentration will return to the background concentration C_{bnd}. After that period, the concentration will remain C_{bnd}. The vertical diffusive flux through the free surface and bed is zero except for the heat flux through the free surface.

3.4 Turbulence

In 3D shallow water flow, the stress and diffusion tensor are anisotropic. The horizontal eddy viscosity (ν_H) and diffusivity (D_H) coefficients are much larger than the vertical coefficients ($\nu_H >> \nu_V$ and $D_H >> D_V$). The horizontal coefficients are a superposition of: a part due to molecular viscosity, a part due to 2D-turbulence and a part due to 3D-turbulence. The vertical coefficients are determined with four types of closure models: constant coefficient model, Algebraic Eddy viscosity Model (AEM), $k-L$ turbulence model and $k-\varepsilon$ turbulence model. Where k is the turbulent kinetic energy, ε the dissipation rate of turbulent kinetic energy and L the mixing length.

The 3D eddy viscosity equation is:

$$\nu_{3D} = c'_{\mu} L \sqrt{k} \tag{3.26}$$

and the diffusivity equation is:

$$D_{3D} = \frac{\nu_{3D}}{\sigma_c} \tag{3.27}$$

With c'_{μ} a constant determined by calibration, L the mixing length, k the turbulent kinetic energy and σ_c the Prandtl-Schmidt number.

$$\sigma_c = \sigma_{c_0} F_{\sigma}(Ri) \tag{3.28}$$

Where σ_{c_0} is a constant dependent on the substance and $F_{\sigma}(Ri)$ is a damping function that depends on the density stratification via the gradient of Richardson's number (Richardson, 1920). Stable stratification leads to dumping of turbulent mixing while unstable stratification leads to a higher mixing.

$$Ri = \frac{-g\frac{\partial \rho}{\partial z}}{\rho\left[\left(\frac{\partial u}{\partial z}\right)^2 + \left(\frac{\partial v}{\partial z}\right)^2\right]}, \quad \begin{cases} Ri \geq 0 & Stable\ Stratification \\ Ri \leq 0 & Unstable\ Stratification \end{cases} \tag{3.29}$$

In the $k-\varepsilon$ turbulence model, transport equations must be solved for both the turbulent kinetic energy k and for the energy dissipation ε. The mixing length L is then determined from ε and k according to:

$$L = c_D \frac{k\sqrt{k}}{\varepsilon} \tag{3.30}$$

In transport equations for $k-\varepsilon$ turbulence model, the dominating terms are the production, buoyancy and dissipation, and the horizontal length scales are larger than the vertical ones. So the transport equation for k is:

$$\begin{aligned} &\frac{\partial k}{\partial t} + \frac{u}{\sqrt{G_{\xi\xi}}}\frac{\partial k}{\partial \xi} + \frac{v}{\sqrt{G_{\eta\eta}}}\frac{\partial k}{\partial \eta} + \frac{\omega}{d+\zeta}\frac{\partial k}{\partial \sigma} = \\ &= \frac{1}{(d+\zeta)^2}\frac{\partial}{\partial \sigma}\left(D_k \frac{\partial k}{\partial \sigma}\right) + P_k + P_{kw} + B_k - \varepsilon \end{aligned} \tag{3.31}$$

and for ε is:

$$\frac{\partial \varepsilon}{\partial t} + \frac{u}{\sqrt{G_{\xi\xi}}}\frac{\partial \varepsilon}{\partial \xi} + \frac{v}{\sqrt{G_{\eta\eta}}}\frac{\partial \varepsilon}{\partial \eta} + \frac{\omega}{d+\zeta}\frac{\partial \varepsilon}{\partial \sigma} = \tag{3.32}$$

$$= \frac{1}{(d+\zeta)^2}\frac{\partial}{\partial \sigma}\left(D_\varepsilon \frac{\partial \varepsilon}{\partial \sigma}\right) + P_\varepsilon + P_{\varepsilon w} + B_\varepsilon - c_{2\varepsilon}\frac{\varepsilon^2}{k}$$

Where the eddy diffusivity terms are:

$$D_k = \frac{\nu_{mol}}{\sigma_{mol}} + \frac{\nu_{3D}}{\sigma_k} \tag{3.33}$$

and

$$D_\varepsilon = \frac{\nu_{3D}}{\sigma_k} \tag{3.34}$$

The production terms are:

$$P_k = \nu_{3D}\frac{1}{(d+\zeta)^2}\left[\left(\frac{\partial u}{\partial \sigma}\right)^2 + \left(\frac{\partial v}{\partial \sigma}\right)^2\right] \tag{3.35}$$

and

$$P_\varepsilon = c_{1\varepsilon}\frac{\varepsilon}{k}P_k \tag{3.36}$$

The buoyancy flux terms are:

$$B_k = \frac{\nu_{3D}}{\rho\sigma_\rho}\frac{g}{H}\frac{\partial \rho}{\partial \sigma} \tag{3.37}$$

and

$$B_\varepsilon = c_{1\varepsilon}\frac{\varepsilon}{k}(1-c_{3\varepsilon})B_k \tag{3.38}$$

Lastly, the calibration terms, given by Rodi (1984), are $c_{1\varepsilon} = 1.44$, $c_{2\varepsilon} = 1.92$ and $c_{3\varepsilon} = 0$ for an unstable stratification or $c_{3\varepsilon} = 1$ for an stable stratification.

3.5 Heat Flux

The sun emits radiation that arrives to Earth in the form of electromagnetic waves. In the atmosphere that radiation is reflected and absorbed by air, clouds and particles. In Delft3D-FLOW, the heat fluxes modelled at the free surface are related with the effects of solar (short wave) and atmospheric (long wave) radiation, and heat losses due to back radiation, evaporation and convection.

The total heat flux through the free surface is:

$$Q_{total} = Q_{sr} + Q_{ar} - Q_{br} - Q_{ev} - Q_{co} \tag{3.39}$$

Where Q_{sr} is the net solar radiation, Q_{ar} the net atmospheric radiation, Q_{br} the back radiation, Q_{ev} the evaporative heat flux and Q_{co} the convective heat flux.

These fluxes can be described by:

- Net solar radiation (short wave):

$$Q_{sr} = \sigma T^4 \tag{3.40}$$

With σ as Stefan-Boltzmann's constant = 5.67×10^{-8} $(Jm^{-2}s^{-1}K^{-4})$ and T the absolute temperature of a black-body in Kelvin (K).

- Net atmospheric radiation (long wave):

$$Q_{ar} = (1-r)\varepsilon\sigma T_a^4 g(F_c) \tag{3.41}$$

With r the reflection coefficient ($r = 0.03$), ε the emissivity factor, T_a the air temperature in Kelvin and $g(F_c)$ the cloud function.

- Back radiation (long wave):

$$Q_{br} = (1-r)\varepsilon\sigma T_s^4 \tag{3.42}$$

With T_s the water surface temperature in Kelvin.

- Evaporative heat flux (latent heat):

$$Q_{ev} = L_v E \tag{3.43}$$

With L_v the latent heat of vaporization and E the evaporation rate.

- Convective heat flux (sensible heat):

$$Q_{co} = R_b Q_{ev} \tag{3.44}$$

With the Bowen ratio (R_b):

$$R_b = \gamma \frac{T_s - T_a}{e_s - e_a} \tag{3.45}$$

Where γ is the Bowen's constant, e_s is the saturated vapour pressure and e_a is the actual vapour pressure.

Delft3D-Flow provides five heat flux models, however it was used the second Heat flux (model 2 - Absolute flux, net solar radiation), which uses the combined net solar radiation (Equation 3.40) and net atmospheric radiation (Equation 3.41). The terms related to heat losses due to evaporation, back radiation and convection are computed by the model. This heat flux model is based on formulations given by Octavio (1977). The source of data for the combined net incoming radiation terms (Q_{sr} + Q_{ar}) must come from direct measurements.

Chapter 4

Model Implementation to the Estuarine and Coastal Regions

The fate of a model simulation is determined by the free model parameters. These parameters reflect the uncertainty on how to model certain physical process, and provide the opportunity to adjust the model using measured data Ribeiro (2015).

This Chapter summarizes the free model parameters in the Delft3D-Flow module, which are considered the most uncertain and important. In section 4.1 is presented the data used to implement and calibrate the model. In section 4.2 is presented the properties of the model's grid including the grid's orthogonality, the number of sigma layers, and the model's numerical bathymetry. Finally, in section 4.3 is presented the model's tidal and salt and heat transport calibrations.

4.1 Data Presentation

The inputs that are used to perform numerical simulations are crucial to the modelling process. These inputs are responsible for the model's accuracy to predict the physical processes. This section presents the data that were used to generate the numerical bathymetry applied on the model's grid, the ocean, river and atmospheric time series applied on model's boundaries, and the field data used to calibrate the water level and the model's salt and heat transport module.

4.1.1 Bathymetry

The coastal region bathymetry data was constructed based on General Bathymetric Chart of the Oceans (GEBCO). The bathymetry data used for Minho estuary was obtained and interpolated from LIDAR data given by DGT (Direção Geral do Território), collected in 2011 with a spatial resolution of 2 meters. The data was received in ETRS89 (European Terrestrial Reference System 1989) as reference system and in Cascais Helmert 38 Altimetric Datum as the vertical reference. It was necessary to transform that reference into WGS 1984 Datum with the support of ArcGis software.

The bathymetry used in Lima estuary was obtained from Hidrodata company, with a spatial resolution of 5 meters. It was measured between October 2002 and December 2003 in three surveys: Hydrographic Survey 0255-ARN-1002 (main port area), Hydrographic Survey 0286-ARN-0503A (near port entrance) and Hydrographic Survey 0330-ARN-1203A (area between bridges) (Vale, 2008). The final files with the bathymetric samples were prepared in .xyz format.

4.1.2 Ocean Boundary

In this section, are presented the data used for the flow and transport conditions imposed at the model's open boundaries. The flow conditions were given by TOPEX/Poseidon (www.jpl.nasa.gov) (MacMillan et al., 2004). The TOPEX/Poseidon method is based on a global ocean tide model (NAO.99b model), representing the major 13 constituents with a spatial resolution of 0.25º and is estimated from 5 years of TOPEX/Poseidon altimeter data. In model's configuration, it was applied the astronomic forcing type at the model's open boundary.

The transport conditions were calculated based on inputs from Copernicus Marine Environment Monitoring Service (CMEMS, www.marine.copernicus.eu). From CMEMS, the project MyOcean has the objective to set up (definition, design, development and validation) an integrated European capability for ocean monitoring and forecasting. This project supplied the daily salinity and water temperature in 3 km horizontal resolution for 50 layers depth from the surface up to 5000 m bottom. The period of extracted data was from January 2012 to March 2013 and the spatial domain was from 40º to 43º N and 7º to 10º W. The flow and transport conditions were interpolated across the open boundaries using Matlab scripts.

4.1.3 Atmospheric Boundary

The meteorological data used to implement the forcing at model's atmospheric boundary, was obtained from the European Centre for Medium-Range Weather Forecasts (ECMWF, www.ecmwf.int). The ECMWF provides a global atmospheric reanalysis model continuously updated in real time - the ERA-Interim. The data assimilation system, used to produce the model ERA-Interim, is based in the dataset IFS (Cy31r2) released on 2006. The system includes a 4-dimensional variation (4D-Var) with a 12 hour analysis window in a 3 km resolution.

The data supplied from ERA-Interim has a temporal resolution of 3 hours and was used to apply the heat flux and wind process of Delft3D-FLOW. The heat flux module requires relative humidity (%), air temperature (ºC) and net solar radiation ($Jm^{-2}s^{-1}$), and the wind process requires the wind velocity (ms^{-1}) and direction in degrees.

The data was extracted from ERA-Interim model between January 2012 and March 2013, with a spatial domain that extends from 40º to 43º N and 7º to 10º W. Figure 4.1 shows the wind roses of the monthly average direction and velocity wind between February 2012 and February 2013. As it is seen in the figure, the predominant wind regime for the summer months (e, f and g) was from South East, and the predominant regime for the winter months (k, l and m) was from South.

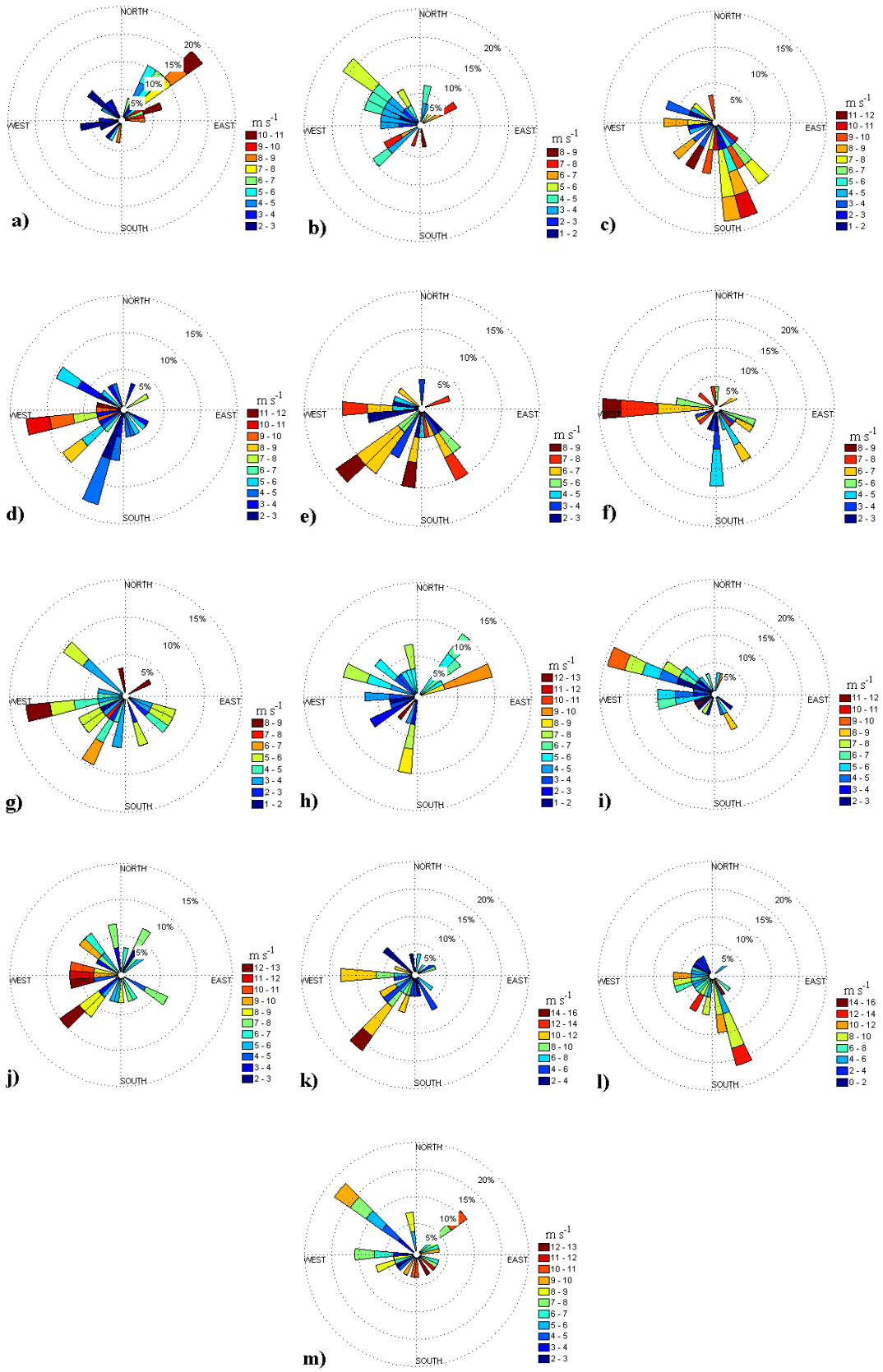

Figure 4.1: Wind roses representing the month wind average direction and velocity between February 2012 and February 2013. a) February 2012, b) March, c) April, d) May, e) June, f) July, g) August, h) September, i) October, j) November, k) December, l) January 2013, m) February 2013.

4.1.4 River Boundary

The daily series of river discharge data was obtained from the Confederación Hidrográfica del Miño-Sil (www.chminosil.es) for Minho river, while for Lima river was obtained from the Portuguese National Information System of Water Resources (www.snirh.pt). For Minho river, the data was taken from Frieira station in Spain, and for Lima river was taken from Ponte da Barca station in Portugal. Figure 4.2 shows the monthly average rivers discharge between February 2012 and February 2013. This figure shows that during summer (June, July and August) the average Minho river discharge was 100 m^3s^{-1} and Lima river discharge was 20 m^3s^{-1}. During winter (December, January and February) the average Minho river discharge was 340 m^3s^{-1} and Lima river discharge was 80 m^3s^{-1}.

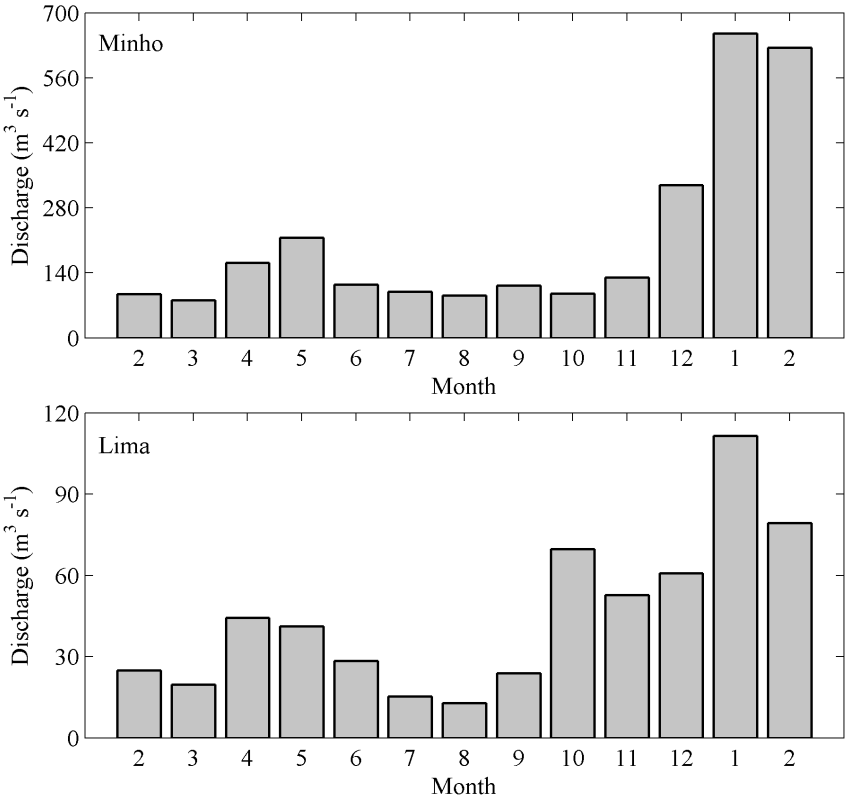

Figure 4.2: Monthly average river discharge between February 2012 and February 2013.

4.1.5 Field Data

Zacarias (2007) studied the influence of bathymetry and river flow on tidal propagation in Minho estuary under the ECOIS (Estuarine Contributions to Inner Shelf Dynamics) project. This project aims to evaluate how variability in river flow is reflected in Douro and Minho outflows. The water level data survey was made in six locations (Barra, Caminha, Seixas, V. N. Cerveira, Segadães and Viana do Castelo) during three campaigns between October 2005 and February 2007. Figure 4.3 shows the position of the tide gauges from where the sea surface elevation measurements were performed.

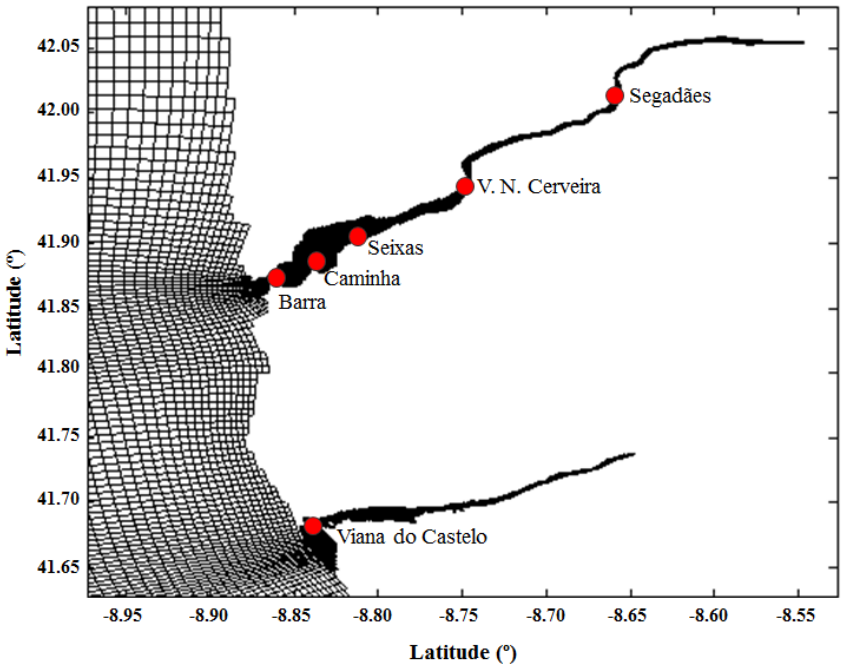

Figure 4.3: Part of the numerical grid contemplating both estuaries. Red dots are the tide gauge stations used for the extraction of the sea surface elevation.

The first campaign was performed between 8th September and 10th October 2005, the second campaign between 20th February and 19th March 2006 and the third campaign between 25th January and 5th February 2007. The first campaign took place during minimum flow and the second and third campaigns during winter conditions, which means under high fluvial discharges. For Viana do Castelo, the data was obtained by the Portuguese Hydrographic Institute. It was preformed the harmonic analysis to water level data, obtaining 45 harmonic constituents. These harmonics were used in this work to calibrate the tidal wave on both estuaries.

To perform the calibration of the model's salt and heat transport module, it was used the water temperature and salinity data measured one day per month between February 2012 and February 2013 in a campaign performed by Vieira et al. (2015) on both estuaries. The sampling was made along seven transects in each estuary (Figure 2.1). The data collection was made in three locations (south, middle and north margin) of each transect and, in each location, were made three replicates in the middle of the water column. In Minho, the sampling locations were in the lower part of the estuary and in Lima the locations were in the lower part (near the mouth) and in the middle area (a shallow salt marsh zone).

It was used a GPS to determine and validate the coordinates of the sampling locations and a probe to determine the depth in all transect locations. Table 4.1 shows the coordinates and the average depths for each site.

Table 4.1: Coordinates and average depths of each site for all the transects. Site 1 is located on the south margin, the Site 2 on the middle margin and the Site 3 on the north margin.

Estuary	Site's Coordinates	Transect						
		T1	T2	T3	T4	T5	T6	T7
Minho	Site 1	41° 52' 02" N 08° 51' 11" W	41° 52' 23" N 08° 50' 42" W	41° 52' 47" N 08° 50' 23" W	41° 53' 06" N 08° 49' 58" W	41° 53' 28" N 08° 49' 35" W	41° 53' 55" N 08° 49' 11" W	41° 54' 12" N 08° 48' 44" W
	Depth (m)	1.5	1.0	1.5	1.0	1.0	1.5	2.0
	Site 2	41° 52' 10" N 08° 51' 35" W	41° 52' 32" N 08° 51' 03" W	41° 52' 52" N 08° 50' 44" W	41° 53' 16" N 08° 50' 23" W	41° 53' 37" N 08° 49' 59" W	41° 53' 58" N 08° 49' 26" W	41° 54' 15" N 08° 48' 57" W
	Depth (m)	2.0	1.5	2.0	1.5	1.5	2.5	2.5
	Site 3	41° 52' 24" N 08° 51' 52" W	41° 52' 43" N 08° 51' 28" W	41° 53' 01" N 08° 51' 07" W	41° 53' 32" N 08° 50' 52" W	41° 53' 51" N 08° 50' 20" W	41° 54' 06" N 08° 49' 42" W	41° 54' 26" N 08° 49' 17" W
	Depth (m)	3.0	1.5	2.0	1.0	2.0	1.5	1.5
Lima	Site 1	41° 40' 48" N 08° 50' 15" W	41° 40' 59" N 08° 49' 43" W	41° 41' 09" N 08° 49' 26" W	41° 41' 22" N 08° 49' 14" W	41° 41' 23" N 08° 48' 44" W	41° 41' 24" N 08° 08' 14" W	41° 41' 22" N 08° 47' 35" W
	Depth (m)	4.0	4.0	4.0	1.5	2.0	2.0	1.5
	Site 2	41° 40' 50" N 08° 50' 25" W	41° 41' 07" N 08° 49' 58" W	41° 41' 17" N 08° 49' 37" W	41° 41' 26" N 08° 49' 20" W	41° 41' 33" N 08° 48' 54" W	41° 41' 36" N 08° 48' 26" W	41° 41' 29" N 08° 47' 38" W
	Depth (m)	6.0	5.0	5.0	3.0	2.5	3.0	2.0
	Site 3	41° 40' 58" N 08° 50' 35" W	41° 41' 09" N 08° 50' 08" W	41° 41' 21" N 08° 49' 47" W	41° 41' 30" N 08° 49' 28" W	41° 41' 40" N 08° 49' 02" W	41° 41' 44" N 08° 48' 35" W	41° 41' 36" N 08° 47' 50" W
	Depth (m)	5.0	4.0	4.0	3.0	2.5	2.5	2.0

4.2 Model Establishment

One of the most important parts in the modelling process is the implementation of the parameters that will be used by the model. In this study, the modelling procedure starts with the construction of the model's grid following the methodology present in Deltares (2014b). This grid is the base for other model implementations like the bathymetry, observation and dry points.

It was constructed a single domain spherical coordinated grid representing the main body of the hydrodynamic system (Figure 4.3), including the Minho and Lima estuaries and adjacent coastal region. The total covered area includes 20 km from the coast to open sea, 22 km for Minho river and 17.5 km for Lima river. The total grid size is 898 cells in M-direction (longitude) and 146 in N-direction (latitude) with a total grid elements of 33790.

The dimensions of each offshore cell are 800 $\times$ 800 m and near coastline are 200 $\times$ 200 m, but in order to represent in the best way possible the interactions inside estuaries it was necessary to increase the resolution of the grid. Therefore, in Minho estuary the size of each cell is 50 $\times$ 70 m and in Lima estuary is 20 $\times$ 30 m.

The grid generation was a challenging process mainly due to the complex geometry of Lima mouth. In this area exists a groin which complicates the geometry of the estuary and involves more work and time. This grid was made using tools for irregular grids, and, during the process, it was necessary to check the orthogonality a couple of times. The achieved orthogonality, between 0.01 and 0.02, was an excellent result because fulfils the recommended range proposed by Deltares (2014b).

The model uses 10 sigma layers (with 5% of depth in layer 1, 2 and 3, 10% in layer 4, 5, 6, 7 and 8, 15% in layer 9 and 20% in layer 10). This distribution considers that the most important dynamics occurs in the first layers, and therefore was necessary to refine the surface layers to improve the model's capacity to resolve mixing processes.

The bathymetry was created by interpolating the surveys data mentioned in section 4.1.1 to the numerical grid. Using tools and mechanisms available in Deltares (2014c), the numerical grid was generated with chart datum referenced to the Portuguese hydrographic null (Figure 4.4).

The time step used in the model was 30 seconds in order to account the Courant-Friedrichs-Lewy number (Courant et al., 1928). The CFL_{wave} number is presented in Deltares (2014a) and is represented by equation 4.1.

$$CFL_{wave} = 2\triangle t\sqrt{gH}\sqrt{\frac{1}{\triangle x^2}+\frac{1}{\triangle y^2}} < 1 \tag{4.1}$$

Where $\triangle t$ is the time step (minutes), g is the acceleration of gravity (ms^{-2}), H is the water column (m) and $\triangle x = \sqrt{G_{\xi\xi}}$ and $\triangle y = \sqrt{G_{\eta\eta}}$ are the smallest grid spaces in ξ- and η- direction of the physical space. This time step is very important because if it is too large regarding to grid cell size and water depth, probably a large number of disequilibrium's will occur. According to Deltares (2014a), Courant number should not exceed a value of 10, but for problems with small variations in time and space, this number can be larger. In this work, the maximum Courant's number was 12.

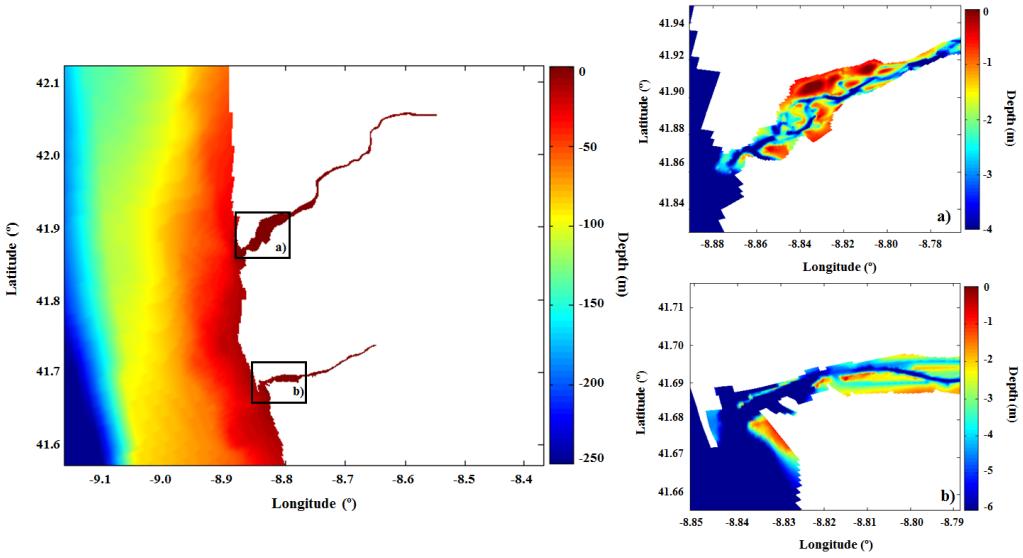

Figure 4.4: Study area bathymetry. a) Detailed part of Minho estuary and b) detailed part of Lima estuary.

The background horizontal viscosity and diffusivity were uniformly set to 10 m^2s^{-1}. The components of the heat flux model (section 3.5) and wind process were obtained from ERA-Interim atmospheric reanalysis. The two discharge points (freshwater input) were defined as outflows representing the Minho and Lima rivers. These time series were described in section 4.1.4. This model configuration was set up to run over fourteen months with one month of warm up.

4.3 Model Calibration

Physical models are based on mathematical equations that try to represent natural processes occurring in nature. The aim of this work consists in a coupled modelling of Minho and Lima estuaries, and as such, the calibration refers to the processes inside the two estuaries, intending to ensure the best reproduction of the observations in these systems. To achieve that, the model needs some inputs and it is necessary to perform the model calibration to get the best representation of the estuarine processes.

The model predictions are reliable only if the model assumptions, inputs, and parameters estimates are reliable too. The presence of variables in process-based models is a direct consequence of the need to simplify reality or even represent unknown or sub-scale processes, but these parameters do not represent measurable attributes of the study area, so the generated values have to be determined through calibration using input/output interactions. Thus, the calibration objective is to determine the optimum parameter setting to compute correctly the flows according to the morphological characteristics of the study area (Ribeiro, 2015).

The methodology used for model calibration was proposed by Dias and Lopes (2006):

- Visual observation of the model's capacity to represent, inside the model domain, the tide propagation;
- Quantification of the adjustment between model predictions and observations, including the comparison between observed and predicted tidal amplitudes and phases;
- Temporal analysis between the observed and predicted water temperature and salinity (including the quantification of the model's performance).

Both in the water level and salinity and water temperature calibrations, were necessary several attempts with a large numbers of runs that were time consuming, to achieve the results presented in subsections 4.3.1 and 4.3.2.

4.3.1 Water Level

The model predictions for water level were compared with observations, at the six stations presented in section 4.1.5. The time series were reproduced by harmonic synthesis and the harmonic constituents used for the tide reconstruction were the MSF, $2Q_1$, Q_1, O_1, NO_1, K_1, J_1, OO_1, UPS_1, N_2, M_2, S_2, ETA_2, MO_3, M_3, MK_3, SK_3, MN_4, M_4, MS_4, S_4, $2MK_5$, $2SK_5$, $2MN_6$, M_6, $2MS_6$, $2SM_6$, $3MK_7$ and M_8.

The tidal propagation was adjusted with the bottom roughness. For that purpose it was used the Manning's coefficients. Those coefficients are obtained following the Manning's formulation dependent on the Chezy coefficient (Equation 4.2) (Deltares, 2014a).

$$n = \frac{\sqrt[6]{H}}{C} \tag{4.2}$$

Where n is the Manning coefficient ($m^{-1/3}s$), H the water column (m) and C the Chezy coefficient ($m^{1/2}s^{-1}$). Fry and Aubrey (1990) state that an increase in the bottom roughness will produce an increase in the tidal wave phase on high tide and a decrease on low tide. Considering this fact, the Manning coefficients values were adjusted several times, in order to improve the tidal produced by the model and thus calibrate the hydrodynamic. The applied Manning values were: $n = 0.016\ m^{-1/3}s$ for depths $<$ -25 m, and $n = 0.022\ m^{-1/3}s$ for depths $\geq$ -25 m. These values were based on Vale (2008).

The first step in calibration consists in visually comparing the observed and predicted sea surface height related with tide propagation. This visual comparison showed a very good representation of the water level by the model (Figure 4.5). In this figure it is visualized that the model follows the behaviour of the observed measurements in all the six stations.

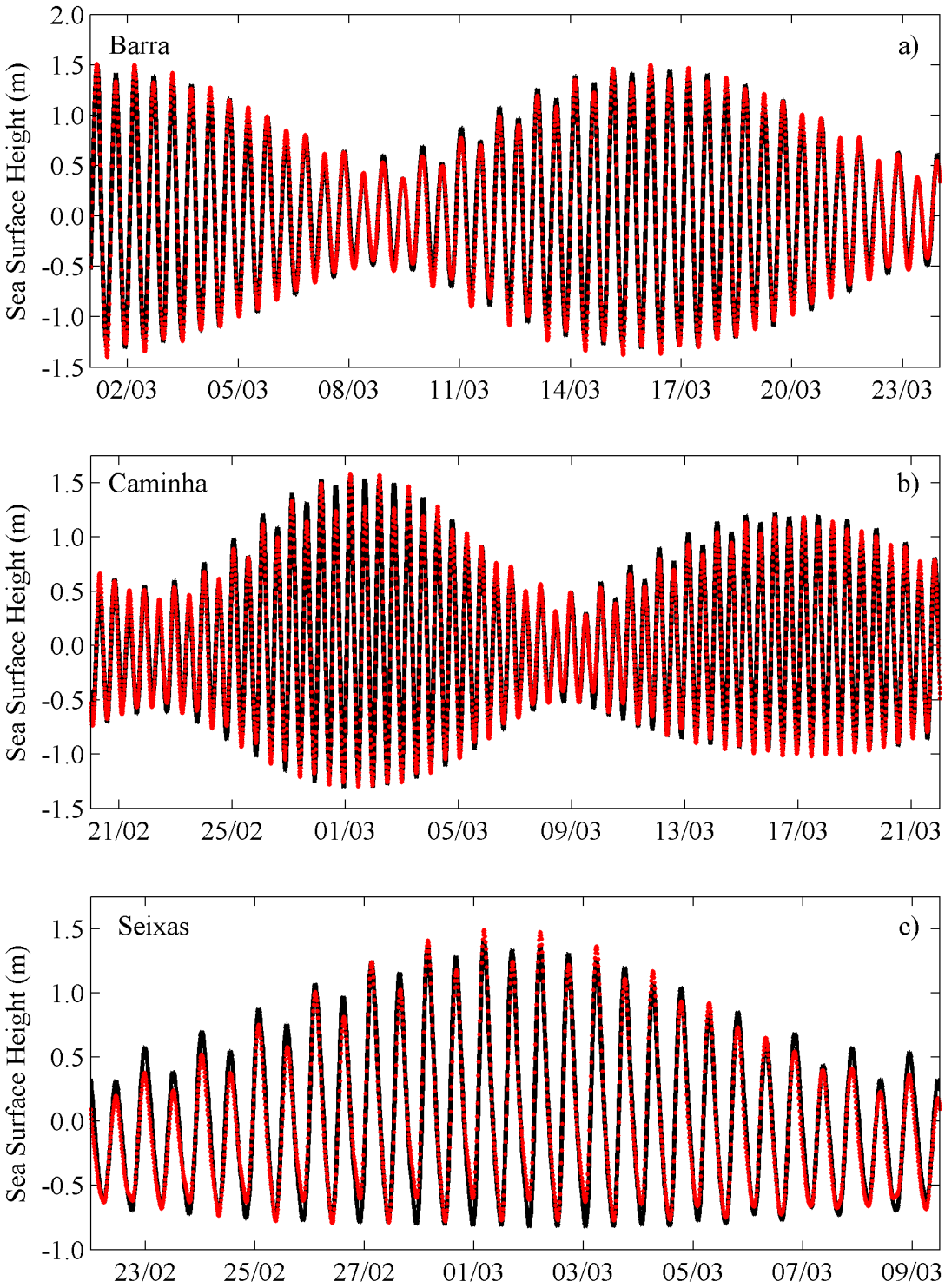

Figure 4.5: Comparison between predicted and observed sea surface height. The black line represents the model predictions and the red dots the observed measurements for a) Barra, b) Caminha and c) Seixas.

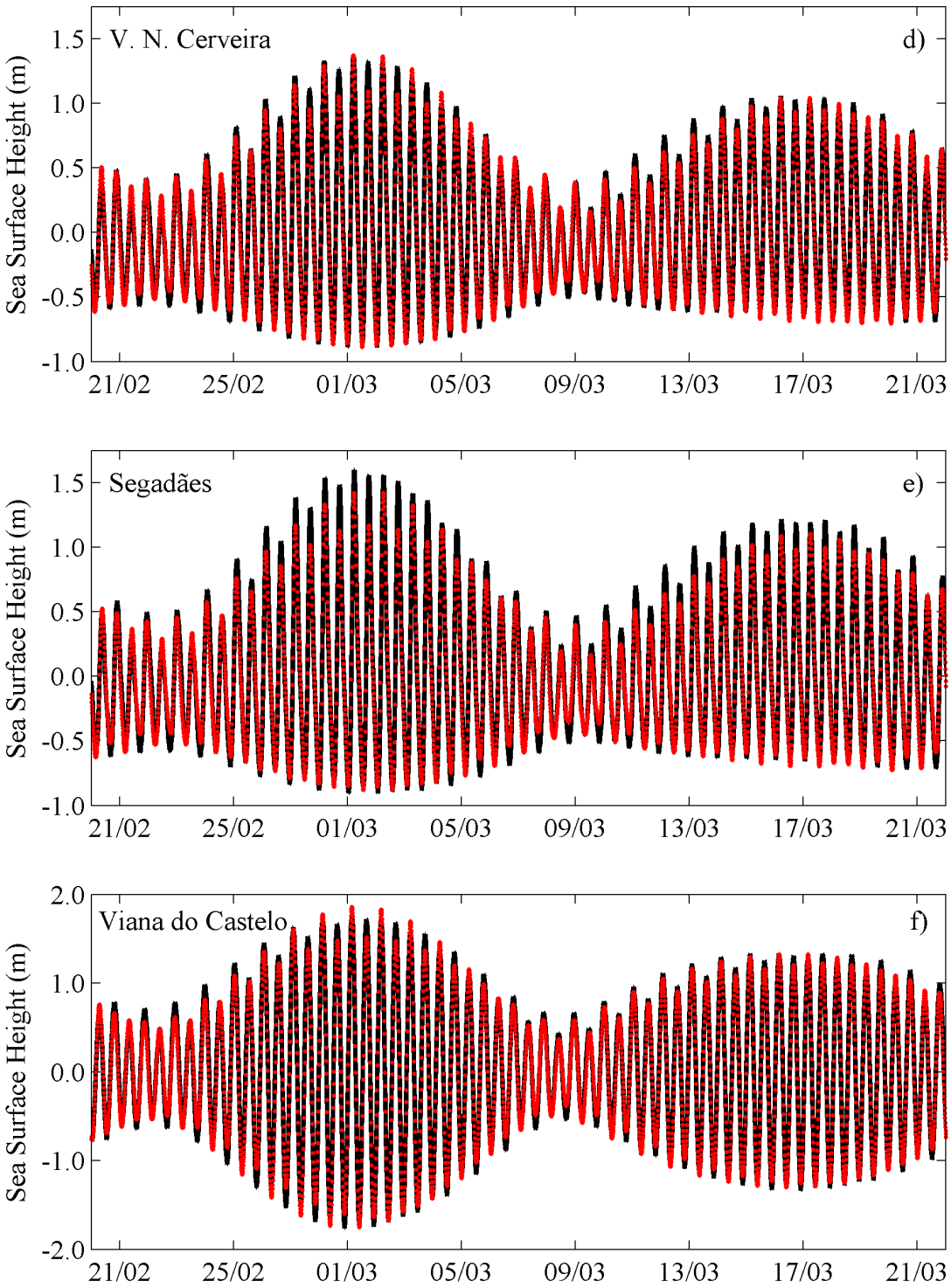

Figure 4.5: (Continued) Comparison between predicted and observed sea surface height. The black line represents the model predictions and the red dots the observed measurements for d) V. N. Cerveira, e) Segadães and f) Viana do Castelo.

The second step comprises the calculation of *RMSE* (Root Mean Square Error) (Atwater and Ball, 1978) and *Skill* (Willmott, 1981) parameters to quantify the model performance and then to compare the observed and predicted tidal amplitudes and phases. The *RMSE* and *Skill* expressions (Dias et al., 2009) are represented by Equation 4.3 and 4.4, respectively.

$$RMSE = \sqrt{\frac{\sum_{i=1}^{N}[\zeta_p(t_i) - \zeta_h(t_i)]^2}{N}} \tag{4.3}$$

$$Skill = 1 - \frac{\sum|\zeta_p - \zeta_h|^2}{\sum(|\zeta_p - \overline{\zeta_h}| + |\zeta_h - \overline{\zeta_h}|)^2} \tag{4.4}$$

Where $\zeta_p(t_i)$ is the predicted water level and $\zeta_h(t_i)$ is the water level obtained with harmonic integration, both at t_i time. In equation 4.3, N is the number of time steps, and in equation 4.4, the horizontal bar represent a temporal mean. Dias et al. (2009) proposed that an *RMSE* with a relative error lower than 5% express an excellent agreement between model predictions and observations, and a relative error between 5% and 10% represent a very good concordance. A *Skill* number higher than 0.95 indicates an excellent correlation between model predictions and observations (Dias et al., 2009).

The *RMSE* and *Skill* were calculated, during one month, for the six locations presented in Figure 4.3, and the results are presented in Table 4.2. The best model results were obtained in Barra and Viana do Castelo, with *RMSE* values of 0.082 and 0.096 m, and relative errors of 3.90 and 3.84%, respectively. The worst model results were found for V. N. Cerveira and Segadães, with an *RMSE* of 0.096 and 0.106 m, and relative errors of 6.40 and 6.52%, respectively.

For Viana do Castelo, the *RMSE* value of 0.096 m can be regarded as an excellent result when compared with Vale (2008), who obtained a value of 0.147 m for the same location. In all sites the *Skill* value was higher than 0.990 which, according to Dias et al. (2009), shows that the model results and observations has an excellent correlation between each other.

The study of sea surface elevations and currents can be done through harmonic analysis. This method solves the harmonic constituents using the least squares technique to examine the specific frequencies of each constituent (Ribeiro, 2015). The tidal signal is modelled as the sum of sinusoidal sets with specific frequencies, and each one of them is specified by various combinations of sums and differences of six fundamental frequencies originated by the planetary motions (Godin, 1972).

Table 4.2: Error values for tidal water levels.

Estuary	Site	RMSE (m)	Relative Error (%)	Skill
Minho	Barra	0.082	3.90	0.997
	Caminha	0.085	4.25	0.996
	Seixas	0.105	5.53	0.991
	V. N. Cerveira	0.096	6.40	0.991
	Segadães	0.106	6.52	0.990
Lima	Viana do Castelo	0.096	3.84	0.996

The harmonic analysis was made using a package of MATLAB routines called T_TIDE (Pawlowicz et al., 2002). This package has an important characteristic: calculates the amplitude and phase with a 95% confidence interval. This analysis was applied to model predictions at the six study locations. The results for the most important semi-diurnal constituents (M_2 and S_2) and diurnal constituents (O_1 and K_1) are presented in Table 4.3, with the respective differences between predicted and observed harmonics data.

For M_2 and S_2 constituents, the amplitude agreement between observed and predicted data is very good with an average value of 5 cm in M_2 and 2 cm in S_2, except in Seixas where exists a difference in M_2 of 16 cm. Relatively to phase, the results can be considered good. For M_2 the minimum difference was 0.32º and the maximum was 7.97º, and for S_2 were 1.10º and 8.57º, respectively. Regarding diurnal constituents (O_1 and K_1), the amplitude results are excellent for all the locations with only 1 cm of difference between model and data.

Table 4.3: Harmonic analysis results, for the M_2, S_2, O_1 and K_1 constituents, comparing the observed and predicted constituents in all tide gauges.

			Amplitude (m)			Phase (º)		
Estuary	Site	Harmonic Constituent	Data	Model	Dif	Data	Model	Dif
Minho	Barra	M_2	0.95	0.95	0.00	86.97	86.37	-0.60
		S_2	0.46	0.45	-0.01	127.14	123.88	-3.26
		O_1	0.06	0.06	0.00	324.42	40.98	-283.44
		K_1	0.06	0.06	0.00	64.91	78.52	13.61
	Caminha	M_2	0.85	0.92	0.07	94.23	92.38	-1.85
		S_2	0.36	0.40	0.04	141.49	132.92	-8.57
		O_1	0.07	0.06	-0.01	340.95	48.09	-292.86
		K_1	0.05	0.06	0.01	91.45	83.87	-7.58
	Seixas	M_2	0.72	0.88	0.16	106.90	104.54	-2.36
		S_2	0.26	0.27	0.01	156.00	147.74	-8.26
		O_1	0.05	0.05	0.00	329.31	57.63	-271.68
		K_1	0.09	0.06	-0.03	92.01	89.57	-2.44
	V. N. Cerveira	M_2	0.65	0.69	0.04	122.10	130.07	7.97
		S_2	0.26	0.26	0.00	173.51	174.61	1.10
		O_1	0.06	0.05	-0.01	359.30	66.30	-293.00
		K_1	0.04	0.05	0.01	107.15	104.61	-2.54
	Segadães	M_2	0.65	0.71	0.06	142.70	143.02	0.32
		S_2	0.26	0.27	0.01	195.26	190.98	-4.28
		O_1	0.06	0.05	-0.01	9.83	74.52	64.69
		K_1	0.04	0.05	0.01	118.03	113.10	-4.93
Lima	Viana do Castelo	M_2	1.00	1.06	0.05	76.76	75.57	-1.19
		S_2	0.50	0.49	-0.01	113.89	112.06	-1.83
		O_1	0.07	0.06	-0.01	319.95	40.15	-279.80
		K_1	0.06	0.06	0.00	73.58	77.00	3.42

4.3.2 Salinity and Water Temperature

A total of 21 locations in each estuary with salinity and water temperature data are available (section 4.1.5), however, only the data from the locations in the center of each transect will be used in this calibration. It was made an average of the three replicates measured in each location during the campaign, and with these values, was made the calibration of salinity and water temperature. However, this calibration only allows to identify a pattern and a seasonal evolution, leaving aside the tide temporal scale comparison.

As observed in Figure 4.6, the water temperature is well represented over all locations, with maximum differences between the model predictions and the data around 4°C. Regarding salinity (Figure 4.7), the pattern is the same between model predictions and observations, with small differences for most of the stations. In Minho estuary, the results are excellent but in Lima are found significant differences (around 10 ppt) in the last four months of the calibration period, mainly in the locations near the mouth of the estuary.

These differences can be explained with the fact that the salinity is a physical variable that undergoes large variations in a short period of time. In ten minutes, the value of this variable may change from 10 to 25 ppt. On the other hand, as has been said before, the salt and heat data were collected doing three replicates in the three locations of each transect once a month, which makes it difficult to calibrate the model.

However, looking at the model predictions, it is seen that the model reproduces satisfactorily the variations of salinity and water temperature in the center stations of each transect at both estuaries.

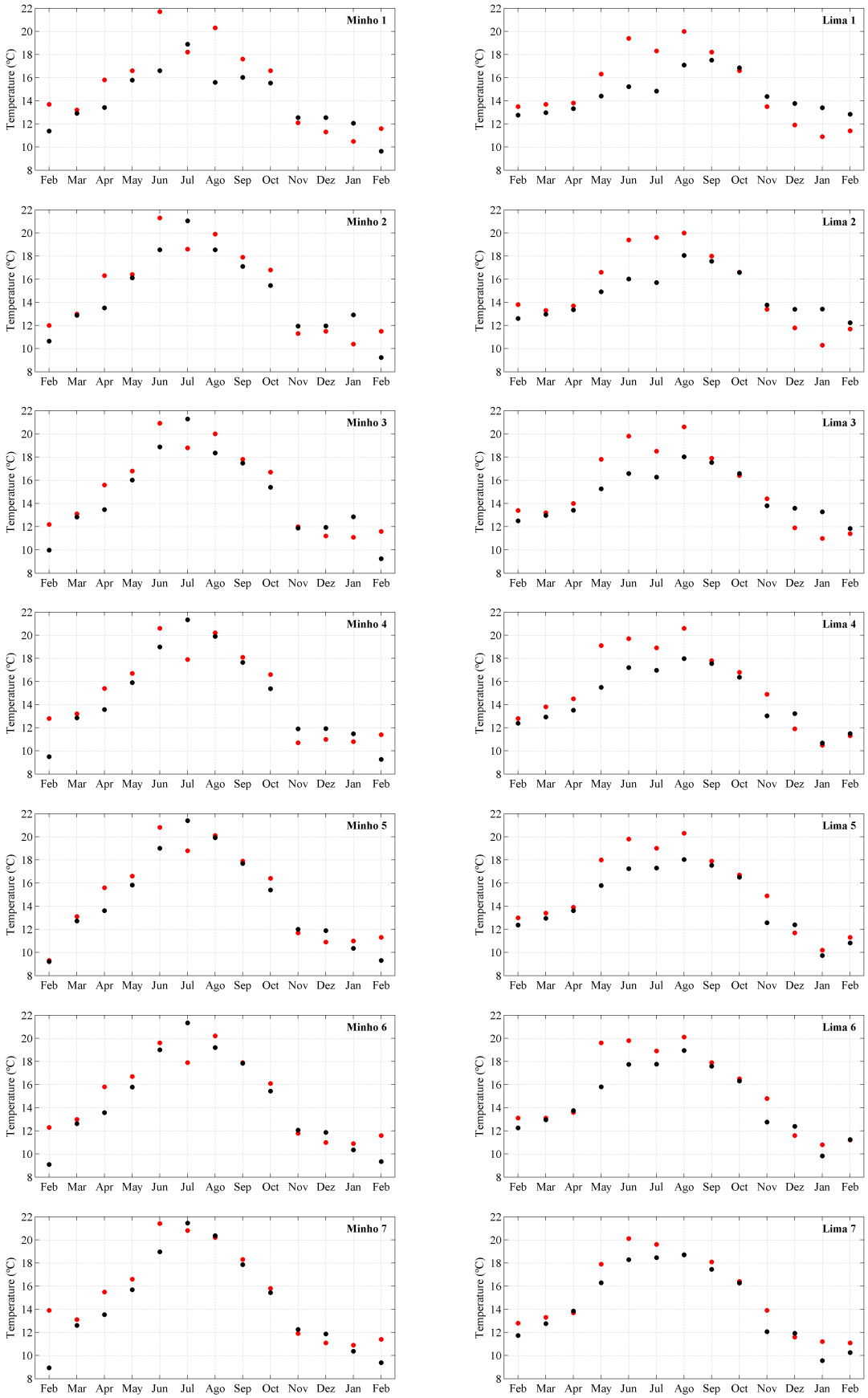

Figure 4.6: Comparison between predicted and observed water temperature. Black dots are the model predictions and red dots are the observations. The first row presents the center stations in transect 1, the second row in transect 2, and so on.

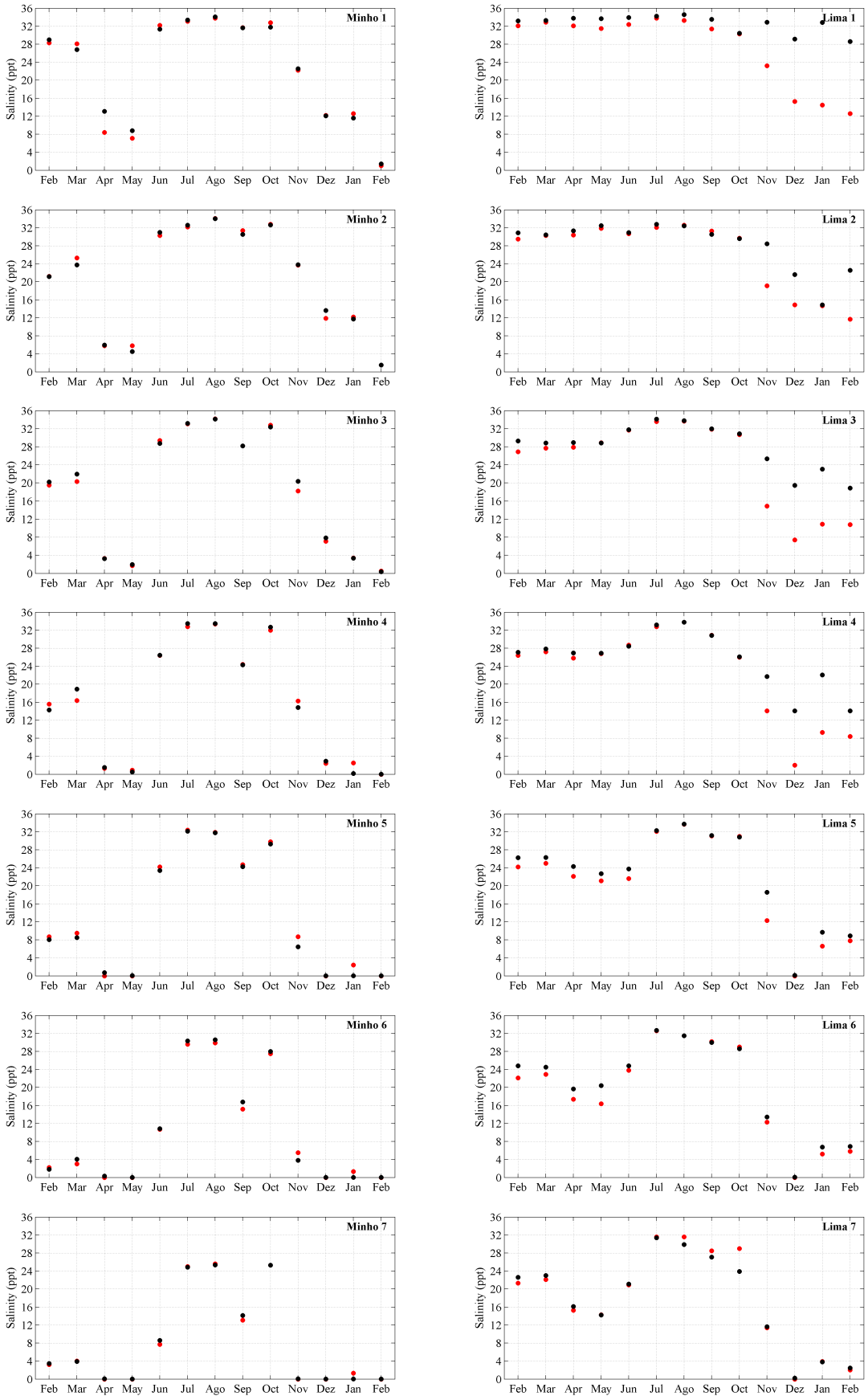

Figure 4.7: Comparison between predicted and observed salinity. Black dots are the model predictions and red dots are the observations. The first row presents the center stations in transect 1, the second row in transect 2, and so on.

Chapter 5

Climate Change Impact on Estuaries Hydrology

This Chapter presents the climate change scenarios description and the model predictions for each scenario. The model's predictions, on both estuaries, are presented in three sets: water temperature and salinity vertical sections; salt intrusions; and estuarine plumes. In each set it is made the analysis for summer and winter conditions in order to study the variations under these seasons.

5.1 Scenarios Description

This section presents the scenarios defined to study the hydrological response of the Minho and Lima estuaries to future climate changes. Based on the IPCC (Intergovernmental Panel on Climate Change) report of 2014 (Pachauri et al., 2014), the future scenarios used in this work were the RCP 4.5 and RCP 8.5, corresponding to the Representative Concentration Pathways mentioned in the report.

The Representative Concentration Pathways (RCPs) describe four different 21st century pathways of greenhouse gas emissions (GHG) and atmospheric concentrations, air pollutant emissions and land use. The RCPs have been developed using Integrated Assessment Models (IAMs) as input to a wide range of climate simulations to project their consequences for the climate system. These projections are used for impacts and adaptation assessment. The scenarios are used to assess the costs associated with emission reductions consistent with particular concentration pathways (Pachauri et al., 2014).

The RCPs represent the range of GHG emissions, including a mitigation scenario (RCP 2.6), two intermediate scenarios (RCP 4.5 and RCP 6.0), and one scenario with very high GHG emissions (RCP 8.5). The RCPs land use scenarios, show a wide range of possible futures, ranging from reforestation to deforestation. For air pollutants, the RCP scenarios assume a consistent decrease in emissions as a consequence of assumed air pollution control and GHG mitigation policy (Pachauri et al., 2014). This report considers the scenario RCP 4.5 the most likely and, consequently, more optimistic than the scenario RCP 8.5, which is presented as the more pessimistic. This was the base to choice the future scenarios that will be studied in this work.

The effect of climatic change in Minho and Lima estuaries was studied through three scenarios. The calibration run, for the year 2012, was defined as Present scenario (representative of the present). To define the RCP 4.5 and RCP 8.5 scenarios, were applied changes in the model's ocean, atmospheric and river boundaries.

The modifications that were applied in the climate change scenarios regarding to Present scenario, were the initial sea level, water temperature, ocean salinity, river discharge, heat flux, and wind process. In the model's heat flux, the climatic changes were made in air humidity, air temperature and solar radiation, and in the model's wind process, the modification was on the wind velocity. Table 5.1 presents the changes applied in the ocean and river model's boundary for the definition of the RCPs scenarios, and Table 5.2 presents the changes in the model's atmospheric boundary.

Each scenario was divided into two parts (summer and winter), giving a total of 6 simulations (2 for Present, 2 for RCP 4.5 and 2 for RCP 8.5). Summer future simulations ran from 1st May to 1st September of 2100, and winter future simulations between 1st November 2100 and 1st March 2101. The first month of simulation was used to warm up the model.

The IPCC report predicts a global sea level variation by the end of the century, for scenario RCP 4.5, between 0.32 and 0.63 m, and for scenario RCP 8.5, between 0.45 and 0.82 m. These values are based on 21 CMIP5 (Coupled Model Intercomparison Project 5) models and the changes are calculated with respect to the 1986–2005 period. In this work, the applied values were 0.32 m for RCP 4.5 and 0.82 m for RCP 8.5 presenting an optimistic and pessimistic view, respectively. This values were directly applied to the model implementation previously developed in calibration.

Concerning water temperature and salinity, the values were obtained averaging the predictions of four global models: CNRM-CM5, HadGEM2-ES, IPSL-CM5A-MR and MPI-ESM-LR. Each model data was withdrawn from the CMIP website, established by the Working Group on Coupled Modelling (WGCM) under the World Climate Research Programme (WCRP). For scenario RCP 4.5, the changes in water temperature and ocean salinity were +1.55 ºC and -0.65 ppt respectively. An increase of 3.20 ºC in water temperature and a decrease of 1.55 ppt in ocean salinity were the changes applied for scenario RCP 8.5.

Table 5.1: Changes in the inputs of ocean and river boundary, applied in the future scenarios.

	RCP 4.5	RCP 8.5
SLR (m)	+0.32	+0.82
Water Temperature (ºC)	+1.55	+3.20
Ocean Salinity (ppt)	-0.65	-1.55
River Discharge (%)	-5	-25

Table 5.2: Changes in the inputs of atmospheric boundary, applied in the future scenarios.

	Air Temperature (ºC)		Humidity (%)		Solar Radiation ($Jm^{-2}s^{-1}$)		Wind Velocity (ms^{-1})	
Month	RCP 4.5	RCP 8.5	RCP4.5	RCP 8.5	RCP 4.5	RCP 8.5	RCP 4.5	RCP 8.5
May	+2.50	+2.91	-1.35	-1.71	+23.37	+8.04	-0.25	-0.24
June	+1.18	+4.01	-1.03	-6.35	-2.81	+18.60	+0.16	+0.15
July	+1.93	+6.82	-2.37	-13.32	+6.73	+20.60	+0.08	+0.15
August	+2.62	+5.17	-1.77	-2.32	+3.66	+6.45	-0.01	-0.14
November	+2.32	+5.18	+4.00	-1.61	-13.53	+0.8	+0.42	+0.07
December	+1.74	+3.88	+0.49	+0.12	-1.88	-1.97	+0.23	+0.20
January	+2.23	+3.22	+2.53	-0.69	-7.39	-5.78	+1.05	+0.24
February	+0.96	+2.70	+1.08	+0.52	-4.12	-8.26	+0.09	-0.08

The Swedish Meteorological and Hydrological Institute (SMHI) has a website with hydrological predictions for the environment called hypeweb (www.hypeweb.smhi.se). Here, is possible to obtain the percentage change in river discharge for the climate change scenarios RCP 4.5 and RCP 8.5. This percentage is calculated, for RCP 4.5 through five global and five regional models with one hydrological model (E-HYPE2.5 model). For RCP 8.5, the global and regional models reduces to four maintaining the hydrological model. The reference period is 1970-1999. The applied changes, in the discharges of both rivers, were -5% for RCP 4.5 and -25% for RCP 8.5.

Finally, the applied changes in the heat flux and wind processes were based on Portal do Clima website (www.portaldoclima.pt). This website was created due to a project resulting from the activities of the AdaPT (Adaptar Portugal às Alterações Climáticas) program. This program was conceived to financially support the activities related to climate change adaptations in Portugal guided by the terms set out in the Memorandum of Understanding between Portugal, Norway, Iceland and Liechtenstein under the European Economic Area Financial Mechanism (EEA-Grants).

From the website, the variables withdrawn were the relative humidity, the air temperature and the solar radiation for the model's heat flux. For the wind process, it was withdrawn the wind speed. These variables are calculated over four global models (CNRM-CERFACS-CNRM-CM5, ICHEC-EC-EARTH, IPSL-IPSL-CM5A-MR and MPI-M-MPI-ESM-LR) and over five regional models (CLMcom-CCLM4-8-17, DHI-HIRHAM5, IPSL-INERIS-WRF331F, KNMI-RACMO22E and SMHI-RCA4). The extracted data was a monthly average anomaly calculated over all models, comparing with the reference period 1971-2000.

Vertical sections, salt intrusions and estuarine plumes were studied throw summer and winter conditions for both estuaries. Figures presenting the model's predictions are from 29th of July for summer and from 19th of December for winter conditions. The next sections in this chapter presents the comparison between Present, RCP 4.5 and RCP 8.5 scenarios, as well as the corresponding differences between them.

5.2 Vertical Sections

An advantage of using three-dimensional models is the ability to analyse from model simulations how the water column varies from the surface to the bottom. The water temperature and salinity, current velocity, density, among others vertical profiles can be analysed from these model predictions.

This section shows the vertical sections of salinity and water temperature, for the three scenarios, during summer and winter conditions. For each situation are shown the transect 1, 2, 3, 5 and 6 in both estuaries (Figure 2.1), allowing an analysis along the estuary, with an M representing Minho and an L representing Lima.

5.2.1 Minho Estuary

Summer Conditions

Figures 5.1 and 5.2 show, respectively, the comparison of water temperature and salinity averaged over the tidal cycle between Present and RCP 4.5 scenarios, during summer conditions.

In the first column of Figure 5.1 is presented the vertical sections of water temperature for Present scenario. The model predictions show an increasing longitudinal gradient of water temperature, rising from 17 ºC in M1 to 22 ºC in M6. This is an expected behaviour due to the water temperature established on the oceanic and fluvial boundary. In ocean boundary, the applied water temperature (18 ºC) is lower than in river boundary (20 ºC).

A lateral structure or gradient in M2, M3 and M5 sections is also observed. In the Southern margin of the estuary (left side of the each image), are found higher water temperatures than in the Northern margin. This possibly means that the ebb occurs preferentially by the Portuguese margin (South margin), and the flood by the Spanish margin (North margin). This first column also shows a vertical structure from M1 to M6. However, this stratification is slight (with differences of 1 ºC from the surface to the bottom).

Regarding salinity, the first column of Figure 5.2 shows that exists a typical longitudinal estuarine gradient with higher salinity values downstream (M1 section), and lower salinity values upstream (M6 section). This gradient it is expectable due to the open boundaries implementation (salt water at the ocean boundary and fresh water at the river boundary).

The lateral structure, visualized in M2, M3 and M5 sections, is in agreement with the water temperature lateral structure mentioned before. It is seen that the less saline water flows through the Portuguese margin and the salt water through the Spanish margin. As in Figure 5.1, it is visualized a slight vertical structure in M1 and M6.

For RCP 4.5 scenario, in the water temperature sections (second column in Figure 5.1), it is found a similar pattern compared with Present scenario, but with higher values, due to the implemented climate changes presented in section 5.1. The longitudinal gradient is similar to the Present scenario (water temperature increases from M1 to M6). The model predictions continue to show the existence of a lateral structure, with fresh water flowing through the Portuguese margin.

It is found an intensification of the water temperature vertical structure, mainly in the M2 and M3 sections, when compared with Present scenario. It is important to note that the modification in the stratification presented in M1 indicates a possible increase in the ebb current, due to the inclination of the isolines. Here, the model predicts an increase of 3 ºC in the South margin of the estuary.

The salinity changes predicted by the model for RCP 4.5 scenario are presented in the second column of Figure 5.2, showing the same longitudinal gradient presented for water temperature, but with higher salinity values. The lateral and vertical structure mentioned previously persists but, in the vertical stratification, the model predicts a slight increase on the South margin of M3 and M5 sections.

The third column of Figure 5.1 and 5.2 presents the differences between Present and RCP 4.5 scenarios of water temperature and salinity, respectively. The higher differences for water temperature are predicted for M5 and M6 sections, and the higher differences for salinity are predicted for M2 and M3 sections. In M5 and M6 sections, the model predicts a water temperature increase of 3 ºC in the shallow zones (north part of the sections) due to the higher solar radiation predicted for the future. The lower increases are predicted for the bottom.

For RCP 8.5 scenario, the water temperature sections (second column of Figure 5.3), resemble with Present scenario sections but with higher values due to climate change modifications. It is found lower water temperature (20 ºC) at the mouth and higher water temperature (25 ºC) at M6 section. As in Figure 5.1, model predicts an increase of water temperature (about 4 ºC) at the Portuguese margin in M1 section, and at the Spanish margin (shallow zone) in M5 and M6 sections. The predicted salinity for RCP 8.5 scenario is presented in Figure 5.4. Comparing with Present scenario, the salinity increases is higher (5.5 ppt) in the South margin of M3 and M5 sections. The lower differences occur in M1 section.

Finally, the comparison between RCP 4.5 and RCP 8.5 scenarios is presented in Figures 5.5 and 5.6. The first figure shows the water temperature differences, where it is predicted that the smaller differences between future scenarios will occur at the surface, and the higher differences at the bottom. It is also found that in M1 section the global differences are larger that in M6 section.

Considering this justification, can be also explained the differences occurring in salinity (Figure 5.6). In this figure, the differences presented in the third column show that the upstream sections (M5 and M6) will suffer an increase of 8.5 ppt at the surface, while the downstream sections (M1 and M2) will be only increased by 1 ppt. The higher values in M5 and M6 sections are explained by the decrease of 20% in the river discharge and by the sea level rise of 0.5 m between scenarios. This changes promote an increment of salinity, especially in the inner sections.

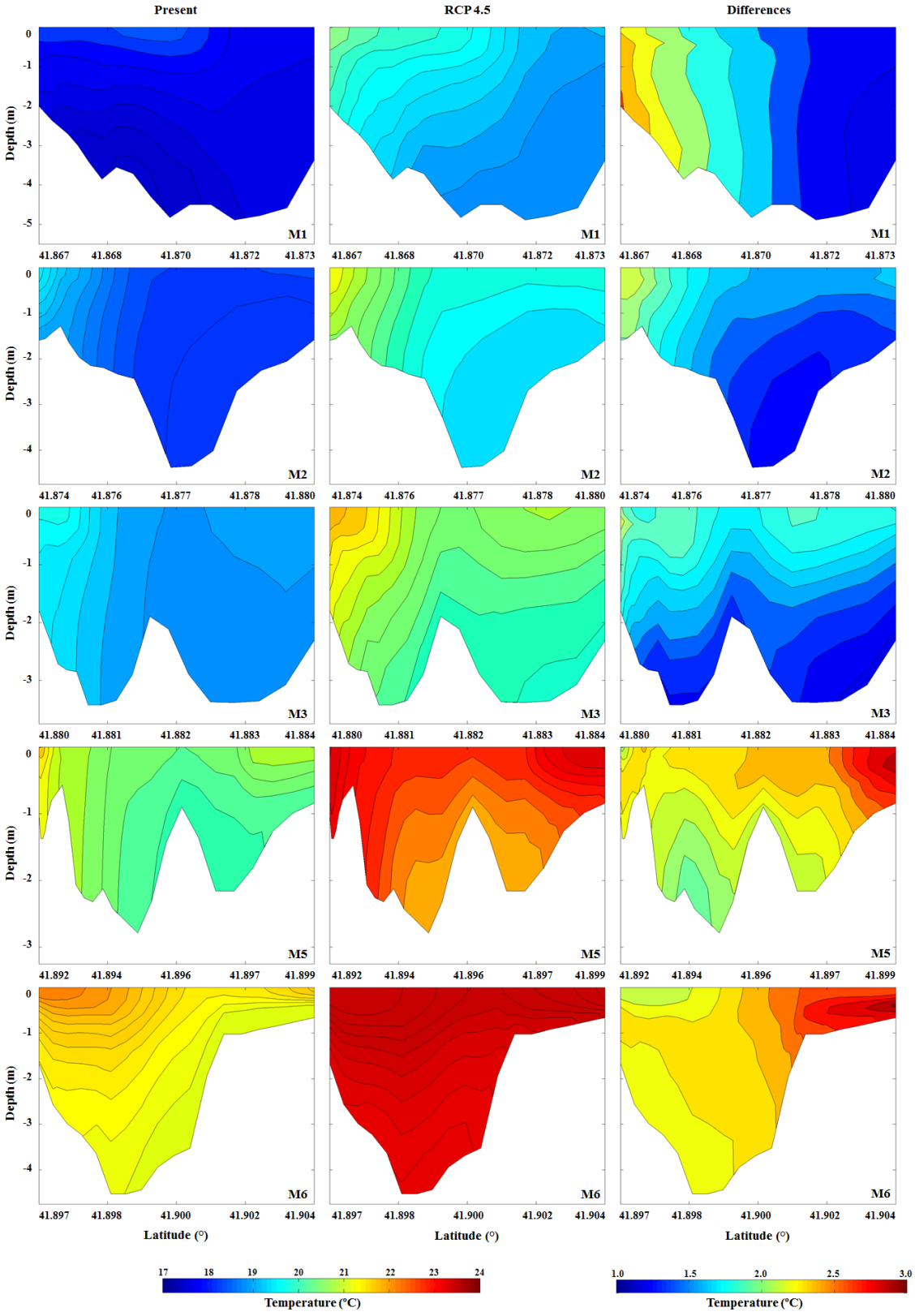

Figure 5.1: Vertical sections of water temperature averaged over the tidal cycle during summer conditions. From left to right columns: Present; RCP 4.5; differences between RCP 4.5 and Present. From top to bottom rows: transition from estuary mouth to estuary head.

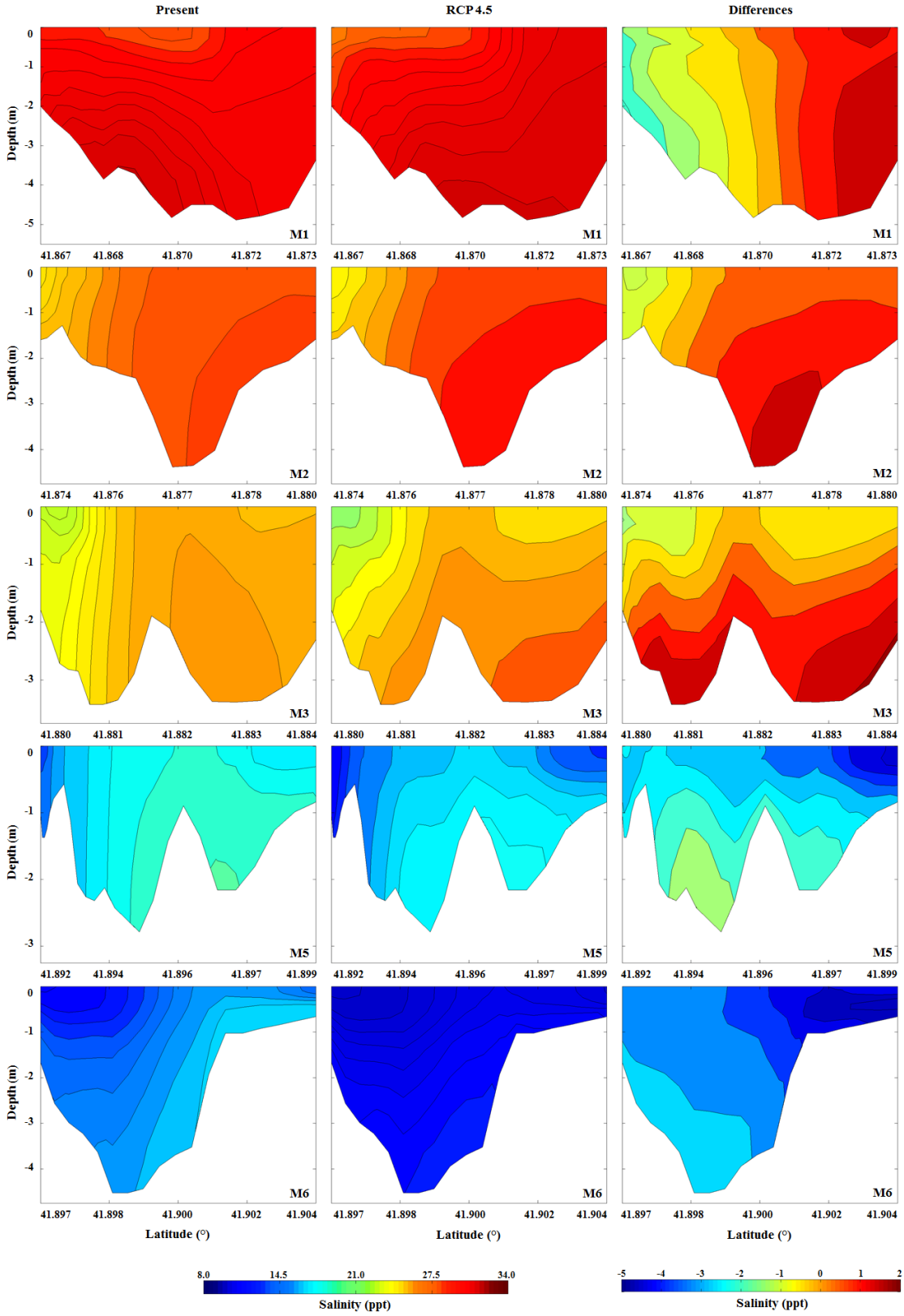

Figure 5.2: Vertical sections of salinity averaged over the tidal cycle during summer conditions. From left to right columns: Present; RCP 4.5; differences between RCP 4.5 and Present. From top to bottom rows: transition from estuary mouth to estuary head.

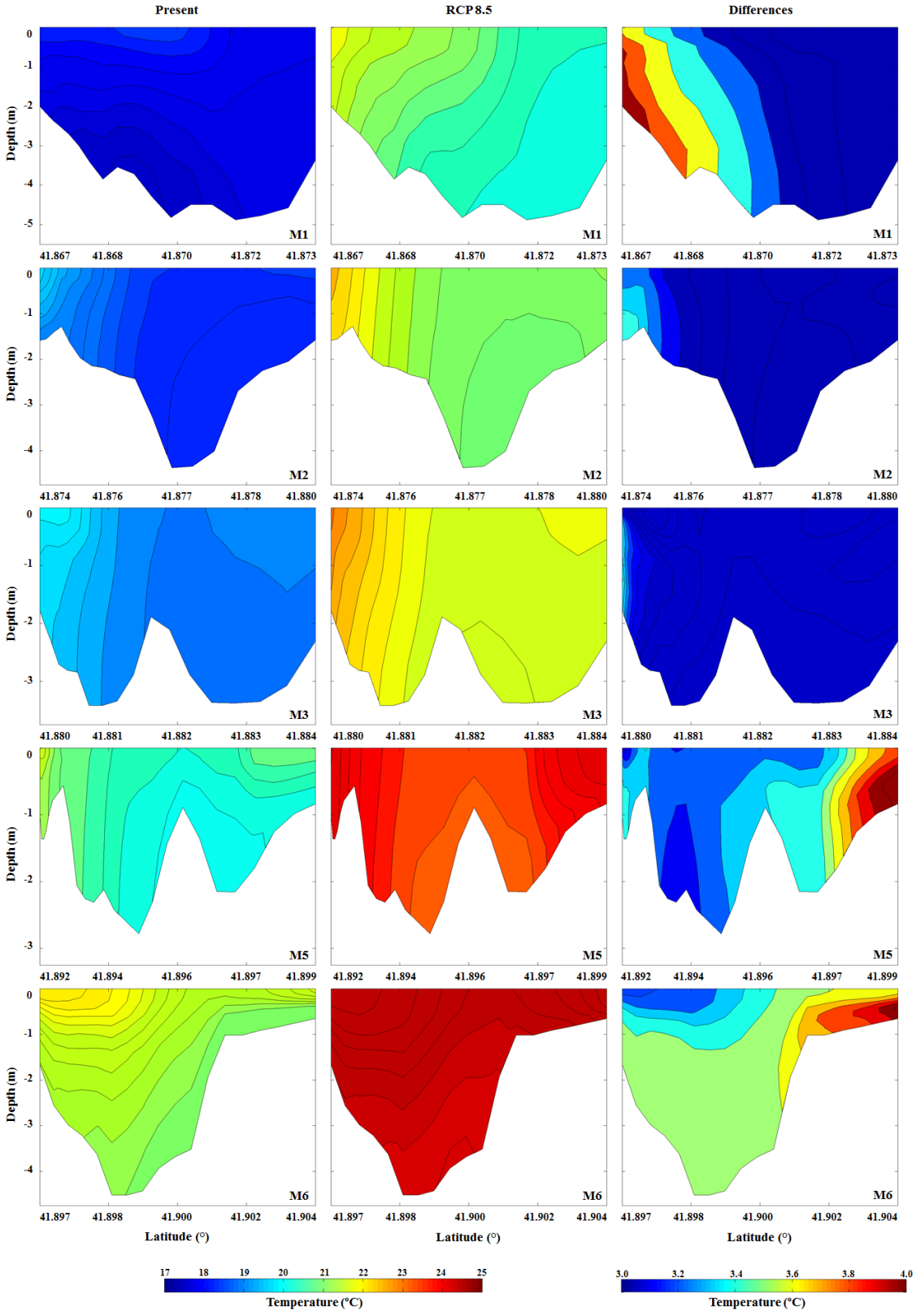

Figure 5.3: Vertical sections of water temperature averaged over the tidal cycle during summer conditions. From left to right columns: Present; RCP 8.5; differences between RCP 8.5 and Present. From top to bottom rows: transition from estuary mouth to estuary head.

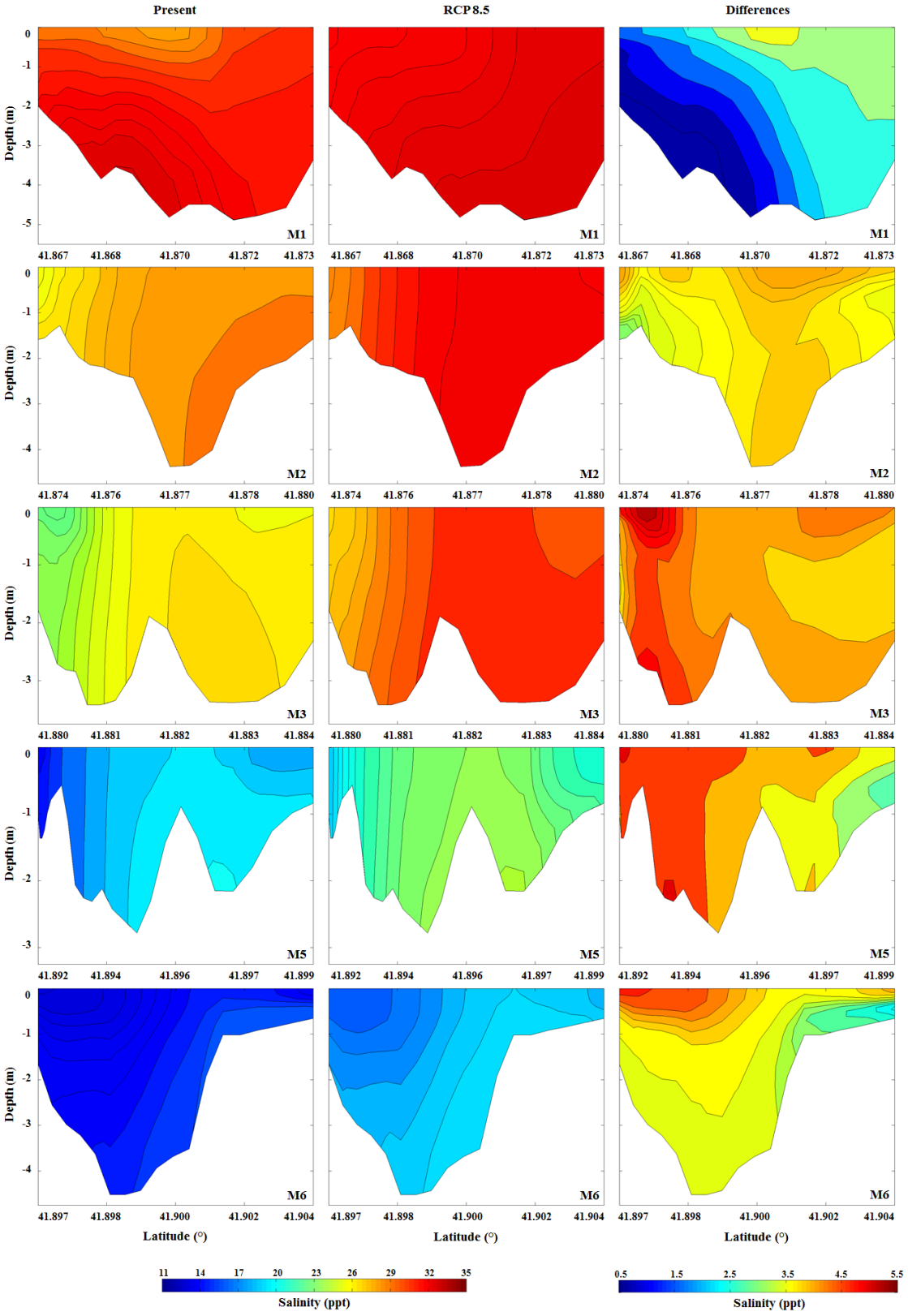

Figure 5.4: Vertical sections of salinity averaged over the tidal cycle during summer conditions. From left to right columns: Present; RCP 8.5; differences between RCP 8.5 and Present. From top to bottom rows: transition from estuary mouth to estuary head.

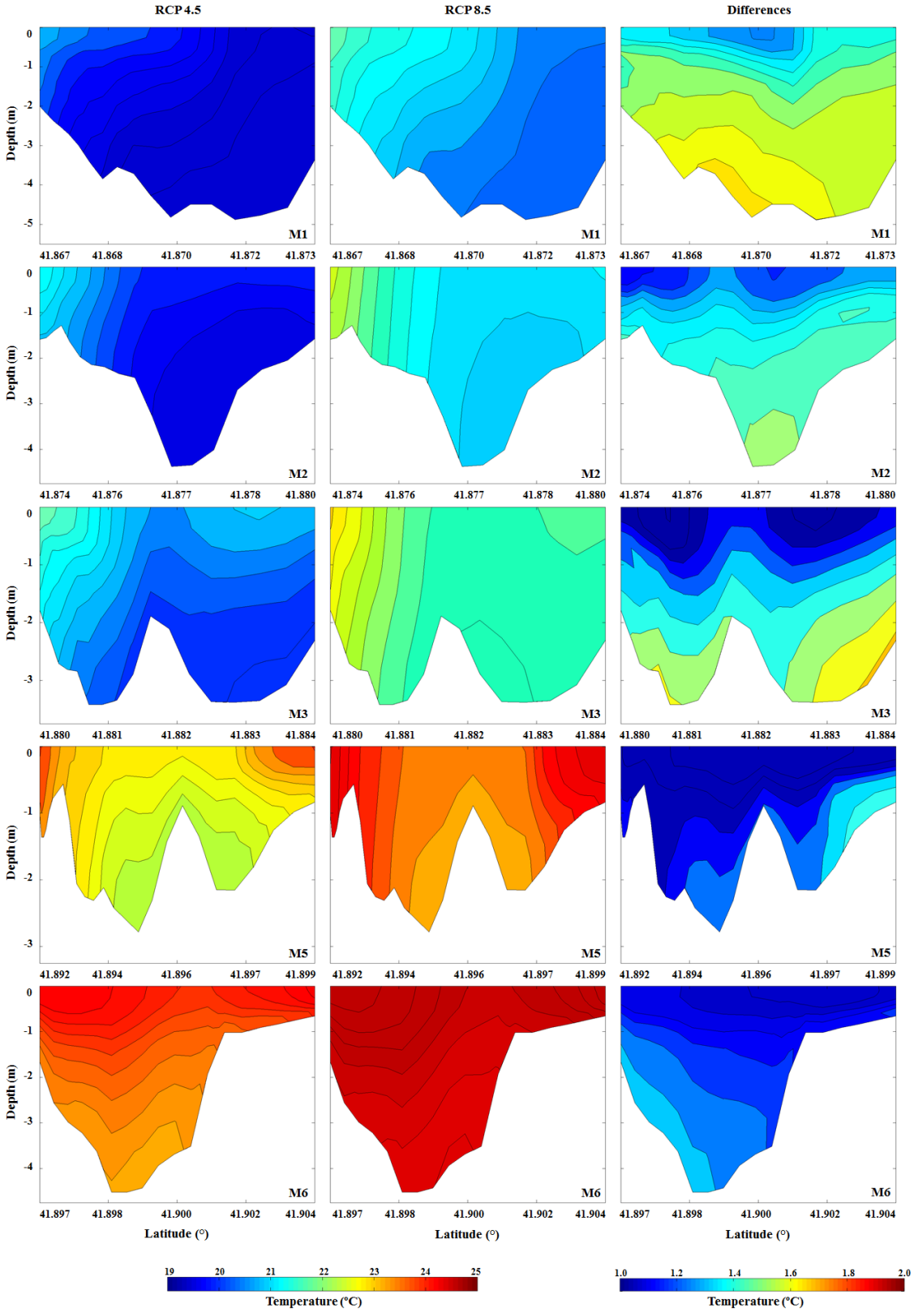

Figure 5.5: Vertical sections of water temperature averaged over the tidal cycle during summer conditions. From left to right columns: RCP 4.5; RCP 8.5; differences between RCP 8.5 and RCP 4.5. From top to bottom rows: transition from estuary mouth to estuary head.

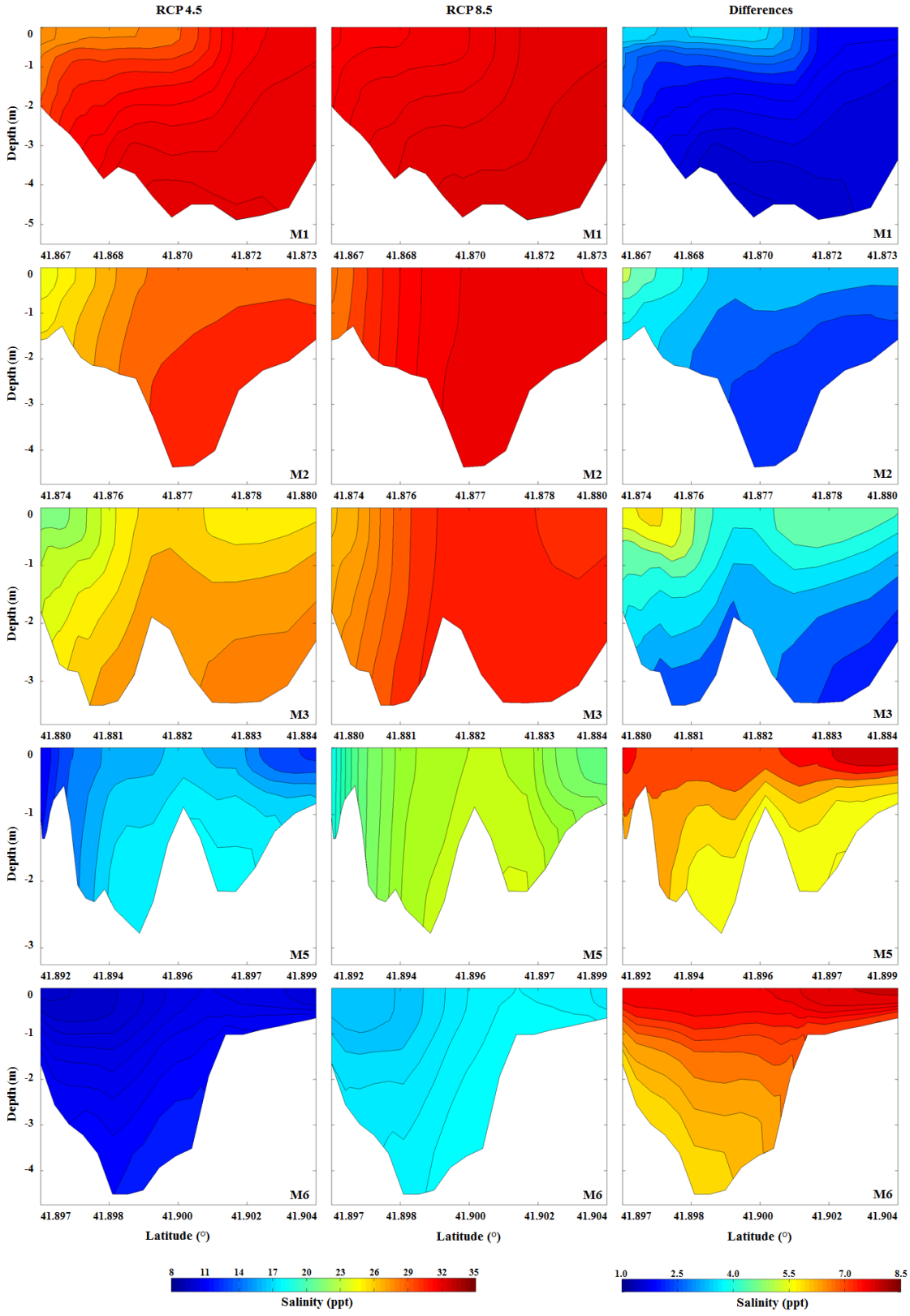

Figure 5.6: Vertical sections of salinity averaged over the tidal cycle during summer conditions. From left to right columns: RCP 4.5; RCP 8.5; differences between RCP 8.5 and RCP 4.5. From top to bottom rows: transition from estuary mouth to estuary head.

Winter Conditions

The estuary behaviour under winter conditions was also addressed in this work. It is important to study how the estuary respond to this type of conditions, that sometimes become quite extreme. In winter, the river discharge is higher but the water temperature is lower, and the air temperature and solar radiation are lower when compared with summer conditions.

Figure 5.7 shows the vertical sections of water temperature for Present and RCP 4.5 scenarios. The analysis of this, indicates that there is a different longitudinal gradient during winter comparing with summer. Whereas in summer the longitudinal gradient is positive from M1 to M6, during winter the gradient is negative from M1 to M6.

The minimum and maximum water temperature values decreases during winter conditions. The minimum value for Present scenario is 12.5 ºC, and the maximum is 15.5 ºC. This decrease is a combination of the changes mentioned above. The lateral gradient is less evident than in summer conditions, but it is still observed in M1, M2 and M3 sections in the Portuguese margin (North margin). The vertical stratification, in winter conditions, is less significant than in summer. For example, in M6 section, the model predicts a variation in the water column of 0.5 ºC from the surface to the bottom. The increase of fluvial discharge makes the water column more homogeneous.

For salinity (Figure 5.8), the model predicts a longitudinal variation from M1 to M6 sections of 26 to 2 ppt, maintaining the typically estuarine profile. Comparing with summer conditions, it is immediately observed that the increased river discharge during winter will have a strong impact on the saline structure of this estuary. The model predictions indicate a slight stratification in the North margin of M2, M3 and M5 sections, comparing with summer conditions. The large volume of fresh water coming from the river starts to slightly stratify the salt water zones, which were previously more saline and homogeneous. In M6 section, due to river discharge, the water column becomes completely homogeneous.

For RCP 4.5 scenario, in the water temperature sections (second column in Figure 5.7), as in summer, is observed a similar pattern compared with Present scenario but with higher values. This is due to the saline intrusion (increased by the sea level rise) and to the decrease of river discharge. The longitudinal gradient is similar to the Present scenario (water temperature decreases from M1 to M6). The model predictions continue to show the existence of a lateral structure, with fresh water flowing through Portuguese margin. It is found an intensification of the water temperature vertical structure, mainly in the M2 and M5 sections, comparing with Present scenario.

The salinity changes predicted by the model for RCP 4.5 scenario are presented in the second column of Figure 5.8, showing a longitudinal gradient similar to the water temperature figure, but with higher salinity values. The lateral and vertical structure mentioned previously are also found but, in vertical the model predicts a slight increase of salinity on the South margin of M3 and M5 sections.

The third column of Figure 5.7 and 5.8 presents the differences between Present and RCP 4.5 scenarios, for water temperature and salinity, respectively. From these figures is found that the higher differences for water temperature are predicted for M1 and M2 sections, and the higher differences for salinity are predicted for M3 and M5 sections. In M1 and M6 sections the model predicts a water temperature increase of 1.2 ºC and 0.4 ºC, respectively.

Comparing with summer conditions, it becomes more evident that the river discharge and the sea level rise are very important to longitudinal, lateral and vertical estuary structure establishment. In M5 section, the salinity increase of 3 ppt is an evidence of a higher saline intrusion.

For RCP 8.5 scenario, the water temperature sections (second column of Figure 5.9), resemble with Present scenario sections, but with higher values due to climate change modifications. It is observed the higher water temperature (17 ºC) at the mouth and lower water temperature (14 ºC) at M6 section. From this figure, is found that the model predicts an increase of water temperature (about 3 ºC) at the mouth, and 1.5 ºC at the head. The predicted salinities for RCP 8.5 scenario are presented in Figure 5.10. Comparing with Present scenario, the salinity increases with more intensity (9 ppt) in the North margin of M5 section. The lower differences occur in M1 section (4 ppt).

Finally, the comparison between RCP 4.5 and RCP 8.5 scenarios are presented in Figures 5.11 and 5.12. The first figure shows the water temperature, where are found smaller differences between future scenarios at M6 section while the higher differences occur at M1 and M2 sections. The reason for this is the increase of sea level and the decrease of river discharge between scenarios. This can be also explained by the differences occurring in salinity (Figure 5.12).

In this figure, the differences presented in the third column show that M5 section will suffer an increase of 7.5 ppt, while the downstream sections (M1, M2 and M3) will be increased by 4.5 ppt. It is also found that in M5 section, the North margin will become more saline and, consequently, less stratified. The raise of salinity through the estuary is explained, as in Figure 5.6, by the decrease of 20% in the river discharge and by the sea level rise of 0.5 m between scenarios. This changes promote an increment of salinity in all estuary.

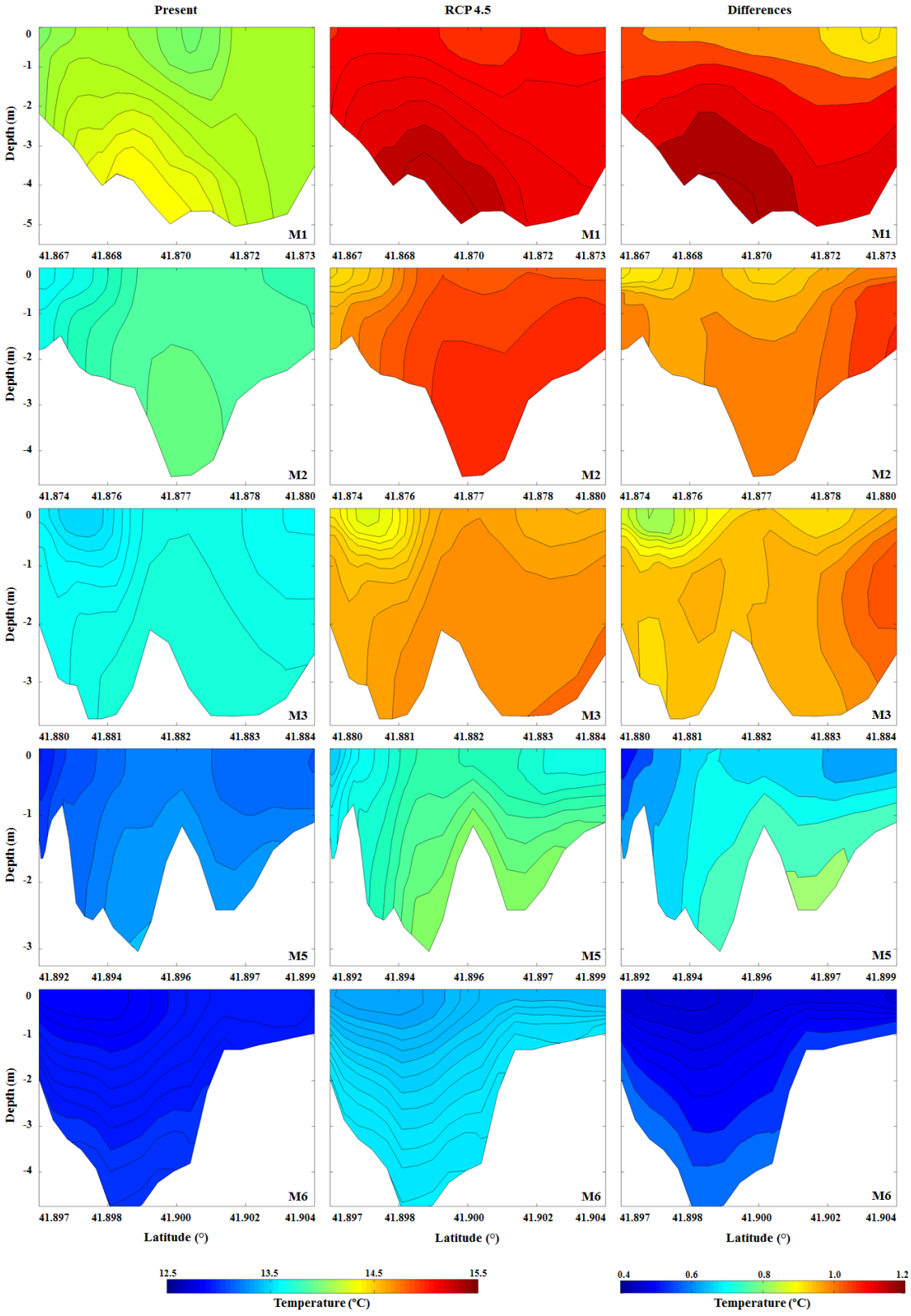

Figure 5.7: Vertical sections of water temperature averaged over the tidal cycle during winter conditions. From left to right columns: Present; RCP 4.5; differences between RCP 4.5 and Present. From top to bottom rows: transition from estuary mouth to estuary head.

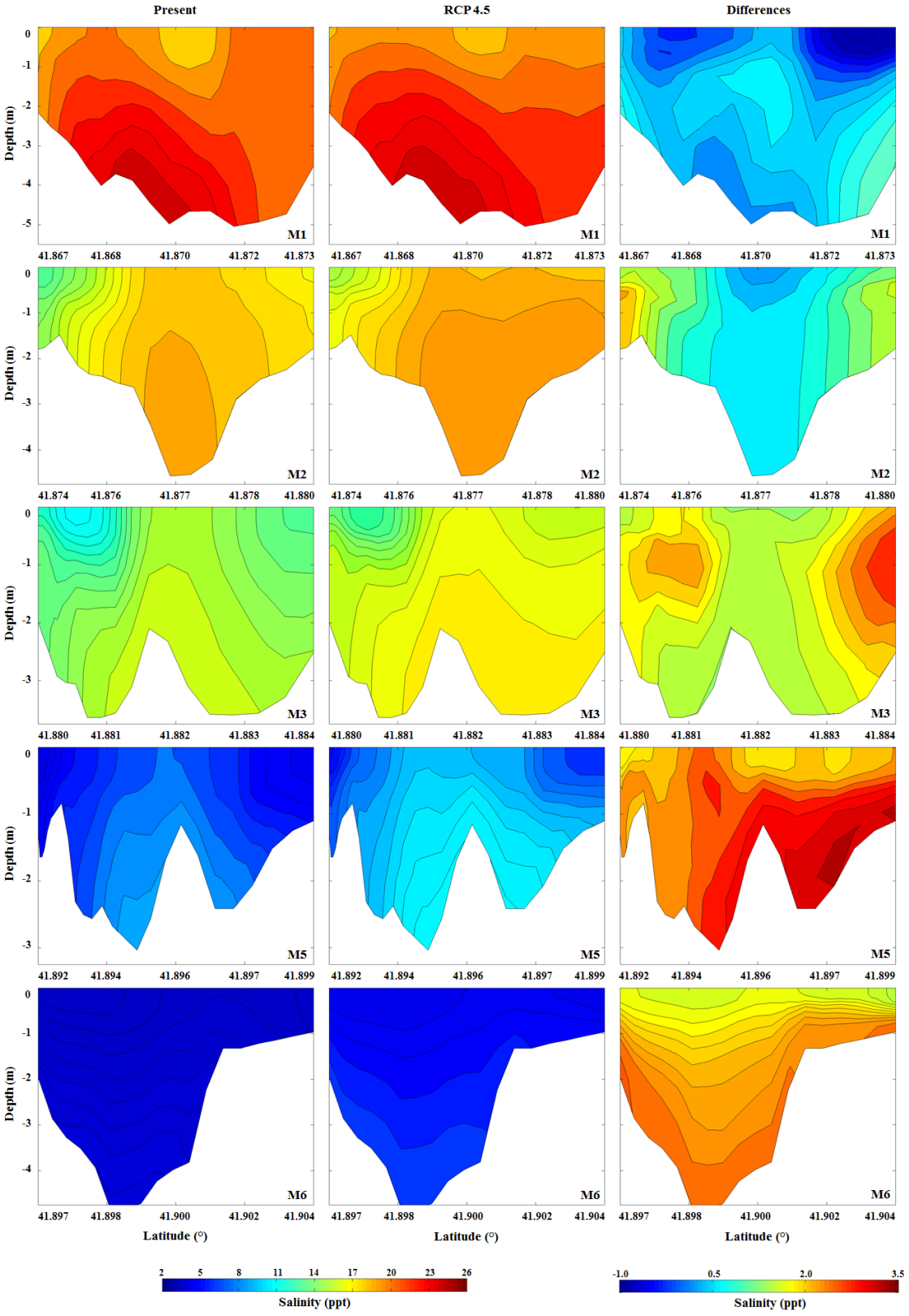

Figure 5.8: Vertical sections of salinity averaged over the tidal cycle during winter conditions. From left to right columns: Present; RCP 4.5; differences between RCP 4.5 and Present. From top to bottom rows: transition from estuary mouth to estuary head.

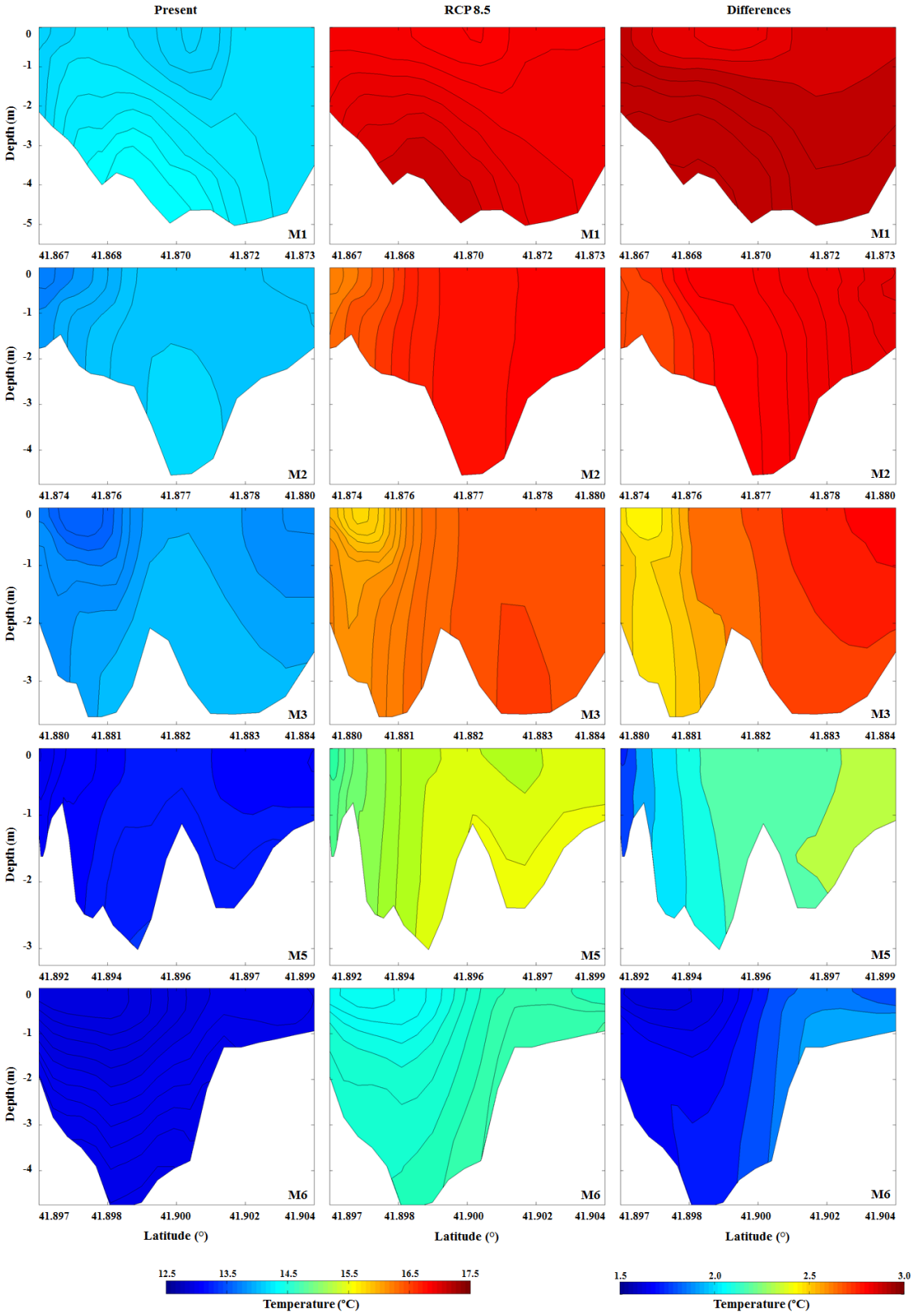

Figure 5.9: Vertical sections of water temperature averaged over the tidal cycle during winter conditions. From left to right columns: Present; RCP 8.5; differences between RCP 8.5 and Present. From top to bottom rows: transition from estuary mouth to estuary head.

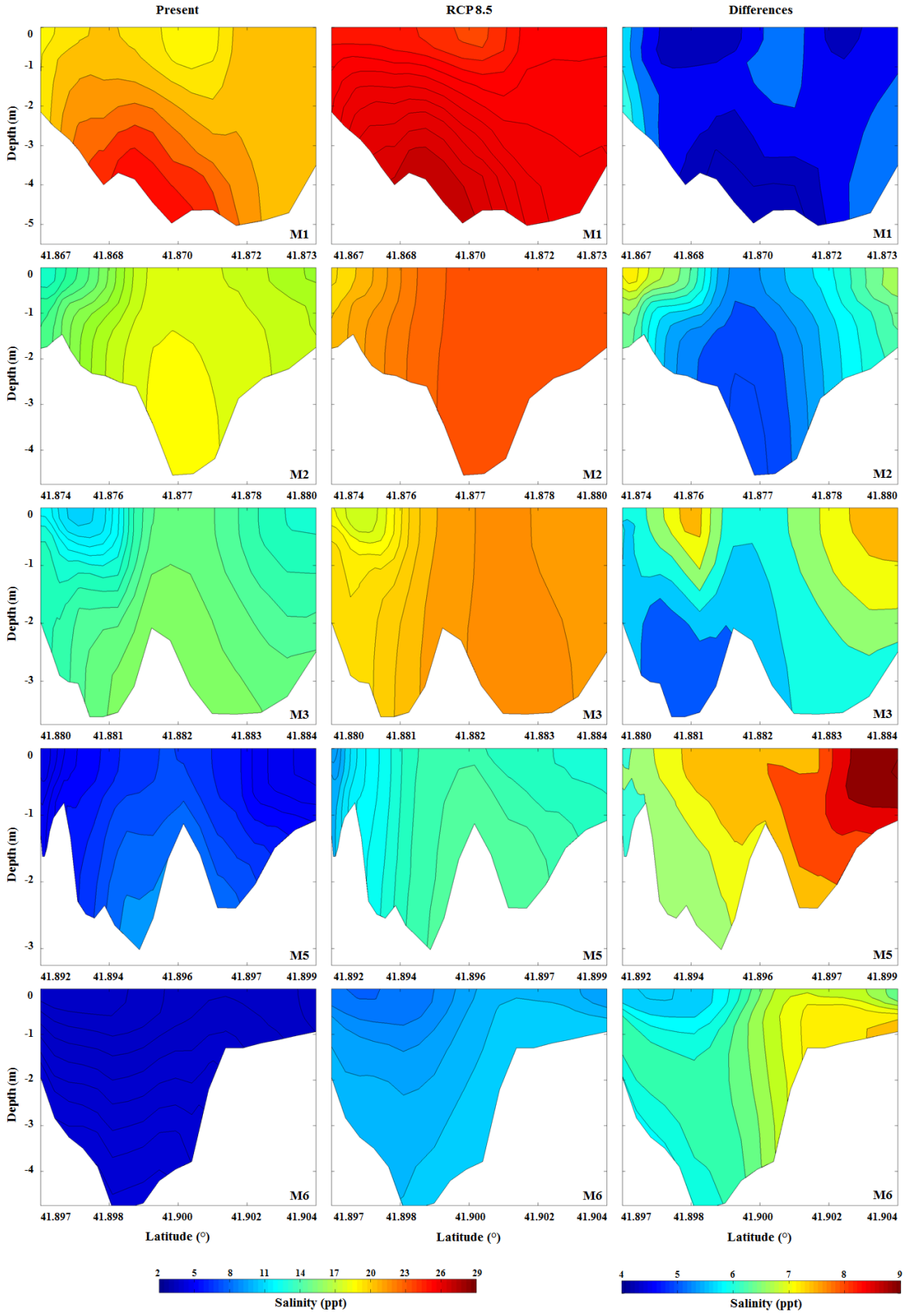

Figure 5.10: Vertical sections of salinity averaged over the tidal cycle during winter conditions. From left to right columns: Present; RCP 8.5; differences between RCP 8.5 and Present. From top to bottom rows: transition from estuary mouth to estuary head.

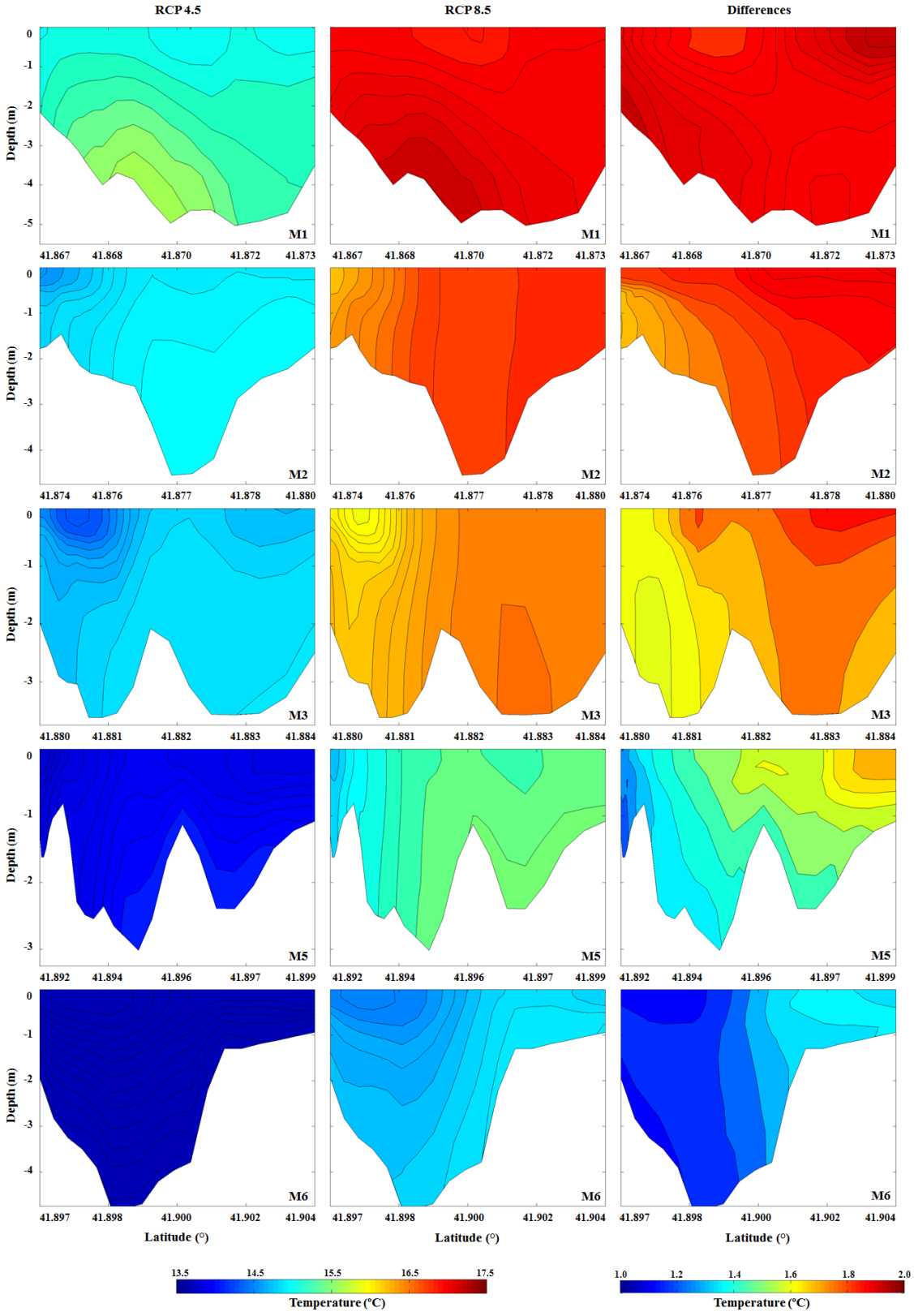

Figure 5.11: Vertical sections of water temperature averaged over the tidal cycle during winter conditions. From left to right columns: RCP 4.5; RCP 8.5; differences between RCP 8.5 and RCP 4.5. From top to bottom rows: transition from estuary mouth to estuary head.

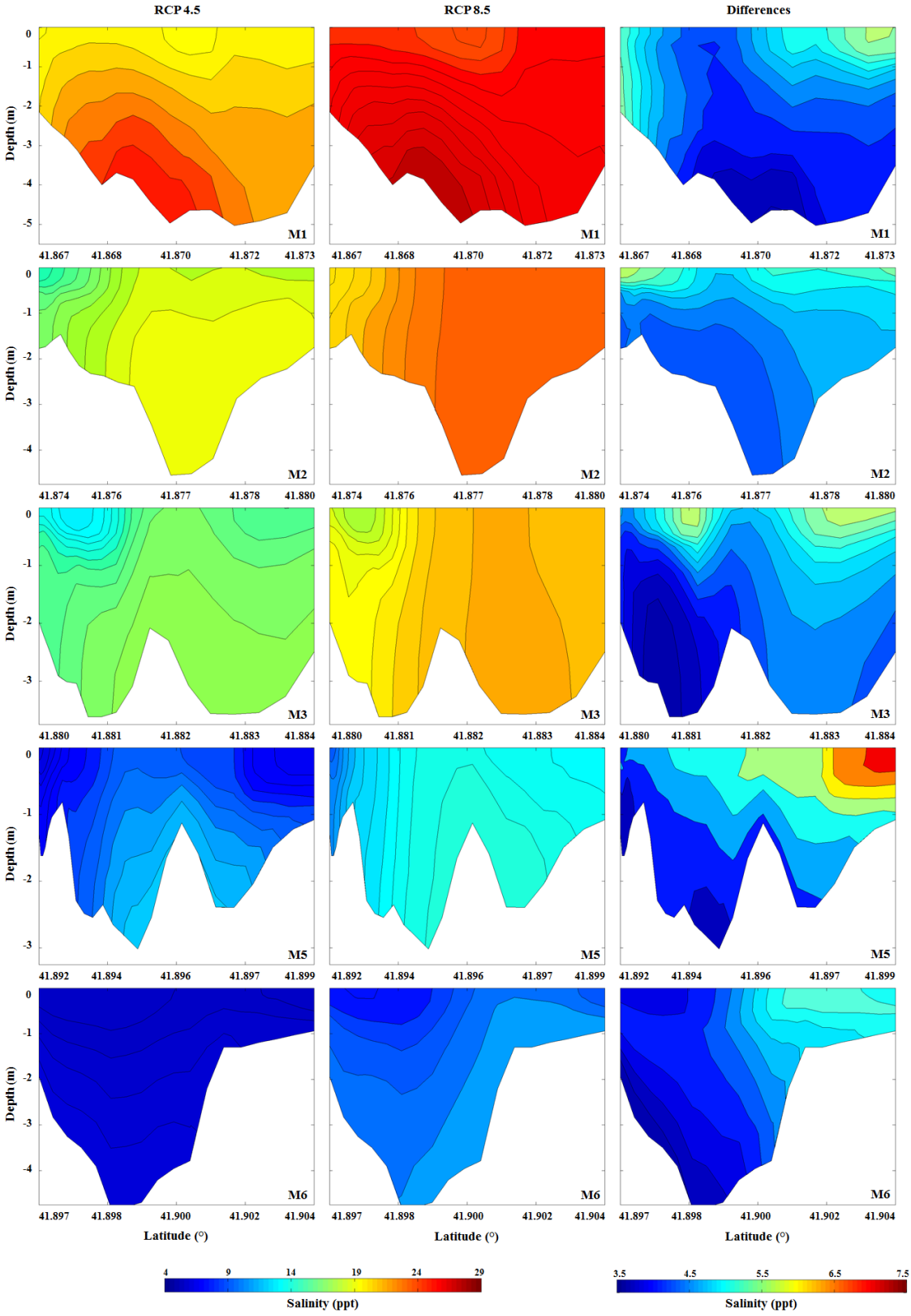

Figure 5.12: Vertical sections of salinity averaged over the tidal cycle during winter conditions. From left to right columns: RCP 4.5; RCP 8.5; differences between RCP 8.5 and RCP 4.5. From top to bottom rows: transition from estuary mouth to estuary head.

5.2.2 Lima Estuary

Summer Conditions

In this section are presented the Lima river sections for the summer and winter conditions previously exposed in section 5.2.1. Figures 5.13 and 5.14 show, respectively, the comparison of the water temperature and salinity averaged over the tidal cycle, between Present and RCP 4.5 scenarios, during summer conditions.

The vertical sections of water temperature for Present scenario presented in the first column of Figure 5.13 show immediately deeper depth for this estuary along the first three sections than for the Minho estuary. The model predictions show an increasing longitudinal gradient of water temperature, rising from 16 ºC in L1 to 20 ºC in L6. As in Minho, this is an expected pattern due to the water temperature established on the oceanic and fluvial boundaries. A lateral homogeneity is found through all sections.

Vertically, this first column shows a vertical gradient in all sections. This stratification, with water temperature differences of 2 ºC from the surface to the bottom, is more evident in L2 and L3 sections. In L2, L3, L5 and L6 sections, is observed a surface layer (about 1 m depth) with higher water temperature than the remaining water column. This is explained by the lower river discharge (section 4.1.4) flowing on the surface of the water column.

Regarding salinity, the first column of Figure 5.14 shows a typical longitudinal estuarine gradient with higher salinity values downstream (L1 section), and lower salinity values upstream (L6 section). This is an expectable variation due to the open boundaries implementation (salt water at the ocean boundary and fresh water at the river boundary). The lateral homogeneity is also visualized in this figure. As in Figure 5.13, a vertical structure from L1 to L6 is observed as well as a superficial layer with lower salinity.

For RCP 4.5 scenario, the water temperature sections (second column in Figure 5.13) revealed a similar pattern comparing with Present scenario, but with higher values, due to the implemented climate change presented in section 5.1. The changes in ocean water temperature (+1.55 ºC) and sea level rise (+0.32 m), induce the increase of water temperature in the estuary. The longitudinal gradient is similar to the Present scenario, with water temperature increasing from L1 to L6. The sea level rise induces this raise, providing more ocean water into the estuary. The model predictions continues to show an homogeneous lateral structure. It is found a similar water temperature vertical structure, but with expected higher values, comparing with Present scenario.

The predicted salinity changes for RCP 4.5 scenario, presented in the second column of Figure 5.14, show longitudinal, lateral and vertical gradients similar to those found for water temperature, but with higher values in the first meter depth and lower values beneath this layer. The explanation for this is the increased sea level and the decreased ocean salinity and river discharge. Being more saline than river water, the ocean water flows into the estuary near the bottom, reason why exists a slight decrease of salinity beneath the surface layer. The increased salinity in the surface layer results from the lower river discharge.

The third column of Figures 5.13 and 5.14, presents the differences between Present and RCP 4.5 scenarios for water temperature and salinity, respectively. These images show that the higher differences for water temperature are predicted below the superficial layer (with maximum value of 1.8 ºC), and the higher differences for salinity are predicted for the superficial layer in L5 and L6 sections.

For RCP 8.5 scenario, the water temperature sections (second column of Figure 5.15), are similar with Present scenario, but with higher values due to climate change modifications. It is found an increase between 3 and 3.5 ºC for all sections, with higher intensification below the superficial layer. Once again, this occur due to sea level rise (+0.82 m) and ocean water temperature increase (+3.20 ºC).

The predicted salinities for RCP 8.5 scenario are presented in Figure 5.16. Comparing with Present scenario, the salinity increases (2.5 ppt) in the surface of L5 and L6 sections and decreases in L1, L2 and L3 sections. The decrease in ocean salinity (-1.55 ppt) explains the predictions founded in L1, L2 and L3 sections. The sea level rise, combined with lower river discharge and more intense solar radiation, lead to the vertical pattern founded in L5 and L6 sections.

At last, the comparison between RCP 4.5 and RCP 8.5 scenarios is presented in Figures 5.17 and 5.18. The first figure shows the water temperature, where is found that the differences are very small (ranging between 1.70 and 1.90 ºC), being more perceptible in the zone immediately below the layer previously mentioned. In Figure 5.18, the differences presented in the third column shows that the upstream sections (L5 and L6) will suffer an increase of 1.2 ppt at the surface, while the downstream sections (L1, L2 and L3) will become less saline.

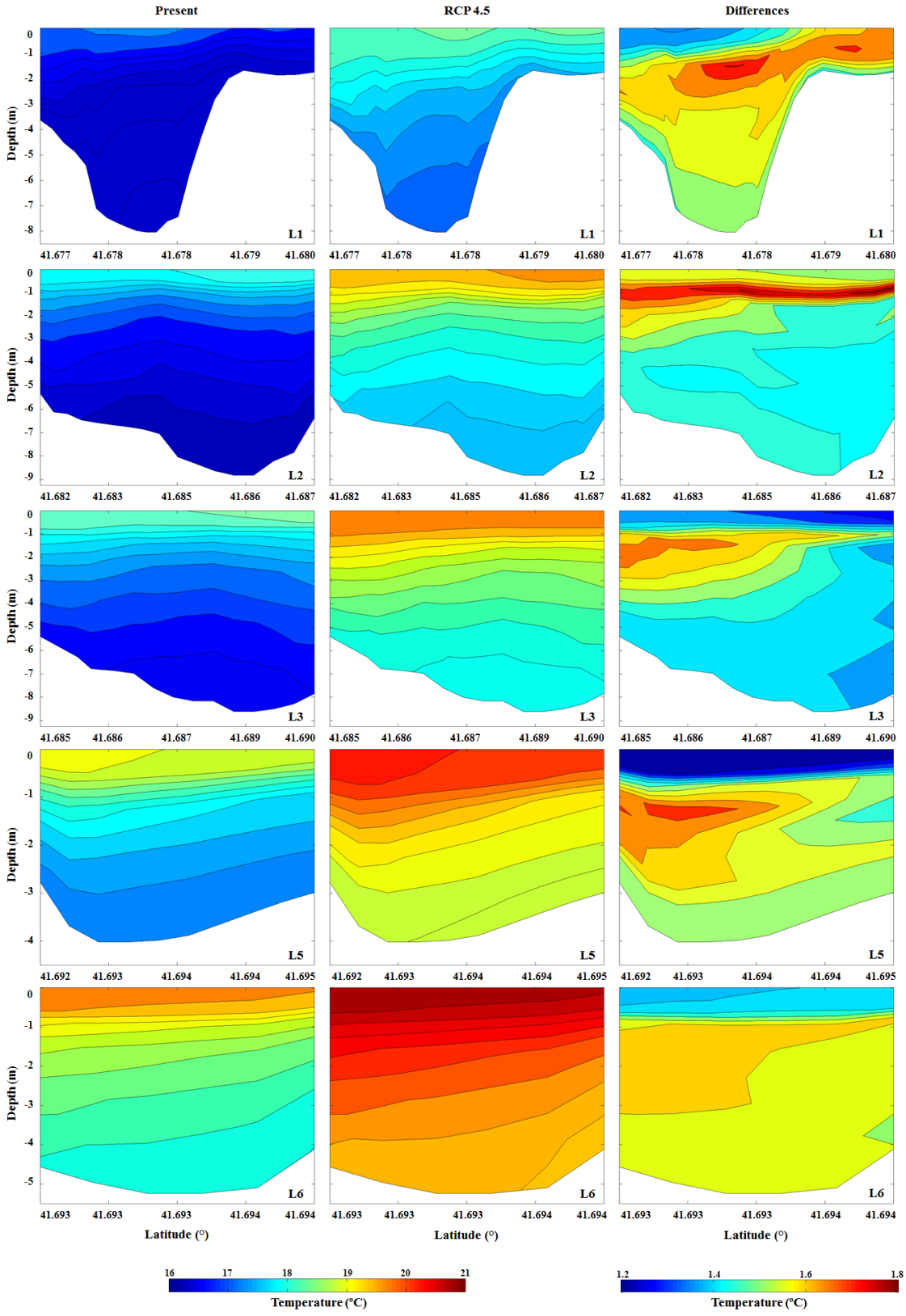

Figure 5.13: Vertical sections of water temperature averaged over the tidal cycle during summer conditions. From left to right columns: Present; RCP 4.5; differences between RCP 4.5 and Present. From top to bottom rows: transition from estuary mouth to estuary head.

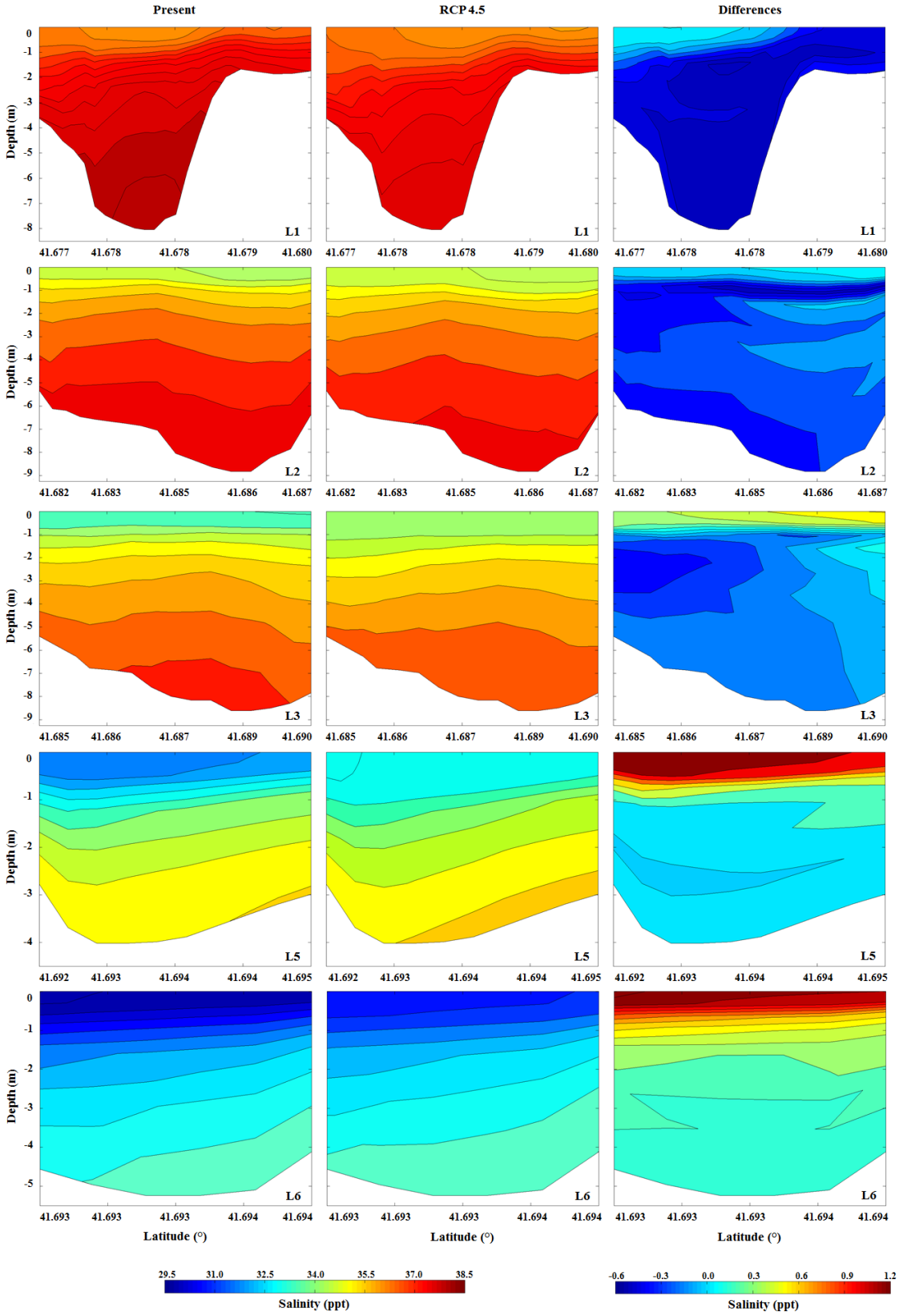

Figure 5.14: Vertical sections of salinity averaged over the tidal cycle during summer conditions. From left to right columns: Present; RCP 4.5; differences between RCP 4.5 and Present. From top to bottom rows: transition from estuary mouth to estuary head.

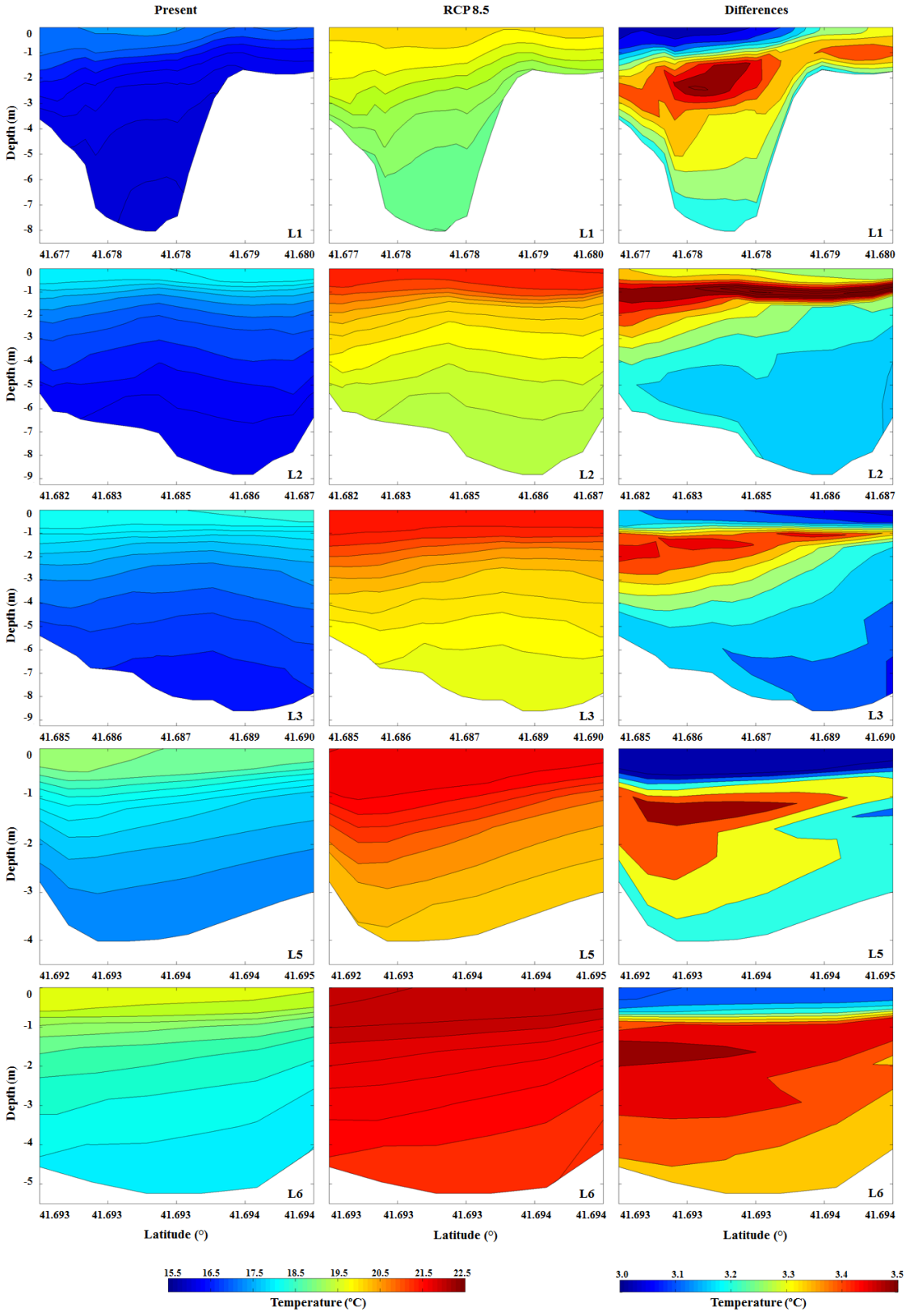

Figure 5.15: Vertical sections of water temperature averaged over the tidal cycle during summer conditions. From left to right columns: Present; RCP 8.5; differences between RCP 8.5 and Present. From top to bottom rows: transition from estuary mouth to estuary head.

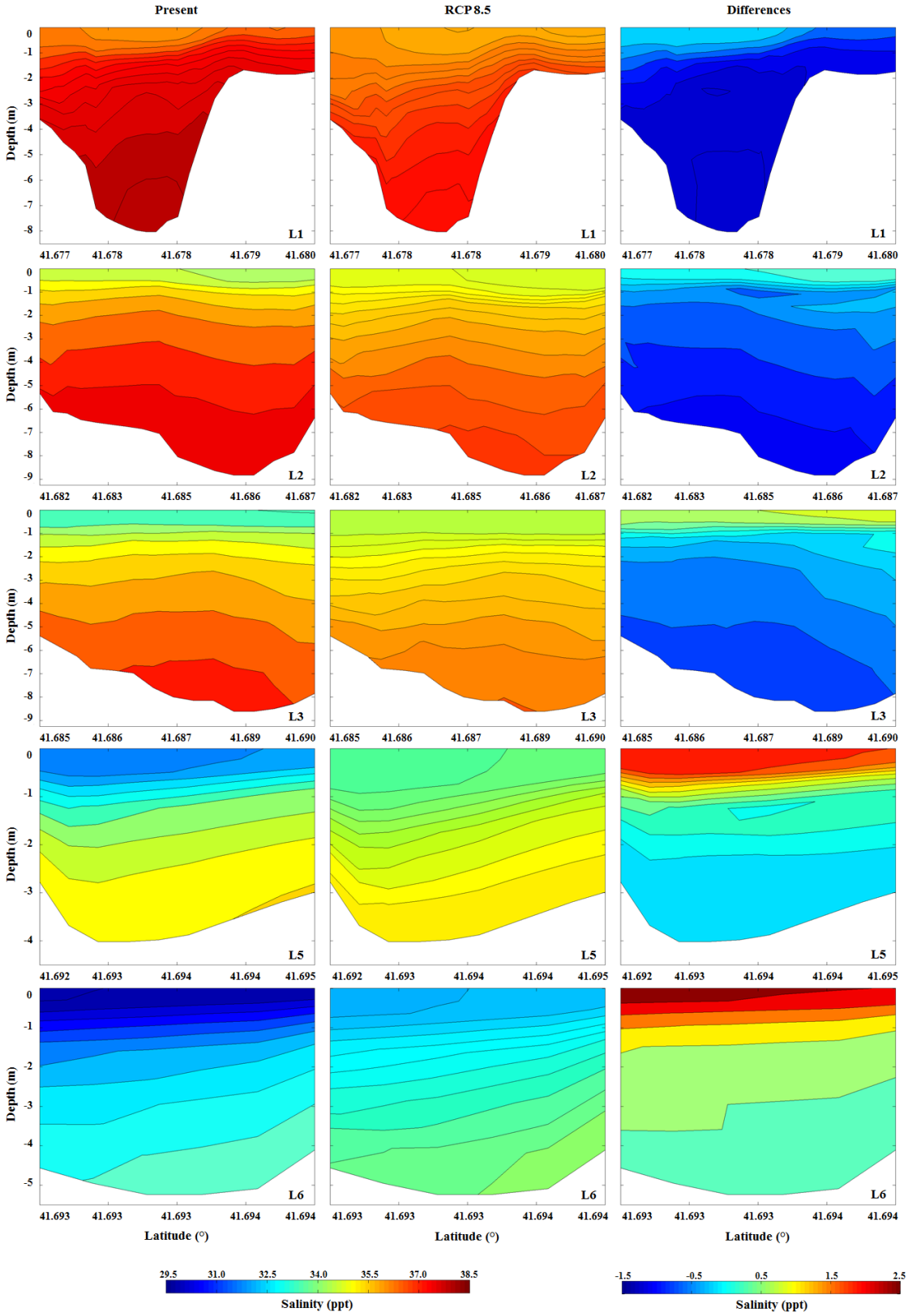

Figure 5.16: Vertical sections of salinity averaged over the tidal cycle during summer conditions. From left to right columns: Present; RCP 8.5; differences between RCP 8.5 and Present. From top to bottom rows: transition from estuary mouth to estuary head.

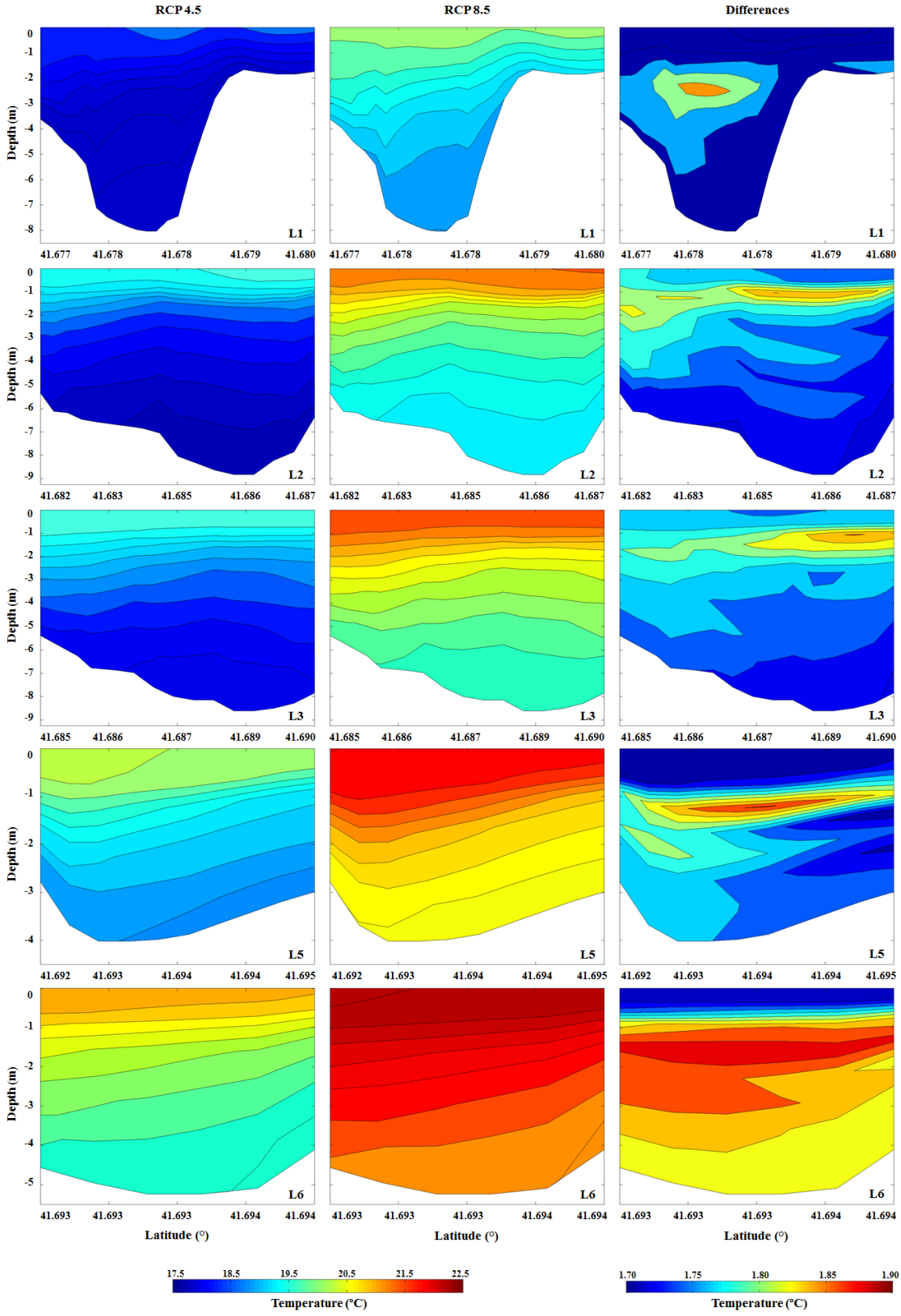

Figure 5.17: Vertical sections of water temperature averaged over the tidal cycle during summer conditions. From left to right columns: RCP 4.5; RCP 8.5; differences between RCP 8.5 and RCP 4.5. From top to bottom rows: transition from estuary mouth to estuary head.

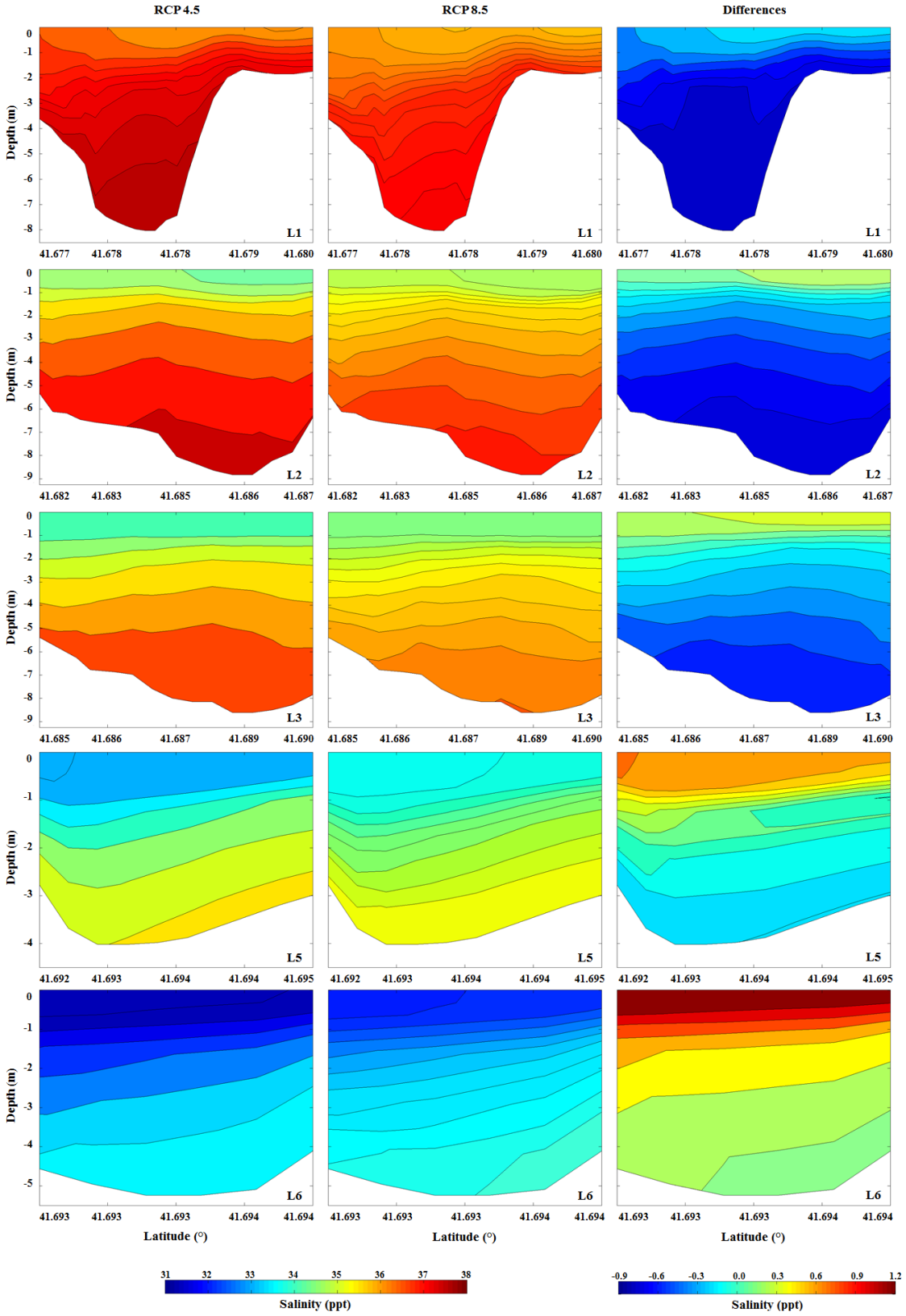

Figure 5.18: Vertical sections of salinity averaged over the tidal cycle during summer conditions. From left to right columns: RCP 4.5; RCP 8.5; differences between RCP 8.5 and RCP 4.5. From top to bottom rows: transition from estuary mouth to estuary head.

Winter Conditions

Figures 5.19 and 5.20 show, respectively, the comparison of water temperature and salinity averaged over the tidal cycle, between Present and RCP 4.5 scenarios, during winter conditions.

The model predictions of water temperature for Present scenario, presented in the first column of Figure 5.19, show a negative longitudinal gradient, declining from 15 ºC in L1 to 13.5 ºC in L6. A lateral homogeneity was found through all sections. This first column also shows a vertical gradient in all sections. As in summer figure, this stratification has differences of 1 ºC from the surface to the bottom, and it is more evident in L2 and L3 sections. The existence of a surface layer in the water column, founded in Figure 5.13 for L2, L3, L5 and L6 sections, ceased under winter conditions. This is explained by the increased river discharge for this time of the year (60 m^3s^{-1}).

Regarding salinity, the first column of Figure 5.20 shows a typical longitudinal estuarine gradient, with higher salinity values downstream (L1 section) and lower upstream (L6 section), as in summer figure. However, in this case the salinity values range from 12 to 36 ppt, while in summer ranged from 30 to 38 ppt.

The lateral homogeneity is also found in this figure. As in Figure 5.19, it is found a vertical structure from L1 to L6, but the superficial layer no longer exists. In L2 and L3 sections, it is found a stronger stratification (ranging from 22 ppt at the surface to 34 at the bottom).

For RCP 4.5 scenario, the water temperature sections (second column in Figure 5.19) present a similar pattern comparing with Present scenario, but with higher values, due to the implemented climate change presented in section 5.1. The changes in ocean water temperature and sea level rise, induce the increase of water temperature inside the estuary. The longitudinal gradient is similar to the Present scenario, with water temperature decreasing from L1 to L6. The sea level rise and river discharge induce this raise, providing a higher volume of ocean water (hotter) and a higher river flow (colder) into the estuary.

The model predictions continues to show a homogeneous lateral structure. It is found a similar water temperature vertical stratification, but with higher values comparing with Present scenario. The predicted salinity changes for RCP 4.5 scenario, presented in the second column of Figure 5.20, show similar longitudinal, lateral and vertical gradients for water temperature, but also with higher values.

The third column of Figures 5.19 and 5.20 presents the differences between Present and RCP 4.5 scenarios for water temperature and salinity, respectively. The higher differences for water temperature are predicted for the bottom (with maximum value of 1.6 ºC), and the higher differences of salinity are predicted for the left margin of L2, L3 and L5 sections.

For RCP 8.5 scenario, the water temperature sections (second column of Figure 5.21), are similar to those found for Present scenario, but with higher values. It is found an increase between 2.5 and 3.5 ºC in all sections, more intensified in L1 section. Once again, this occur due to sea level rise (+0.82 m) and ocean water temperature increase (+3.20 ºC).

The predicted salinities in RCP 8.5 scenario are presented in Figure 5.22. Comparing with Present scenario, the salinity increases (6.5 ppt) in the surface of L5 and L6 sections, and decreases in the bottom of L1 and L2 sections. The decrease in ocean salinity (-1.55 ppt) explains the model predictions in L1 and L2. The sea level rise, combined with lower river discharge and more intense solar radiation, leads to the vertical pattern found in L5 and L6 sections.

At last, the comparison between RCP 4.5 and RCP 8.5 scenarios is presented in Figures 5.23 and 5.24. The first figure shows the water temperature, where are found very small differences (ranging between 1.50 and 1.80 ºC), which are more evident at the surface. In Figure 5.24, the differences presented in the third column show that the upstream sections (L5 and L6) will suffer an increase of 3.5 and 4.5 ppt at the surface, respectively For the downstream sections (L1, L2 and L3), model predicts less saline water at the bottom and more saline water at the surface.

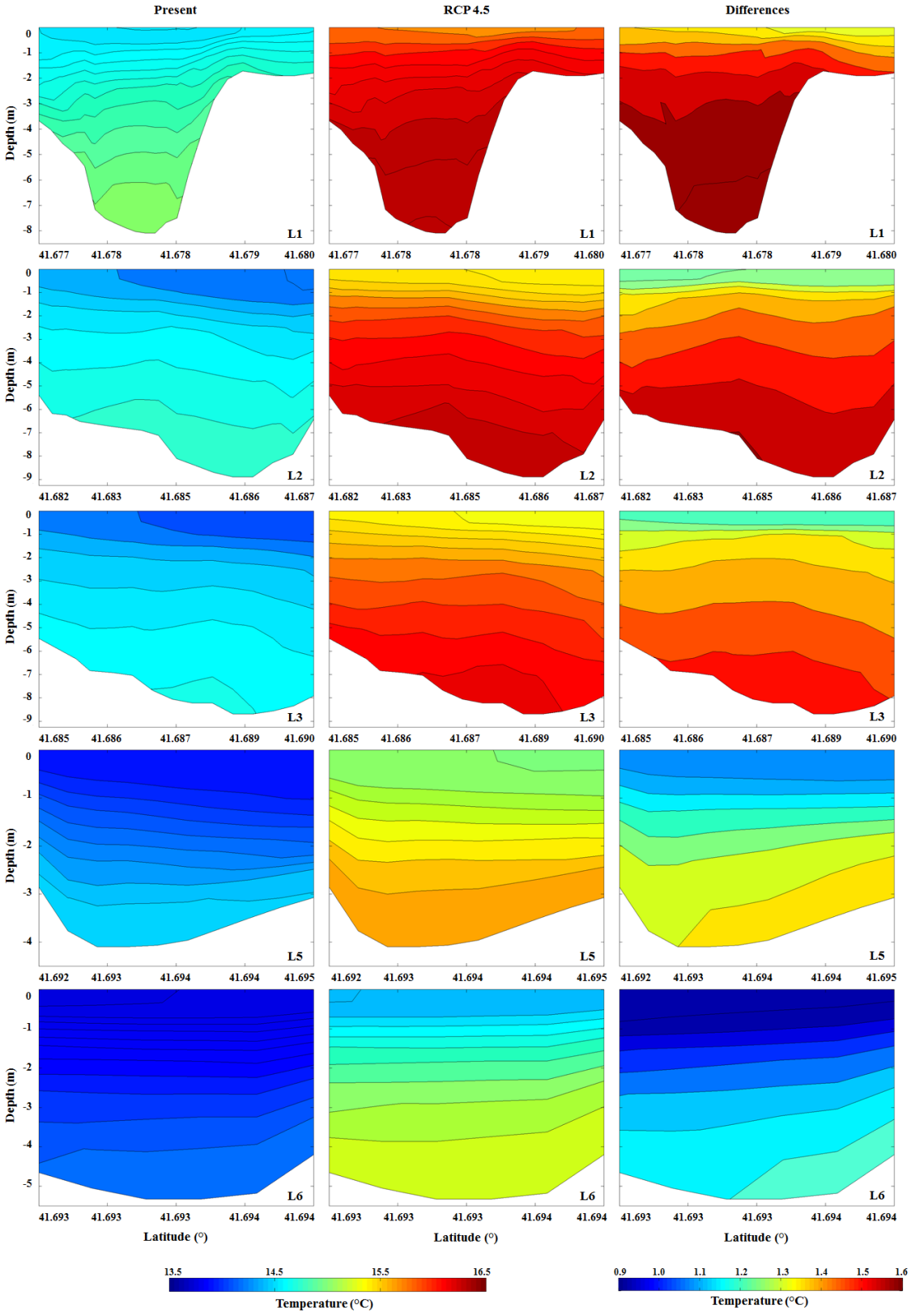

Figure 5.19: Vertical sections of water temperature averaged over the tidal cycle during winter conditions. From left to right columns: Present; RCP 4.5; differences between RCP 4.5 and Present. From top to bottom rows: transition from estuary mouth to estuary head.

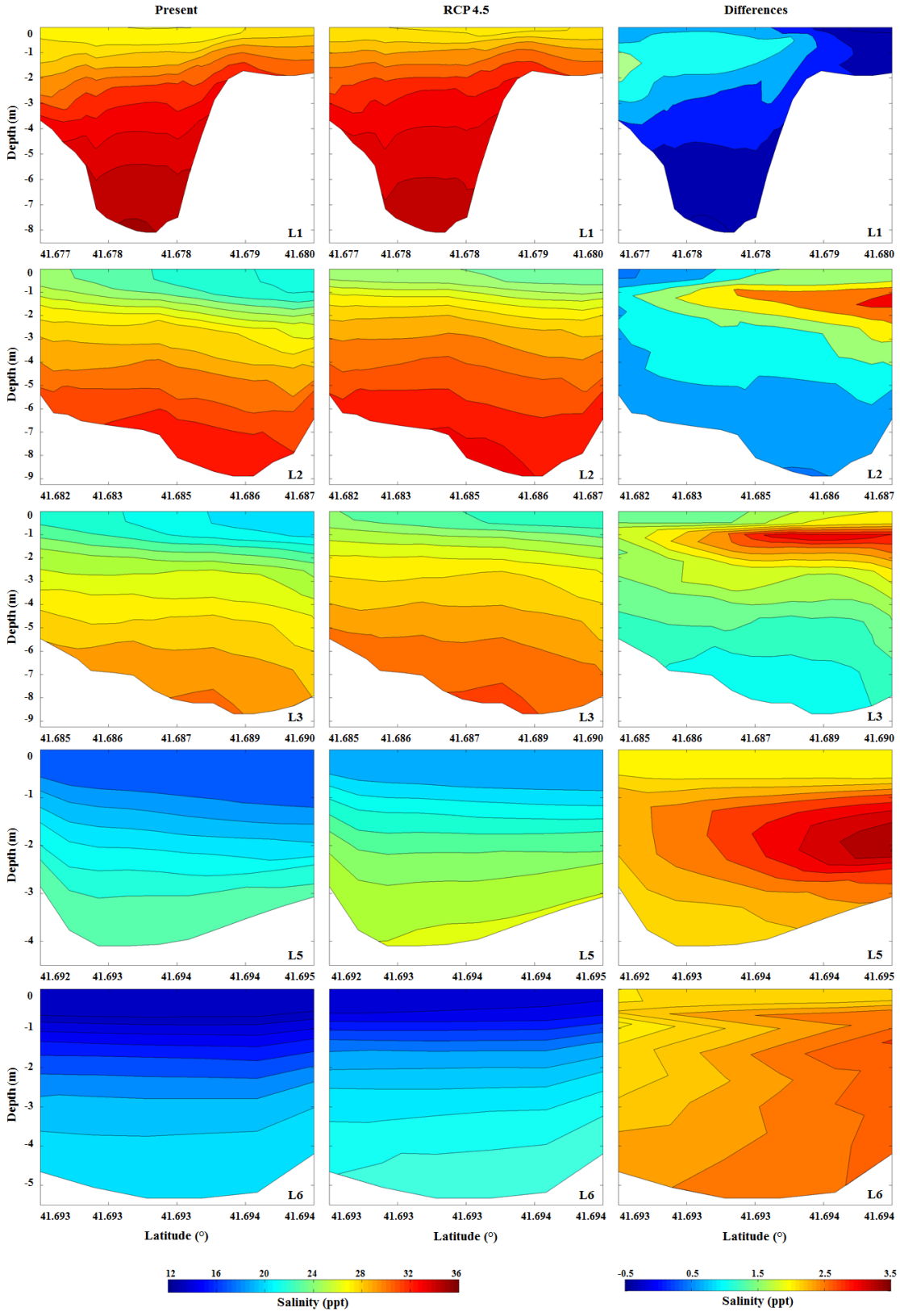

Figure 5.20: Vertical sections of salinity averaged over the tidal cycle during winter conditions. From left to right columns: Present; RCP 4.5; differences between RCP 4.5 and Present. From top to bottom rows: transition from estuary mouth to estuary head.

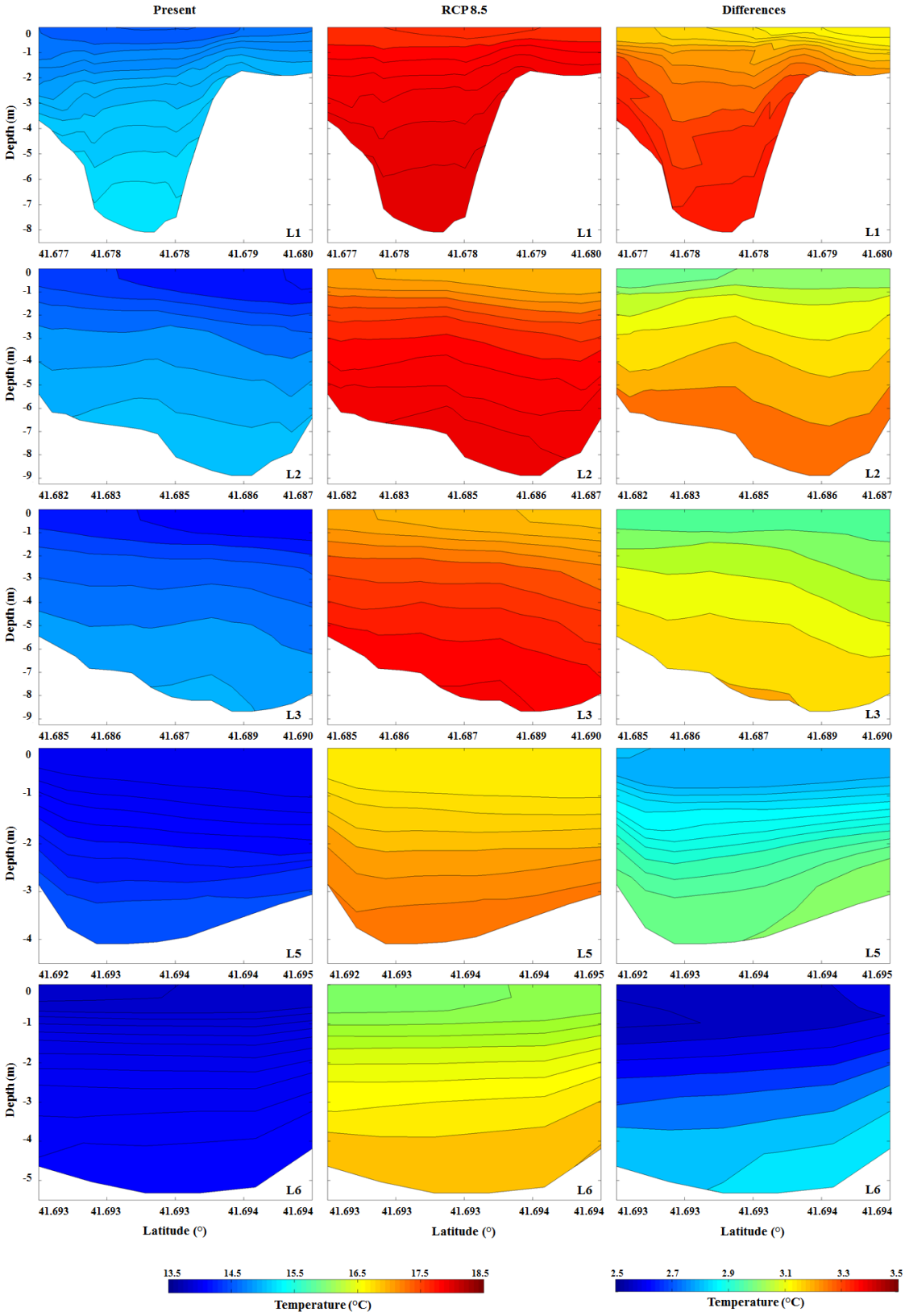

Figure 5.21: Vertical sections of water temperature averaged over the tidal cycle during winter conditions. From left to right columns: Present; RCP 8.5; differences between RCP 8.5 and Present. From top to bottom rows: transition from estuary mouth to estuary head.

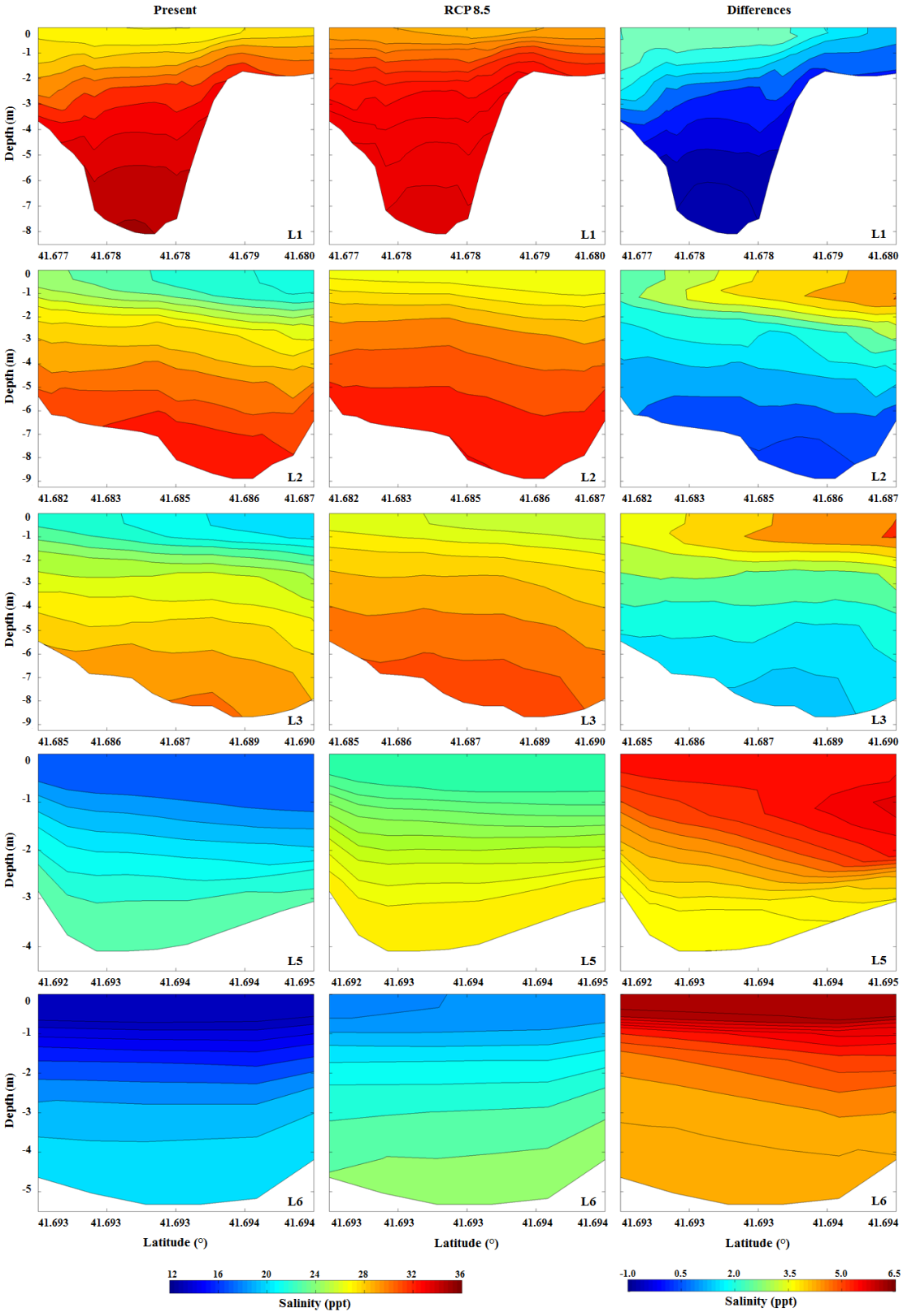

Figure 5.22: Vertical sections of salinity averaged over the tidal cycle during winter conditions. From left to right columns: Present; RCP 8.5; differences between RCP 8.5 and Present. From top to bottom rows: transition from estuary mouth to estuary head.

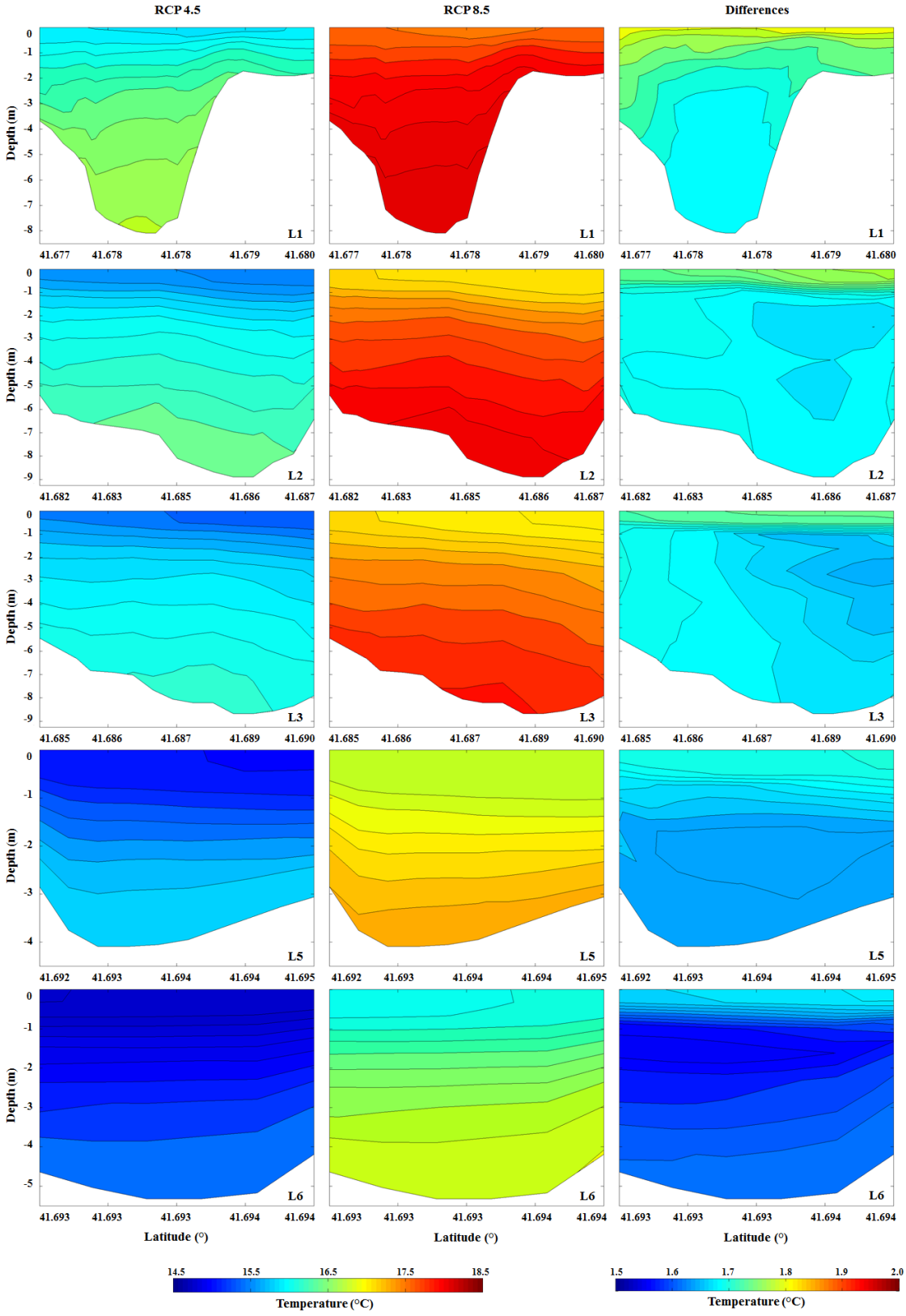

Figure 5.23: Vertical sections of water temperature averaged over the tidal cycle during winter conditions. From left to right columns: RCP 4.5; RCP 8.5; differences between RCP 8.5 and RCP 4.5. From top to bottom rows: transition from estuary mouth to estuary head.

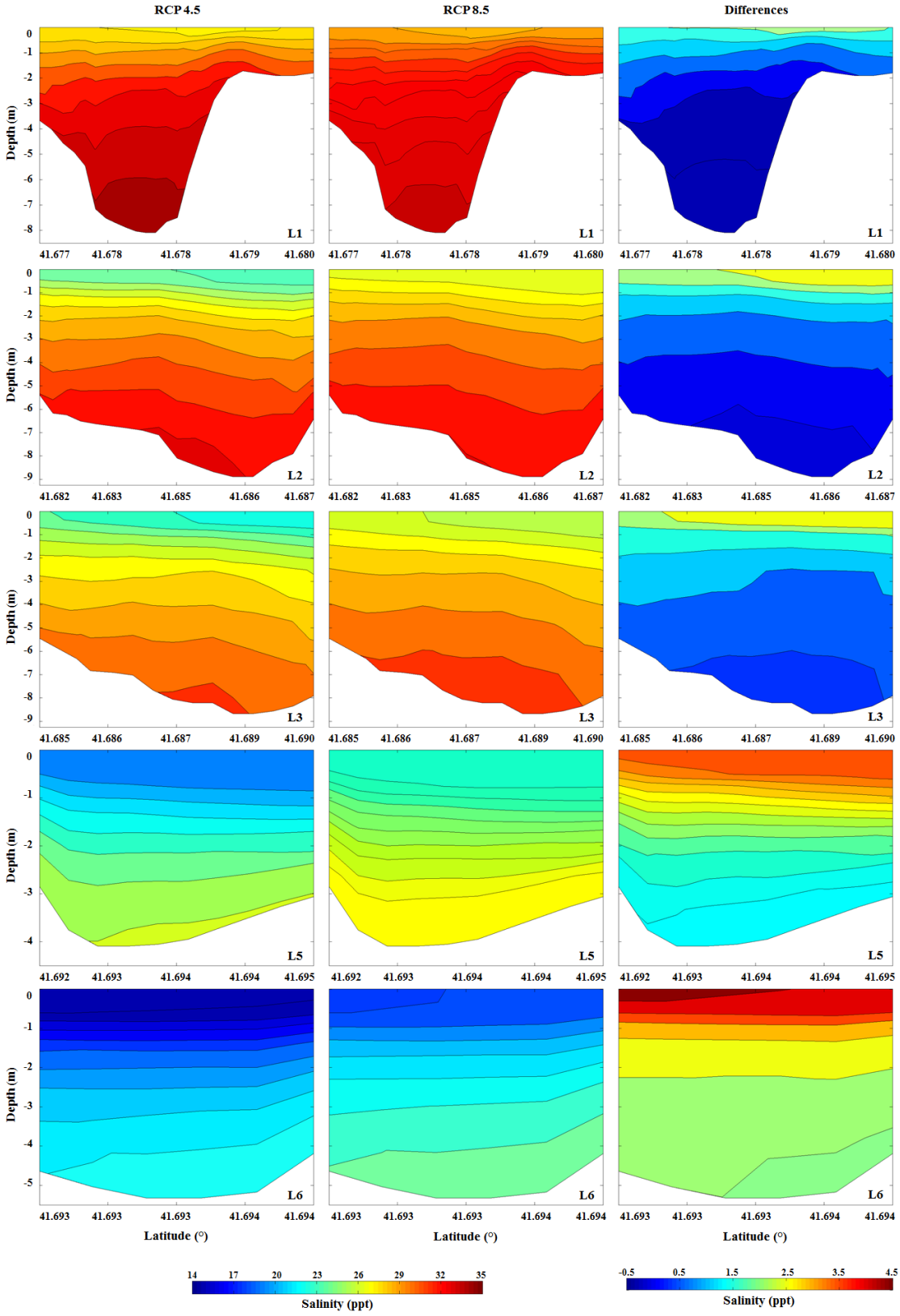

Figure 5.24: Vertical sections of salinity averaged over the tidal cycle during winter conditions. From left to right columns: RCP 4.5; RCP 8.5; differences between RCP 8.5 and RCP 4.5. From top to bottom rows: transition from estuary mouth to estuary head.

5.3 Salt Intrusion

The salt water movement upward estuarine systems is called saline or salt intrusion. The water coming from the ocean has a higher salt content than freshwater from the rivers. When these two water bodies meet, salt water, being more dense, sinks in relation to freshwater, which causes salt intrusion to occur in wedge shape near the bottom (Johnson, 2007). Consequently, the salt intrusion was analysed in layer 10 (bottom layer) of the model.

The analytical computation of salt intrusion in estuaries uses theoretical equations to predict the mixing behaviour of the estuary based on channel topography, river discharge and tidal characteristics. The influence of rainfall and evaporation on salt intrusion is also important, and sometimes is crucial to understand the salinity distribution (Savenije, 2012).

One type of estuarine classification system is the Venice system (Carriker, 1967). In this system it is considered six fundamental sections in an estuary, based on the longitudinal distribution of salinity: Limnetic zone (river section with salinity less than 0.5); Oligohaline zone (estuary head with salinity from 0.5 to 5); Mesohaline zone (upper section of the estuary with salinity from 5 to 18); Polyhaline zone (covering the middle and lower sections of the estuary): middle section with salinity from 18 to 25, and lower section with salinity from 25 to 30; and Euhaline zone (estuary mouth with salinity from 30 to 36). In this work, it is considered that the saline intrusion extends to 0.5 ppt of salinity.

Figure 5.25 shows the salt intrusion in high tide during summer conditions for both estuaries under study. In Minho estuary, the length of the saline intrusion for Present and RCP 4.5 scenarios was 13 km, while for RCP 8.5 scenario was 14 km. In Lima estuary the length of the salt intrusion was slightly higher, reaching 15 km in Present and RCP 4.5 scenarios, and 17.5 km in RCP 8.5 scenario.

The highest values in Lima estuary can be explained by fluvial effect. Lima river has a discharge about six times lower than the Minho river (See Figure 4.2), which makes Lima estuary more saline. The increase of the salt wedge that occurs in RCP 8.5 scenario can be explained by the sea level rise of about 0.82 m. This increase in the sea level causes a higher volume of saline water entering in the estuary, promoting the prolongation of the salt wedge.

The first row of this figure shows the comparison between Present and RCP 4.5 scenarios. Here, it is observed that there was a decrease of the salinity in the whole domain. The higher differences are in the upper part of the estuaries. Comparing Present and RCP 8.5 scenarios, it is found that the differences become positive at the upper estuary zone in both sites. Positive differences show higher saline values in RCP 8.5 and negative differences shows the opposite.

Lastly, the third row presents the comparison between RCP 4.5 and RCP 8.5 scenarios, where are observed blue values near the estuary mouth and red values from the center part to the head of the estuary. This means that in the future these estuaries will become more saline in the inner part and less saline near the mouth during summer.

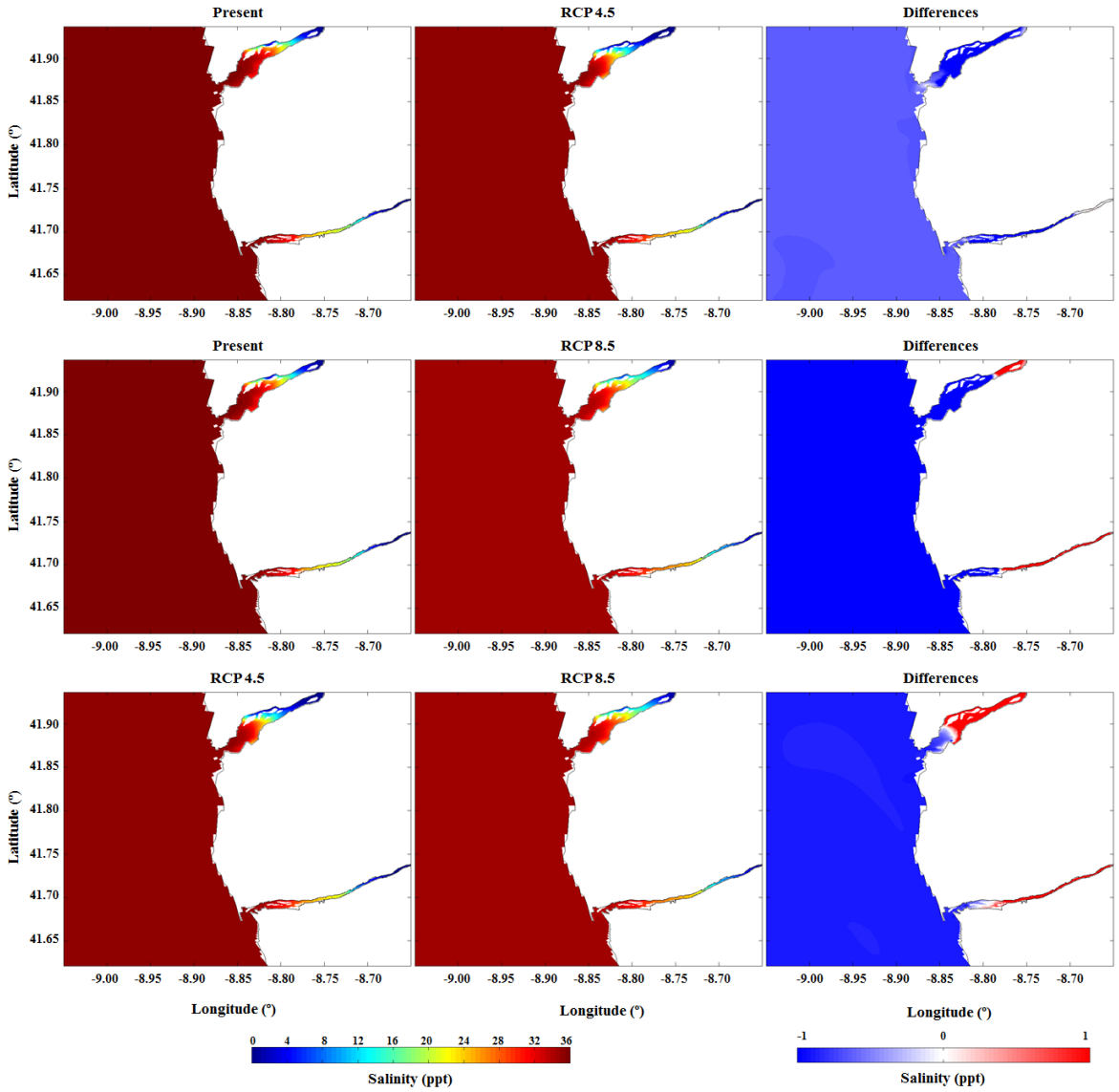

Figure 5.25: Salt intrusion, at high tide, during summer conditions. First row: Present; RCP 4.5; diff. between RCP 4.5 and Present. Second row: Present; RCP 8.5; diff. between RCP 8.5 and Present. Third row: RCP 4.5; RCP 8.5; diff. between RCP 8.5 and RCP 4.5.

Figure 5.26 shows the salt intrusion, also in high tide, but during winter conditions. In Minho estuary, the length of the salt intrusion for the Present scenario was 7 km, for RCP 4.5 was 9 km and for RCP 8.5 was 11 km. In Lima estuary the length of the salt intrusion was slightly higher, reaching 8.5 km in Present scenario, 10 km in RCP 4.5 and 11.5 km in RCP 8.5. In this case, comparing with summer conditions, occurs a decrease in the total saline intrusion, and between scenarios the saline intrusion increases progressively. The decrease of the salt intrusion can be explained by the rise of fluvial flows, comparing with summer conditions. In Minho river, the discharge value changed from $\sim$120 to $\sim$360 m^3s^{-1}, while in Lima river from $\sim$20 to $\sim$60 m^3s^{-1}.

Regarding the changes between the three scenarios, the column with the differences shows that in the future there may be an increase in saline intrusion within the estuaries. In the first and second rows, are found negative values of salinity near the estuaries mouth, which means that the imposed decrease of salinity in the RCP 4.5 and RCP 8.5 scenarios is felted in this zone. The positives values show that salinity will raise in the future, even under winter conditions.

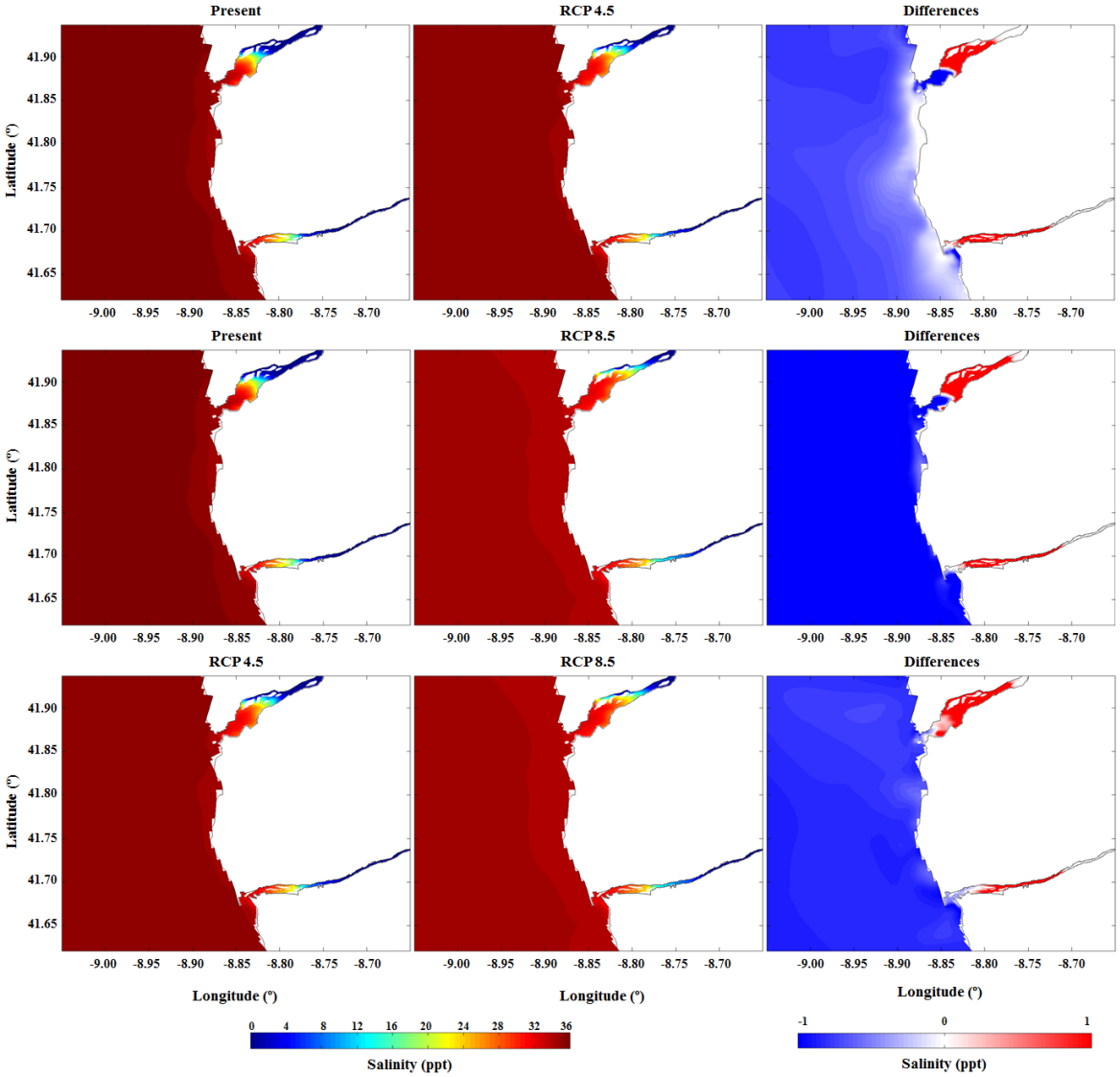

Figure 5.26: Salt intrusion, at high tide, during winter conditions. First row: Present; RCP 4.5; diff. between RCP 4.5 and Present. Second row: Present; RCP 8.5; diff. between RCP 8.5 and Present. Third row: RCP 4.5; RCP 8.5; diff. between RCP 8.5 and RCP 4.5.

5.4 Estuarine Plume

Estuarine discharges generate coastal water masses with low density, carrying several dissolved and suspended riverine materials with distinct properties from surrounding ocean waters. The river or estuarine plume is the river outflow to the coast that can be observed near the estuaries mouth by the different colour between river and ocean waters (Mendes et al., 2016).

The impact and dispersion of riverine material along coast depends on physical processes, which determine the plume fate over shelf (Horner-Devine et al., 2015). Plumes spread and advect material across long distances providing a mechanism for horizontal redistribution of nutrients and/or pollutants (Ribeiro, 2015). This dynamic is controlled by the interaction of outflow inertia, buoyancy, Earth's rotation, wind forcing and alongshore coastal current (Sousa, 2013). Being buoyancy a characteristic of the estuarine plumes, in this work, the plume is identified in the superficial layer (layer 1) of the model.

The Western Iberian Buoyant Plume (WIBP) is a large buoyant plume formed by the accumulation of a less dense water mass originated from all estuarine out-flowing along northern Portuguese coast (Mendes et al., 2016). The dynamics of Minho river, one of the WIBP contributors, was previously studied by Sousa (2013), revealing a rapid response of the plume to wind variations.

Figure 5.27 presents the horizontal velocities at Minho and Lima Mouths, and Figure 5.28 shows the surface salinity variation after the ebb, during summer conditions. This way, is visualised the formation of estuarine plumes in both estuaries. In Minho, it is observed the generation of a bulge in all three scenarios, but with more intensity in Present scenario. This can be explained by the velocity patterns in the estuary mouth. As Figure 5.27 shows, the velocity in Present scenario is higher, at flood and ebb peak, comparing with RCP 4.5 and 8.5 scenarios (graphics a) and c)).

Another feature found is that the bulb generated is confined only to the zone in front of the estuary mouth. This pattern is induced by the winds considered in simulations. At this location winds blew predominantly from East and with low intensity (about 4 ms^{-1}) during the previous two days, which confines the plume near to the estuary entrance. This result is consistent with Sousa (2013) that revealed that the Minho plume has a similar pattern during identical wind conditions (East winds with a velocity of 3 ms^{-1}).

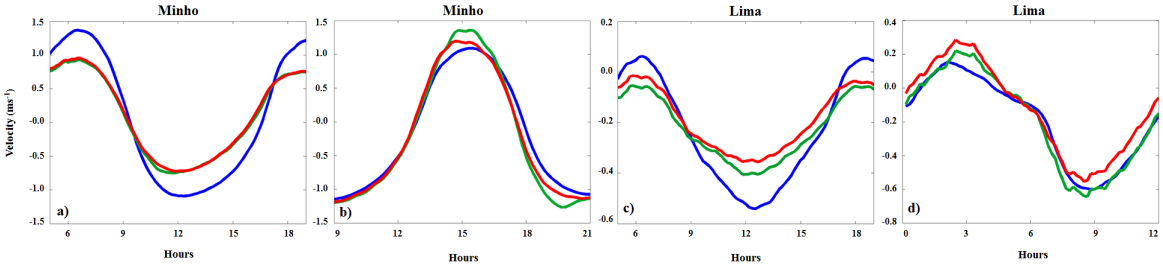

Figure 5.27: Horizontal velocity in the center of the mouth of Minho and Lima estuaries. a) and b) flow velocity in E-W direction for summer and winter, respectively. c) and d) flow velocity in N-S direction for summer and winter, respectively. Scenarios: Present (blue), RCP 4.5 (green) and RCP 8.5 (red).

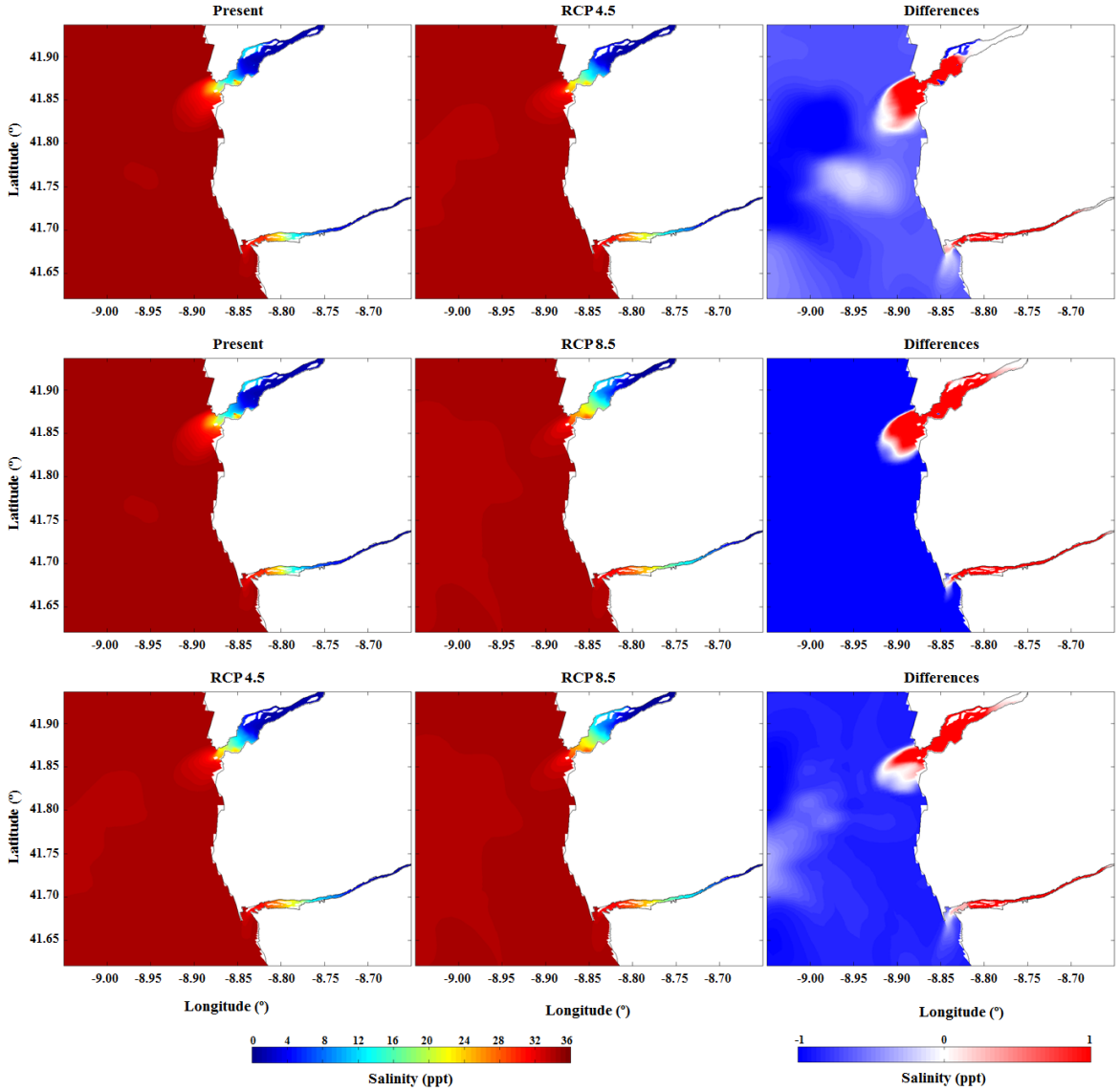

Figure 5.28: Surface water temperature, after the ebb, during summer conditions. First row: Present; RCP 4.5; diff. between RCP 4.5 and Present. Second row: Present; RCP 8.5; diff. between RCP 8.5 and Present. Third row: RCP 4.5; RCP 8.5; diff. between RCP 8.5 and RCP 4.5.

Figure 5.29 presents the surface salinity under winter conditions. In this case the plume's generation it is more evident that during summer conditions. This difference is justified by the river discharge increase from the summer case. During winter conditions the river flux is six times higher than in summer, and the predominant wind is from Southwest with an average velocity of 8 ms^{-1} leading the plumes to North.

Unlike summer case, during winter the plume size increases for the two future scenarios (first and second rows). At first sight this increment looks contradictory, since the river discharges diminish in the future and therefore the decrease of the plume dimension would be expected. However, the sea level rise will increase the ebb currents (see Figure 5.27), justifying this changes.

Finally, Figure 5.29 shows a connection between Minho and Lima plumes near the coast. This proves that under special conditions, like high river flow and favourable wind velocity and direction, the Lima plume can interact the Minho plume. Then this "new" larger plume starts to move North, integrating the WIBP.

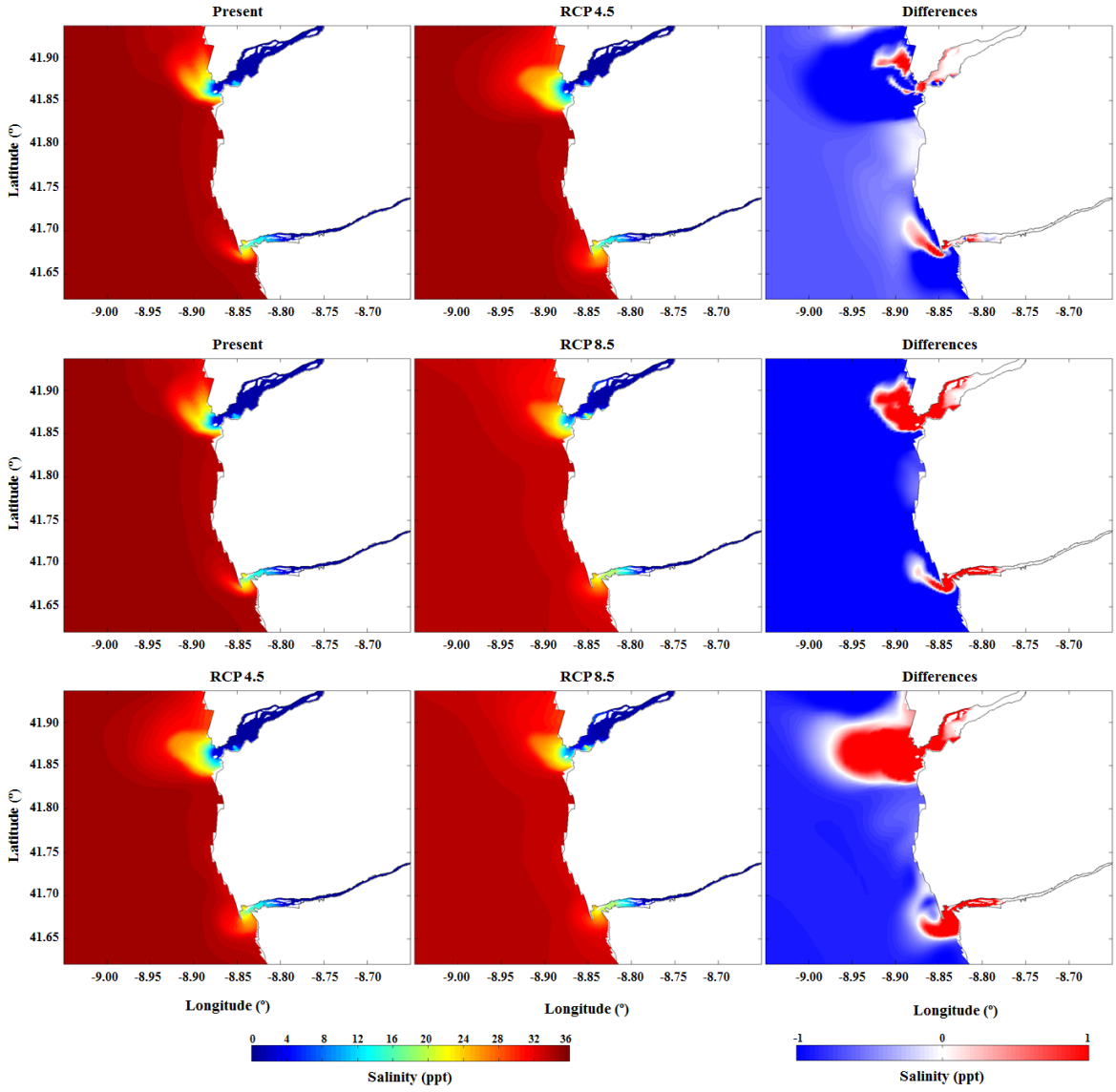

Figure 5.29: Surface water temperature, after the ebb, during winter conditions. First row: Present; RCP 4.5; diff. between RCP 4.5 and Present. Second row: Present; RCP 8.5; diff. between RCP 8.5 and Present. Third row: RCP 4.5; RCP 8.5; diff. between RCP 8.5 and RCP 4.5.

Chapter 6

Final Conclusions

Human activity is being pointed out as the main cause of climate change, also called global warming. Nowadays, the study of climate change impacts on estuaries and coastal zones has been increasingly sought and fulfilled, considering the high socio-economic importance of these coastal systems.

Minho and Lima estuaries have different characteristics that have been previously studied individually through dedicated numerical modelling applications. However, the coupled modelling of this two estuaries in a single model application was never done before. The presented study considers both Minho and Lima estuaries in a single model implementation, that has the ability to predict the integrated hydrological response of the estuaries under climate change forcing.

The modelling process was done using the three-dimensional hydrodynamic model Delft3D-Flow. This model was implemented in both estuaries with a grid size of 200 $\times$ 200 m near coast line, 50 $\times$ 70 m in Minho estuary and 20 $\times$ 30 m in Lima estuary, with 10 vertical layers. The model's calibration was successfully performed through comparison between model predictions and field data, showing the models accuracy in reproducing the local tidal propagation and salt and heat transport.

After model's calibration, were defined three scenarios to study the hydrological response of the estuaries to climate change. The calibration run, for the year 2012, was defined as Present scenario. Scenarios based on RCP 4.5 and RCP 8.5 projection were defined changing the ocean, atmospheric and river boundaries of the model.

For RCP 4.5 scenario, the principal changes in ocean and river boundaries were in the sea level (+0.32 m), ocean water temperature (+1.55 ºC), ocean salinity (-0.65 ppt) and river discharge (-5%). For RCP 8.5 scenario, the ocean and river boundaries changes were also applied in the sea level (+0.82 m), ocean water temperature (+3.20 ºC), ocean salinity (-1.55) and river discharge (-25%). Atmospheric boundary changes were applied monthly into the air temperature, humidity, solar radiation and wind velocity.

Model results were analysed considering vertical sections, salt intrusion and estuarine plume generation. For each scenario were presented the salinity and water temperature estuarine responses under summer and winter conditions. The differences between summer and winter conditions were defined by distinct river discharge, air and water temperature and wind velocity.

Model predictions showed that in Minho estuary during summer conditions the water temperature has longitudinal, lateral and vertical gradients. Longitudinally, the minimum water temperature value (17 ºC) was found for Present scenario in the downstream section, and the maximum value (25 ºC) in RCP 8.5 scenario, in the upstream section. Laterally, the water temperature is higher in the South margin and lower in the North margin. These results show that the flood current flows through the North side, and the ebb current flows predominantly through the South side.

Vertically, this estuary presents a slight stratification, with water temperature decreasing from the surface to the bottom. Regarding salinity, the longitudinal structure showed higher values near the mouth, and less saline water upstream. The lateral structure remains in salinity predictions, showing less saline water in the South margin of M2, M3 and M5 sections. The vertical structure shows a stratification similar to that presented for water temperature.

During winter conditions, the minimum and maximum values of water temperature are lower than for summer, and the longitudinal, lateral and vertical structures reverse comparing to summer conditions. This inversion is induced by the decrease of the river water temperature and the increase of the river discharge. The air and ocean temperature also decreases, but with lower effect.

Longitudinally, the minor water temperature value (12.5 ºC) occurs in M6, and the major value (17.5 ºC) occurs in M1. Laterally, the water temperature increases from South to North, resulting from the predominant flood current flowing into the estuary along the North side. Vertically, the water temperature increase from the surface to the bottom. Regarding salinity was found a similar pattern both in summer and winter conditions. The lower salinity value occurred in M6 (2 ppt), and the higher salinity value (29 ppt) was predicted for M1.

Regarding Lima estuary, its dynamic is lower than that described for Minho estuary. The model predictions showed that the water temperature longitudinal structure is different during summer and winter conditions. As in Minho estuary, in summer the water temperature increases from L1 to L6, and during winter the water temperature decreases from L1 to L6. The lateral structure remains the same during summer and winter. Vertically, it was found a solid stratification comparing with Minho estuary, and in summer the water temperature decreases from the surface to the bottom. However, in winter the water temperature increases.

The salinity changes in Lima estuary have the same pattern during summer and winter. Model results showed a typically estuarine longitudinal gradient with high saline water in the sections downstream and less saline water in the sections upstream. However, the Lima estuary is much more saline than the Minho estuary, due to the Lima's low fluvial discharge. As in water temperature, the salinity is laterally homogeneous. The winter vertical stratification has the same pattern found for the summer stratification, with higher saline water near the bottom and less saline near the surface.

The salt intrusion was also studied in this work. During summer, in Minho estuary, the length of the saline intrusion for the Present and RCP 4.5 scenarios was 13 km and for RCP 8.5 was 14 km. In Lima estuary, the length of the salt intrusion was slightly higher, reaching 15 km in Present and RCP 4.5 scenarios, and 17.5 km in RCP 8.5.

From this results is concluded that the salt intrusion will keep unchanged for future when RCP 4.5 scenario is considered. However, the applied changes in RCP 8.5 scenario will promote an extension of the saline intrusion in both estuaries (1 km in Minho estuary and 2.5 km in Lima estuary). During winter conditions, the extension gradually increases between each scenario. In Minho estuary the predicted salt intrusion for Present scenario was 7 km, for RCP 4.5 scenario was 9 km and for RCP 8.5 scenario was 11 km. Regarding Lima estuary the saline intrusion length was 8.5, 10 and 11.5 km for the same scenarios.

Lastly, it was made the study about the estuarine plume generation and propagation. Model predictions show small plumes (with Lima plume much more smaller than Minho plume) in front of the estuaries mouth during summer season. It was also found that, during summer conditions the plume dimension will reduce in RCP 4.5 scenario and even more in RCP 8.5 scenario. However, during winter conditions it was found an opposite behaviour. In Present scenario, the model forecasts show the formation of a robust plume in Minho and a smaller plume in Lima. In RCP 4.5 scenario the plume expands in both estuaries, and in RCP 8.5 scenario the plume will be amplified but with the bulge core lower than for the RCP 4.5 scenario. However, it was found that the plume starts to move North integrating the WIBP.

After this analysis, it is concluded that the future sea level rise and decrease of river discharge are the major factors inducing the hydrological changes in both estuaries due to climate change. During summer, the Minho estuary will be hotter than Lima estuary, but Lima will be saltier than Minho. During winter, the Lima estuary will be hotter and more saline than Minho estuary.

In summary, the contributions given by this work to the scientific community are: first coupled modelling of Minho and Lima estuaries; first three-dimensional modelling of these estuaries, determining how they vary longitudinally, laterally and vertically; hydrological response of both estuaries to climatic changes.

For future work it is suggested the use of the present model set-up to force a water quality module, to study the biogeochemical characteristics of both estuaries and their responses to climate change.

References

Araújo, M., Mazzolari, A., and Trigo-Teixeira, A. (2011). Wave set-up in the modeling of storm surge at Viana do Castelo (Portugal). *Journal of Coastal Research*, 64:971–975.

Arndt, S., Lacroix, G., Gypens, N., Regnier, P., and Lancelot, C. (2011). Nutrient dynamics and phytoplankton development along an estuary-coastal zone continuum: a model study. *Journal of Marine Systems*, 84(3-4):49–66.

Atwater, M. A. and Ball, J. T. (1978). Computation of IR sky temperature and comparison with surface temperature. *Solar Energy*, 21(3):211–216.

Balsinha, M. J., Santos, A. I., Alves, A. M., and Oliveira, A. T. (2009). Textural composition of sediments from Minho and Douro estuaries (Portugal) and its relation with hydrodynamics. *Journal of Coastal Research*, SI 56:1330–1334.

Brown, C. A., Sharp, D., and Mochon Collura, T. C. (2016). Effect of climate change on water temperature and attainment of water temperature criteria in the Yaquina estuary, Oregon (USA). *Estuarine, Coastal and Shelf Science*, 169:136–146.

Cardoso, R., Araújo, M. F., Freitas, M. C., and Fatela, F. (2006). Geochemical characterisation of sediments from salt marsh environments of the Lima estuary. In *VI Congresso Ibérico de Geoquímica*, 305–308.

Cardoso, R., Araújo, M. F., Freitas, M. C., and Fatela, F. (2008). Geochemical characterisation of sediments from marginal environments of Lima estuary (NW Portugal). *Geosciences On-line Journal*, 5(6):1–11.

Carriker, M. R. (1967). Ecology of estuarine benthic invertebrates: a perspective. *Estuaries*, 83:442–487.

Costanza, R., Arge, R., de Groot, R., Farberk, S., Grasso, M., Hannon, B., Limburg, K., Naeem, S., O'Neill, R., Paruelo, J., Raskin, R., Suttonkk, P., and van den Belt, M. (1997). The value of the world ' s ecosystem services and natural capital. *Nature*, 387:253–260.

Courant, R., Friedrichs, K., and Lewy, H. (1928). On the partial difference equations of mathematical physics. *IBM Journal of Research and Development*, 100:32–74.

Delgado, A., Taveira-Pinto, F., and Silva, R. (2011). Hydrodynamic and morphodynamic preliminary simulation of river Minho estuary. *6ª Jornadas de Hidráulica, Recursos Hídricos e Ambiente*, 113–126.

Deltares (2014a). *Delft3D - FLOW (Simulation of multi-dimensional hydrodynamic flows and transport phenomena, including sediments) [User Manual]*. Boussinesqweg 1, Netherlands, 3.15.34158 edition, 684 pp.

Deltares (2014b). *Delft3D - RGFGRID (Generation and manipulation of curvilinear grids for Delft3D-Flow and Delft3D-Wave) [User Manual]*. Boussinesqweg 1, Netherlands, 4.00.34074 edition, 112 pp.

Deltares (2014c). *Delft3D - QUICKIN (Generation and manipulation of grid-related parameters such as bathymetry, initial conditions and roughness) [User Manual]*. Boussinesqweg 1, Netherlands, 4.00.34158 edition, 96 pp.

Dias, J. M. (2001). *Contribution to the study of the Ria de Aveiro hydrodynamics*. PhD thesis, Aveiro University, 288 pp.

Dias, J. M. and Lopes, J. F. (2006). Implementation and assessment of hydrodynamic, salt and heat transport models: the case of Ria de Aveiro lagoon (Portugal). *Environmental Modelling and Software*, 21(1):1–15.

Dias, J. M., Sousa, M. C., Bertin, X., Fortunato, A. B., and Oliveira, A. (2009). Numerical modeling of the impact of the Ancão Inlet relocation (Ria Formosa, Portugal). *Environmental Modelling and Software*, 24(6):711–725.

Elhakeem, A., Elshorbagy, W., and Bleninger, T. (2015). Long-term hydrodynamic modeling of the Arabian Gulf. *Marine Pollution Bulletin*, 94(1-2):19–36.

Falcão, A. P., Mazzolari, A., Gonçalves, A., Araújo, M., and Trigo-Teixeira, A. (2013). Influence of elevation modelling on hydrodynamic simulations of a tidally-dominated estuary. *Journal of Hydrology*, 497:152–164.

Ferreira, J. G., Simas, T., Nobre, A., Silva, M. C., Shifferegger, K., and Lencart-Silva, J. (2003). Identification of sensitive areas and vulnerable zones in transitional and coastal Portuguese systems. *INAG and IMAR*, 79–94.

Freitas, V., Costa-Dias, S., Campos, J., Bio, A., Santos, P., and Antunes, C. (2009). Patterns in abundance and distribution of juvenile flounder, Platichthys flesus, in Minho estuary (NW Iberian Peninsula). *Aquatic Ecology*, 43:1143–1153.

Fry, V. A. and Aubrey, D. G. (1990). Tidal velocity asymmetries and bedload transport in shallow embayments. *Estuarine, Coastal and Shelf Science*, 30(5):453–473.

Garcia, M., Ramirez, I., Verlaan, M., and Castillo, J. (2015). Application of a three-dimensional hydrodynamic model for San Quintin Bay, B.C., Mexico. Validation and calibration using OpenDA. *Journal of Computational and Applied Mathematics*, 273:428–437.

Godin, G. (1972). *The Analysis of Tides*. University of Toronto Press, Toronto, 264 pp.

Grunnet, N. M., Ruessink, B. G., and Walstra, D. J. (2005). The influence of tides, wind and waves on the redistribution of nourished sediment at Terschelling, The Netherlands. *Coastal Engineering*, 52(7):617–631.

Horner-Devine, A. R., Hetland, R. D., and MacDonald, D. G. (2015). Mixing and transport in coastal river plumes. *Annual Review of Fluid Mechanics*, 47(1):569–594.

Hu, K., Ding, P., Wang, Z., and Yang, S. (2009). A 2D/3D hydrodynamic and sediment transport model for the Yangtze estuary, China. *Journal of Marine Systems*, 77(1-2):114–136.

Johnson, T. (2007). Battling seawater intrusion in the Central & West Coast basins. *Water Replenishment District of Southern California*, 13:2.

Lazzari, P., Mattia, G., Solidoro, C., Salon, S., Crise, A., Zavatarelli, M., Oddo, P., and Vichi, M. (2014). The impacts of climate change and environmental management policies on the trophic regimes in the Mediterranean Sea: scenario analyses. *Journal of Marine Systems*, 135:137–149.

Macías, D., Castilla-Espino, D., García-del Hoyo, J. J., Navarro, G., Catalán, I. A., Renault, L., and Ruiz, J. (2014). Consequences of a future climatic scenario for the anchovy fishery in the Alboran Sea (SW Mediterranean): a modeling study. *Journal of Marine Systems*, 135:150–159.

MacMillan, D. S., Beckley, B. D., and Fang, P. (2004). Monitoring the TOPEX and Jason - 1 microwave radiometers with GPS and VLBI wet zenith path delays. *Marine Geodesy*, 27:703–716.

Marta-Almeida, M., Reboreda, R., Rocha, C., Dubert, J., Nolasco, R., Cordeiro, N., Luna, T., Rocha, A., Lencart-Silva, J., Queiroga, H., Peliz, A., and Ruiz-Villarreal, M. (2012). Towards operational modeling and forecasting of the Iberian Shelves ecosystem. *PLoS ONE*, 7(5):1–12.

Marujo, N., Araújo, M., Trigo-Teixeira, A., Falcão, A. P., and Mazzolari, A. (2014). Storm-Surge hindcast at Viana do Castelo: an oceanic and estuarine domain approach. *Journal of Coastal Research*, 30(6):1268–1277.

Mendes, R., Sousa, M. C., de Castro, M., Gómez-Gesteira, M., and Dias, J. M. (2016). New insights into the Western Iberian Buoyant Plume: interaction between the Douro and Minho river plumes under winter conditions. *Progress in Oceanography*, 141:30–43.

Mil-Homens, M., Costa, A. M., Fonseca, S., Trancoso, M. A., Lopes, C., Serrano, R., and Sousa, R. (2013). Natural heavy metal and metalloid concentrations in sediments of the Minho river estuary

(Portugal): baseline values for environmental studies. *Environmental Monitoring and Assessment*, 185(7):5937–5950.

Najjar, R. G., Pyke, C. R., Adams, M. B., Breitburg, D., Hershner, C., Kemp, M., Howarth, R., Mulholland, M. R., Paolisso, M., Secor, D., Sellner, K., Wardrop, D., and Wood, R. (2010). Potential climate-change impacts on the Chesapeake Bay. *Estuarine, Coastal and Shelf Science*, 86(1):1–20.

Neves, R. (2007). Numerical models as decision support tools in coastal areas. In *Assessment of the Fate and Effects of Toxic Agents on Water Resources*, chapter 8, 171–195. Springer Netherlands.

Octavio, K. A. (1977). *Vertical heat transport mechanisms in lakes and reservoirs*. MSc thesis, Massachusetts Institute of Technology, 129 pp.

Pachauri, R. K., Allen, M. R., Barros, V. R., Broome, J., Cramer, W., Christ, R., Church, J. A., Clarke, L., Dahe, Q., Dasgupta, P., Dubash, N. K., Edenhofer, O., Elgizouli, I., Field, C. B., Forster, P., Friedlingstein, P., Fuglestvedt, J., Gomez-Echeverri, L., Hallegatte, S., Hegeri, G., Howden, M., Jiang, K., Cisneroz, B. J., Kattsov, V., Lee, H., Mach, K. J., Marotzke, J., Mastrandrea, M. D., Meyer, L., Minx, J., Mulugetta, Y., O'Brien, K., Oppenheimer, M., Pereira, J. J., Pichs-Madruga, R., Plattner, G.-K., Pörtner, H.-O., Power, S. B., Preston, B., Ravindranath, N. H., Reisinger, A., Riahi, K., Rusticucci, M., Scholes, R., Seyboth, K., Sakona, Y., Stavins, R., Stocker, T. F., Tschakert, P., van Vuuren, D., and van Ypserle, J.-P. (2014). *Climate Change 2014: Synthesis Report. Contribution of Working Groups I, II and III to the Fifth Assessment Report of the Intergovernmental Panel on Climate Change.* Intergovernmental Panel on Climate Change, Geneva, Switzerland, 112 pp.

Pawlowicz, R., Beardsley, B., and Lentz, S. (2002). Classical tidal harmonic analysis including error estimates in MATLAB using T_TIDE. *Computers and Geosciences*, 28(8):929–937.

Picado, A. (2016). *Influence of physical processes on the primary production along the Iberian Peninsula northwestern coast*. PhD thesis, Aveiro,Porto and Minho University, 191 pp.

Pinho, J. L. and Vieira, J. M. (2005). Mathematical modelling of salt water intrusion in a Northern Portuguese estuary. Technical report, Minho University, Braga, 14 pp.

Pinto, R. and Martins, F. C. (2013). The Portuguese national strategy for integrated coastal zone management as a spatial planning instrument to climate change adaptation in the Minho river estuary (Portugal NW-Coastal Zone). *Environmental Science and Policy*, 33:76–96.

Pritchard, D. W. (1967). What is an estuary: a physical viewpoint. *American Association for the Advancement of Science*, 83:3–5.

Rahbani, M. (2015). A comparison between the suspended sediment concentrations derived from DELFT3D model and collected using transmissometer - a case study in tidally dominated area of Dithmarschen Bight. *Oceanologia*, 57(1):44–49.

Ramos, S. (2007). *Ichthyoplankton of the Lima estuary (NW Portugal): Ecology of the early life stages of Pleuronectiformes*. PhD thesis, Porto University, 190 pp.

Rebordão, I. and Trigo-Teixeira, A. (2009). Tidal propagation in the Lima estuary. *Journal of Coastal Research*, SI 56:1400–1404.

Ribeiro, A. S. (2015). *Coupled modelling of the Tagus and Sado estuaries and their associated mesoscale patterns*. MSc thesis, Aveiro University, 103 pp.

Ribeiro, A. S., Sousa, M. C., Lencart-Silva, J., and Dias, J. M. (2016). David and Goliath revisited: joint modelling of the Tagus and Sado estuaries. *Journal of Coastal Research*, 75:123–127.

Richardson, L. F. (1920). The supply of energy from and to atmospheric eddies. *Proceedings of the Royal Society London*, 97:345–373.

Rodi, W. (1984). *Turbulence models and their application in hydraulics*. State-of-the-art paper article sur l'etat de connaissance. IAHR Paper presented by the IAHR-Section on Fundamentals of Division II: Experimental and Mathematical Fluid Dynamics, The Netherlands, 105 pp.

Rodrigues, J. (2015). *The Tagus estuarine plume variability: impact in coastal circulation and hydrography*. MSc thesis, Aveiro University, 70 pp.

Roebeling, P., Alves, H., Rocha, J., Brito, A., Almeida, P., and Mamede, J. (2014). Gains from trans-boundary water quality management in linked catchment and coastal socio-ecological systems: a case study for the Minho region. *Water Resources and Economics*, 8:32–42.

Santos, A. I., Balsinha, M. J., Oliveira, A. T., and da Silva, A. J. (2006). Tide induced aariability in the hydrography and dynamics of the Minho and Douro estuaries during low runoff. *5th Symposium on the Iberian Atlantic Margin*, 195–197.

Savenije, H. (2012). *Salinity and tides in alluvial estuaries*. Elsevier, Netherlands, second edition, 163 pp.

Shanas, P. R. and Kumar, V. S. (2014). Coastal processes and longshore sediment transport along Kundapura coast, central west coast of India. *Geomorphology*, 214:436–451.

Snyder, M. A., Sloan, L. C., Diffenbaugh, N. S., and Bell, J. L. (2003). Future climate change and upwelling in the California current. *Geophysical Research Letters*, 30(15):4.

Sousa, M. C. (2013). *Modelling the Minho river plume intrusion into the Rias Baixas*. PhD thesis, Aveiro and Porto University, 136 pp.

Sousa, R., Guilhermino, L., and Antunes, C. (2005). Molluscan fauna in the freshwater tidal area of the river Minho estuary, NW of Iberian Peninsula. *Annales de Limnologie - International Journal of Limnology*, 41(2):141–147.

Sousa, M. C., Mendes, R., Alvarez, I., Vaz, N., Gomez-Gesteira, M., and Dias, J. M. (2014a). Unusual circulation patterns of the rias baixas induced by minho freshwater intrusion (NW of the Iberian Peninsula). *PLoS ONE*, 9(11):1–9.

Sousa, M. C., Vaz, N., Alvarez, I., Gomez-Gesteira, M., and Dias, J. M. (2014b). Influence of the Minho river plume on the rias baixas (NW of the Iberian Peninsula). *Journal of Marine Systems*, 139:248–260.

Sousa, M. C., Vaz, N., Alvarez, I., Gomez-Gesteira, M., and Dias, J. M. (2014c). Modeling the Minho river plume intrusion into the Rias Baixas (NW Iberian Peninsula). *Continental Shelf Research*, 85:30–41.

Stelling, G. S. (1983). *On the construction of computational methods for shallow water flow problems*. PhD thesis, Delft University of Technology, 223 pp.

Thatcher, M. L. and Harleman, D. R. (1972). A mathematical model for the prediction of unsteady salinity intrusion in estuaries. Technical report, MIT School of Engineering Massachusetts. Department of Civil Engineering, 232 pp.

Trigo-Teixeira, A. and Rebordão, I. (2009). An assessment of tidal energy potential: the Lima estuary. In *Proceedings of the 8th European Wave and Tidal Energy Conference*, 174–180, Uppsala, Sweden.

Vale, L. M. (2008). *Estudo Hidrodinâmico do porto de Viana do Castelo*. MSc thesis, Universidade de Aveiro, 152 pp.

Vale, L. M. and Dias, J. M. (2011). The effect of tidal regime and river flow on the hydrodynamics and salinity structure of the Lima estuary: use of a numerical model to assist on estuary classification. *Journal of Coastal Research*, SI 64:1604–1608.

Vieira, J. M. and Pinho, J. L. (2010). Salt distribution in river Lima estuary for different hydrodinamic regimes. *Recursos Hídricos*, 31:5–14.

Vieira, L. R., Guilhermino, L., and Morgado, F. (2015). Zooplankton structure and dynamics in two estuaries from the Atlantic coast in relation to multi-stressors exposure. *Estuarine, Coastal and Shelf Science*, 167:347–367.

Willmott, C. J. (1981). On the validation of models. *Physical Geography*, 2(2):184–194.

Zacarias, N. G. (2007). Influência da batimetria e do caudal fluvial na propagação da maré no estuário do rio Minho. Technical report, Universidade de Évora, 81 pp.